UNIVERSITY OF BELGRADE
FACULTY OF PHYSICS

MASTER'S THESIS

Ab Initio Calculation of Charge-Carrier Mobility in ZnO

Student: Ljubica Grašić

Supervisors: Dr. Nenad Vukmirović and Prof. Dr. Saša Dmitrović

Belgrade, 2025.

Abstract

This master's thesis presents *ab initio* calculations of temperature-dependent electron and hole mobilities in wurtzite ZnO. The electronic structure was obtained using DFT including spin-orbit coupling, while the phonon dispersions, high-frequency relative dielectric tensor, and *Born* effective charges were calculated using DFPT. Electron-phonon coupling matrix elements were evaluated at arbitrary k- and q-points by *Wannier-Fourier* interpolation, including the long-range *Fröhlich* contribution. Carrier momentum relaxation times and mobilities were then calculated within the momentum-relaxation-time approximation to the *Boltzmann* transport equation. The calculations employed a grid-free method based on random (*Monte Carlo*) sampling of charge-carrier states and phonon-wave-vector directions. By avoiding predefined dense grids, this method substantially reduces the computational cost. The energy and temperature dependence of the relaxation times was analysed to identify the dominant scattering mechanisms and their role in limiting mobility. Calculated quantities were compared with reliable experimental data where available.

Acknowledgements

I am deeply grateful to my supervisors, Dr. Nenad Vukmirović and Prof. Dr. Saša Dmitrović, for their advice and support during the preparation of this thesis. I owe particular thanks to Dr. Nenad Vukmirović for everything he helped me learn and inspired me to explore over the past year, and for his invaluable guidance, which greatly improved this work.

I am also grateful to the Institute of Physics Belgrade, a National Institute of the Republic of Serbia, for providing all the facilities required to complete this work.

I would also like to thank the Scientific Computing Laboratory of the Institute of Physics Belgrade for providing access to the PARADOX IV computing cluster.

I am grateful to Prof. Dr. Goran Poparić for his inspiring lectures, consultations, and discussions, which further deepened my love of physics. I would also like to thank Prof. Dr. Milica Milovanović, whose undergraduate lectures and advice helped me choose a master's thesis topic in solid-state physics.

Finally, I wish to thank my grandmother Nevenka and my grandfather Živojin, who have always believed in me and supported me unconditionally throughout my life.

Contents

List of Figures

List of Tables

1 Introduction

First-principles calculations of materials properties inevitably involve approximations. Some are essential to make the calculations feasible, whereas others primarily reduce the computational cost. Although greater efficiency can come at the expense of accuracy, a successful approximation may also provide physical insight by identifying the ingredients needed to reproduce a phenomenon. Developing accurate and efficient computational methods is therefore important both for understanding the microscopic mechanisms that determine materials properties and for identifying materials with desirable characteristics.

At sufficiently high temperatures, phonon scattering is the principal mechanism limiting carrier transport in sufficiently pure semiconductors; electron-phonon interactions also govern many optical and thermal properties. Although these properties can be measured directly, their accurate prediction from first principles remains challenging. Within the relaxation-time approximation, the *Boltzmann* transport equation provides a framework for calculating carrier momentum relaxation times and mobilities. The required inputs are the electronic structure, phonon dispersions, and electron-phonon coupling matrix elements of the material [1][2][3]. Electron-phonon interactions are generally treated perturbatively, which is appropriate when they are weak relative to, for example, electron-electron interactions. In 2007, a method based on *Wannier-Fourier* interpolation was developed to obtain electron-phonon coupling matrix elements on dense k- and q-point grids from calculations on coarse grids in non-polar semiconductors [1]. In polar semiconductors, however, long-wavelength longitudinal optical (LO) phonons generate macroscopic electric fields and give rise to the *Fröhlich* interaction, which can dominate the electron-phonon coupling [3]. Verdi and Giustino extended the interpolation scheme in 2015 to treat this long-range contribution correctly [2]. Even with this advance, evaluating carrier momentum relaxation times and mobilities remained computationally demanding [3]. A grid-free approach introduced in 2025 substantially reduces the computational cost by avoiding predefined dense grids and sampling only the relevant k- and q-points [4]. This is the method used here to calculate the momentum relaxation times and mobilities of conduction-band electrons and valence-band holes.

These transport calculations require the electronic structure and phonon dispersions as input. Density functional theory (DFT) is the most widely used framework for electronic-structure calculations and is implemented in numerous software packages [5]. Since its development in 1964–1965, advances in numerical methods and software have made accurate calculations for crystalline materials increasingly efficient. Phonon dispersions are most commonly obtained using density functional perturbation theory (DFPT) [6]. Both methods are used here, and their results provide the input for calculating the electron-phonon coupling matrix elements and, ultimately, the carrier momentum relaxation times and mobilities in wurtzite ZnO.

This thesis aims to determine the temperature-dependent momentum relaxation times and mobilities of electrons and holes in the polar semiconductor ZnO using *ab initio* calculations. The theoretical foundations are outlined first, followed by the computational methods and input data. The principal results are then presented and interpreted. The thesis concludes with a summary of the main findings and suggestions for improving the calculations and extending the study of transport in ZnO.

2 Theoretical Background

This section reviews the theoretical framework underlying the *ab initio* calculations used in this work. It begins with density functional theory and the approximations commonly employed in plane-wave electronic-structure calculations, followed by the transformation to a basis of *Wannier* functions. Spin-orbit coupling and the effective-mass approximation are then discussed. The treatment of lattice vibrations introduces phonon dispersions and density functional perturbation theory. The section next describes the *Wannier-Fourier* interpolation of electron-phonon coupling matrix elements from coarse k- and q-point grids to arbitrary k- and q-points, with particular attention to the long-range *Fröhlich* interaction in polar semiconductors such as ZnO. Finally, the expressions for carrier momentum relaxation times and mobilities within the relaxation-time approximation are presented.

2.1 Electronic Structure of Crystals

A crystal is a many-particle system of nuclei and electrons. Neglecting relativistic effects, its stationary states satisfy the time-independent many-particle *Schrödinger* equation:

$$\hat{H}\Psi(\mathbf{r}_1, ..., \mathbf{r}_N, \mathbf{R}_1, ..., \mathbf{R}_M) = E_{tot}\Psi(\mathbf{r}_1, ..., \mathbf{r}_N, \mathbf{R}_1, ..., \mathbf{R}_M),$$

where $\Psi(\mathbf{r}_1, ..., \mathbf{r}_N, \mathbf{R}_1, ..., \mathbf{R}_M)$ is the wave function of a system consisting of N electrons at positions $\mathbf{r}_1, ..., \mathbf{r}_N$ and M nuclei at positions $\mathbf{R}_1, ..., \mathbf{R}_M$, while E_{tot} is the total energy of the system. In *Hartree* atomic units, the Hamiltonian $\hat{H}$ is defined as

$$\hat{H} = -\frac{1}{2}\sum_{k=1}^{M}\frac{1}{M_k}\nabla_k^2 - \frac{1}{2}\sum_{i=1}^{N}\nabla_i^2 + \frac{1}{2}\sum_{k\neq m}\frac{Z_k Z_m}{R_{km}} + \frac{1}{2}\sum_{i\neq j}\frac{1}{r_{ij}} - \sum_{i=1}^{N}\sum_{k=1}^{M}\frac{Z_k}{r_{ik}}, \tag{2.1.1}$$

Here M_k denotes a nuclear mass, ∇_k^2 and ∇_i^2 are Laplacians with respect to nuclear and electronic coordinates, respectively, Z_k is the atomic number of the kth nucleus, r_{ij} is the distance between the ith and jth electrons, R_{km} is the distance between the kth and mth nuclei, and r_{ik} is the distance between the ith electron and the kth nucleus. Relativistic effects have been neglected [7].

To simplify the Hamiltonian in Eq. 2.1.1, the *Born-Oppenheimer* approximation is introduced, in which the nuclei are nearly stationary relative to the electrons. This approximation is justified because nuclear masses are much greater than the electron mass and nuclear velocities are therefore much smaller than electronic velocities. The nuclear kinetic energy may consequently be neglected, whereas the nucleus-nucleus interaction energy can be treated as a constant. The *Born-Oppenheimer* approximation thus allows $\hat{H}$ to be written as

$$\hat{H}_{BO} = -\frac{1}{2}\sum_{i=1}^{N}\nabla_i^2 + \sum_{i=1}^{N}V_n(\mathbf{r}_i) + \frac{1}{2}\sum_{i\neq j}\frac{1}{r_{ij}} + \frac{1}{2}\sum_{k\neq m}\frac{Z_k Z_m}{R_{km}}, \tag{2.1.2}$$

where

$$V_n(\mathbf{r}) = -\sum_{k=1}^{M}\frac{Z_k}{|\mathbf{R}_k - \mathbf{r}|}, \tag{2.1.3}$$

is the electrostatic potential of the nuclei. The time-independent *Schrödinger* equation for electrons in the nuclear potential $V_n(\mathbf{r})$, with total wave function $\Psi = \Psi(\mathbf{r}_1, ..., \mathbf{r}_N)$,

can then be written as

$$\hat{H}_{BO}\Psi = (E + \frac{1}{2}\sum_{k\neq m}\frac{Z_k Z_m}{R_{km}})\Psi \equiv E_{tot}\Psi, \tag{2.1.4}$$

where the Hamiltonian $\hat{H}_{BO}$ of the electrons and fixed nuclei in the *Born-Oppenheimer* approximation, as well as the electronic wave function Ψ, depend parametrically on the fixed nuclear positions $\mathbf{R}_1, ..., \mathbf{R}_M$ [8]. Although the original problem has been greatly simplified, solving Eq. 2.1.4 remains highly challenging. Density functional theory (DFT) provides one approach for determining the electronic structure from Eqs. 2.1.2–2.1.4.

2.1.1 Density Functional Theory (DFT)

In 1964, *Hohenberg* and *Kohn* proved the existence of a universal functional of the electron density, $\mathcal{F}[n]$, unique for the external nuclear potential $V_n(\mathbf{r})$ experienced by the electrons, whose minimising density $n_0(\mathbf{r})$ is the ground-state electron density of the system [9]. In the same work, they proposed writing this universal functional as

$$\mathcal{F}[n] = \int V_n(\mathbf{r})n(\mathbf{r})d\mathbf{r} + \frac{1}{2}\int V_H(\mathbf{r})n(\mathbf{r})d\mathbf{r} + \mathcal{G}[n], \tag{2.1.5}$$

where $V_H(\mathbf{r}) = \int \frac{n(\mathbf{r}')}{|\mathbf{r}-\mathbf{r}'|}d\mathbf{r}'$ is the *Hartree* potential and $\mathcal{G}[n]$ is another universal functional. In the following year, *Kohn* and *Sham* proposed the decomposition

$$\mathcal{G}[n] = T_s[n] + E_{xc}[n], \tag{2.1.6}$$

where $T_s[n]$ is the kinetic energy of a non-interacting electron system with density $n(\mathbf{r})$, and $E_{xc}[n]$ is the exchange-correlation energy of the interacting system with the same density [10]. When $n(\mathbf{r})$ varies slowly in space, the exchange-correlation energy can be expressed as

$$E_{xc}[n] = \int n(\mathbf{r})\epsilon_{xc}(n(\mathbf{r}))d\mathbf{r} + \int (\nabla n(\mathbf{r}))^2\epsilon_{xc}^{(2)}(n(\mathbf{r}))d\mathbf{r} + ..., \tag{2.1.7}$$

where $\epsilon_{xc}(n(\mathbf{r}))$ is the exchange-correlation energy per electron of a homogeneous electron gas with density $n(\mathbf{r})$, while $\epsilon_{xc}^{(2)}(n(\mathbf{r}))$ describes the exchange-correlation contribution associated with the second term in the density expansion of the total energy [10]. Retaining the first term in this expansion leads to the *Kohn-Sham* equations:

$$\left(-\frac{1}{2}\nabla^2 + V_n(\mathbf{r}) + V_H(\mathbf{r}) + V_{xc}(\mathbf{r})\right)\psi_i(\mathbf{r}) = \epsilon_i\psi_i(\mathbf{r}), \tag{2.1.8}$$

$$n(\mathbf{r}) = 2\sum_{i=1}^{N}|\psi_i(\mathbf{r})|^2, \tag{2.1.9}$$

where $V_{xc}(\mathbf{r}) = \frac{d(n\epsilon_{xc}(n))}{dn}|_{n(\mathbf{r})}$ and the factor of 2 arises from spin degeneracy. These equations are solved self-consistently to obtain the ground-state electron density $n(\mathbf{r})$, from which the ground-state energy follows through Eqs. 2.1.5 and 2.1.6. The original many-particle system of interacting electrons is thereby mapped onto a system of non-interacting electrons with the same density and the corresponding *Kohn-Sham* Hamiltonian

$$\hat{H}_{KS} = -\frac{1}{2}\nabla^2 + V_n(\mathbf{r}) + V_H(\mathbf{r}) + V_{xc}(\mathbf{r}). \tag{2.1.10}$$

Thus, provided that the exchange-correlation functional $E_{xc}[n]$ is known, the density of the interacting electron system can be obtained by solving the one-particle *Schrödinger* equation in Eq. 2.1.8 self-consistently [5]. The *Kohn-Sham* eigenvalues ϵ_i are not, in general, the energies of one-particle states of the interacting system; rather, they are derivatives of the total energy with respect to the occupation of the corresponding state [11]. Nevertheless, in atomic and molecular electronic-structure calculations, the highest occupied *Kohn-Sham* eigenvalue is closely related to the ionisation energy [12]. Strictly speaking, therefore, the band structure obtained by solving the *Kohn-Sham* equations is not the electronic band structure of the interacting crystal. In practice, however, the *Kohn-Sham* bands often approximate the valence-band structure well. Semiconductor band gaps, by contrast, are generally underestimated [13].

Despite its limitations, DFT provides a powerful framework for quantitative and qualitative studies of the electronic structure of real materials. Efficient numerical solution of the *Kohn-Sham* equations is therefore essential.

As the number of electrons in the unit cell increases, ground-state electronic-structure calculations become progressively more demanding. Additional approximations are therefore introduced to reduce the cost of solving the *Kohn-Sham* equations [5]. Several approximations commonly used in electronic-structure software are described below.

2.1.2 Exchange-Correlation Functional

Electrons are fermions and therefore obey the *Pauli* exclusion principle. A many-electron wave function must be antisymmetric under exchange of any two electrons. This antisymmetry gives rise to the exchange contribution, which lowers the ground-state energy relative to that of distinguishable particles in the same potential. Exchange is treated exactly within the *Hartree-Fock* approximation, although the computational cost increases with system size [8]. Correlation effects beyond *Hartree-Fock*, however, cannot generally be treated exactly in practical calculations. The difference between the exact energy of the interacting electron system and the *Hartree-Fock* energy is called the correlation energy. The exchange-correlation energy therefore contains the part of the electron-electron interaction energy not included in the classical electrostatic repulsion.

In their 1965 paper [10], *Kohn* and *Sham* proposed the local-density approximation (LDA) for the exchange-correlation functional. LDA assumes that the exchange-correlation energy per electron at a point $\mathbf{r}$, $\epsilon_{xc}(\mathbf{r})$, depends only on the local electron density $n(\mathbf{r})$ and equals that of a homogeneous electron gas at the same density. Contributions arising from density variations around $\mathbf{r}$ are therefore neglected. Exchange-correlation energies for finite homogeneous systems of approximately 100 electrons at different densities were calculated using *Monte Carlo* simulations and subsequently parameterised [14][15]. In 1997, *Perdew*, *Burke*, and *Ernzerhof* extended LDA by introducing a dependence on the local density gradient [16]. This approach is known as the generalised gradient approximation (GGA). For a homogeneous electron system, the PBE-GGA functional reduces to the corresponding LDA limit. PBE-GGA is a non-empirical functional and remains one of the most widely used approximations in electronic-structure calculations for crystals.

2.1.3 Periodic Supercells

Bulk three-dimensional crystals are periodic along three non-coplanar directions and therefore contain, formally, infinitely many electrons and ions. Without exploiting this

periodicity, the *Kohn-Sham* problem would involve an infinite system of equations. Moreover, because the *Kohn-Sham* wave functions generally extend throughout space, their plane-wave expansions formally contain infinitely many terms. Crystal periodicity and *Bloch*'s theorem [7] allow the electronic wave functions to be written as

$$\psi_{i\mathbf{k}}(\mathbf{r}) = e^{i\mathbf{k}\mathbf{r}} \sum_{\mathbf{G}} c_{i\mathbf{k}}^{\mathbf{G}} e^{i\mathbf{G}\mathbf{r}}, \tag{2.1.11}$$

where the sum runs over all reciprocal-lattice vectors $\mathbf{G}$, $c_{i\mathbf{k}}^{\mathbf{G}}$ are coefficients in the *Fourier* expansion of the periodic part of the *Bloch* wave function, and i is the band index.

For sufficiently small $\Delta\mathbf{k}$, $\psi_{i\mathbf{k}}(\mathbf{r}) \approx \psi_{i\mathbf{k}+\Delta\mathbf{k}}(\mathbf{r})$. The ground-state energy can therefore be evaluated by sampling the *Bloch* wave functions at a finite set of crystal momenta $\mathbf{k}$ [5]. *Monkhorst* and *Pack* developed a scheme for selecting these k-points from the first *Brillouin* zone efficiently and accurately [17]. Their sampling scheme selects three integers q_1, q_2, and q_3, defines the sets $\{u_{r_i} : u_{r_i} = \frac{2r_i - q_i - 1}{2q_i}, r_i \in \{1, ..., q_i - 1, q_i\}\}$, and constructs the k-points as all linear combinations

$$\mathbf{k} = \sum_{i=1}^{3} u_{r_i} \mathbf{b}_i,$$

where $\mathbf{b}_i$ are primitive reciprocal-lattice vectors.

In the plane-wave expansion of the periodic part $\sum_{\mathbf{G}} c_{i\mathbf{k}}^{\mathbf{G}} e^{i\mathbf{G}\mathbf{r}}$ of the *Bloch* wave function $\psi_{i\mathbf{k}}(\mathbf{r})$, the coefficients $c_{i\mathbf{k}}^{\mathbf{G}}$ decrease as the magnitude of $\mathbf{G}$ increases. It is therefore reasonable to introduce the approximation

$$\psi_{i\mathbf{k}}(\mathbf{r}) = e^{i\mathbf{k}\mathbf{r}} \sum_{\mathbf{G} \in S_{\mathbf{G}}^{i\mathbf{k}}} c_{i\mathbf{k}}^{\mathbf{G}} e^{i\mathbf{G}\mathbf{r}}, \tag{2.1.12}$$

where $S_{\mathbf{G}}^{i\mathbf{k}} = \{\mathbf{G} : |\mathbf{G}| < \left|\mathbf{G}_{max}^{\mathbf{k}}\right|\}$ and $\left|\mathbf{G}_{max}^{\mathbf{k}} + \mathbf{k}\right|^2 / 2 < E_{cut}$. The plane-wave kinetic-energy cutoff E_{cut} is generally chosen as the smallest value that satisfies the convergence criterion of the calculation. In this truncated plane-wave basis, Eq. 2.1.8 takes the form

$$\sum_{\mathbf{G}' \in S_{\mathbf{G}}^{i\mathbf{k}}} H_{\mathbf{G}\mathbf{G}'}^{\mathbf{k}} c_{i\mathbf{k}}^{\mathbf{G}'} = \epsilon_{i\mathbf{k}} c_{i\mathbf{k}}^{\mathbf{G}}, \tag{2.1.13}$$

where

$$H_{\mathbf{G}\mathbf{G}'}^{\mathbf{k}} = \frac{|\mathbf{G} + \mathbf{k}|^2}{2} \delta_{\mathbf{G}\mathbf{G}'} + V_H^{\mathbf{G}-\mathbf{G}'} + V_{xc}^{\mathbf{G}-\mathbf{G}'}. \tag{2.1.14}$$

Here $V_H^{\mathbf{G}-\mathbf{G}'}$ and $V_{xc}^{\mathbf{G}-\mathbf{G}'}$ are coefficients in the plane-wave *Fourier* expansions of the potentials $V_H(\mathbf{r}) = \sum_{\mathbf{G}} V_H^{\mathbf{G}} e^{i\mathbf{G}\mathbf{r}}$ and $V_{xc}(\mathbf{r}) = \sum_{\mathbf{G}} V_{xc}^{\mathbf{G}} e^{i\mathbf{G}\mathbf{r}}$. Solving Eq. 2.1.13 reduces to diagonalising the matrices in Eq. 2.1.14. The matrix dimension is set by E_{cut}, or equivalently by the cardinality of $S_{\mathbf{G}}^{i\mathbf{k}}$. Without further approximations, an accurate ground-state energy and electron density require a large E_{cut} and hence the diagonalisation of very large matrices. The pseudopotential approximation reduces this cost: a modified form of Eq. 2.1.13 is solved only for the valence electrons and in the region sufficiently far from the nuclei, where the *Kohn-Sham* wave functions vary much more slowly. The ground-state energy then converges at a substantially lower value of E_{cut} [5].

2.1.4 Pseudopotentials

Many physical properties of solids depend far more strongly on the valence electrons than on the core electrons. Moreover, treating core-electron orbitals in a crystal as identical to the atomic orbitals of isolated atoms gives good quantitative results in practice. These observations justify the pseudopotential approximation, in which the potential of the nuclei and core electrons is replaced by a new function called a pseudopotential. Outside a core region bounded by a sphere of radius r_c, the core radius, this pseudopotential coincides with the nuclear potential plus the averaged potential of the core electrons. Inside the core region, it differs from the true potential and remains finite at the nuclear position. The pseudopotential and its first spatial derivative are also required to be continuous. It is constructed so that the valence pseudo-wave functions outside the core region equal the valence wave functions obtained by solving the all-electron *Kohn-Sham* equations 2.1.8. Inside the core region, however, the pseudo-wave functions are nodeless and vary slowly in space. The true valence wave functions vary rapidly near the nuclei and possess several nodes because they must be orthogonal to all core-electron wave functions. The smoother pseudo-wave functions can therefore be represented accurately by a plane-wave set $S'^{i\mathbf{k}}_{\mathbf{G}}$ whose cardinality is much smaller than that of $S^{i\mathbf{k}}_{\mathbf{G}}$. In other words, the ground-state energy and electron density outside the core regions can be calculated accurately with a substantially lower E_{cut}.

One may additionally require that the integrals of the probability density over the entire core region be equal for an all-electron state and its corresponding pseudo-state. A pseudopotential satisfying this condition is said to be norm-conserving [5].

2.1.5 Maximally Localised *Wannier* Functions

The *Bloch* wave functions in Eq. 2.1.11 represent eigenstates of the electronic Hamiltonian in a plane-wave basis and are localised in reciprocal space. The same eigenstates can also be represented in a direct-lattice basis formed by *Wannier* functions, which are localised in real space and defined as

$$w_{n\mathbf{R}}(\mathbf{r}) = \frac{1}{N_k} \sum_{\mathbf{k}} e^{-i\mathbf{k}\mathbf{R}} \psi_{n\mathbf{k}}(\mathbf{r}). \tag{2.1.15}$$

Strictly speaking, N_k is the number of unit cells in the crystal. In calculations it is replaced by the number of points in the DFT k-point grid, which is mathematically equivalent to considering a crystal containing that number of unit cells and imposing *Born-von Karman* periodic boundary conditions. These functions satisfy

$$w_{n\mathbf{R}}(\mathbf{r}) = w_{n\mathbf{R}+\mathbf{R}'}(\mathbf{r}+\mathbf{R}'). \tag{2.1.16}$$

and are therefore functions of the difference $\mathbf{r}-\mathbf{R}$. Multiplying the *Bloch* functions by a phase factor $e^{i\theta(\mathbf{k})}$, where $\theta(\mathbf{k})$ is an arbitrary continuous function of crystal momentum, leaves the transformed states as eigenstates. The gauge-transformed *Bloch* states are physically equivalent to the original states, but the transformation can substantially alter the properties of the associated *Wannier* functions [18].

Marzari and *Vanderbilt* derived a general expression for constructing J *Wannier* functions from $J \cdot N_k$ *Bloch* functions. The selected states, with band indices $n \in \{m, m+1, ..., m+J\}$, may cross or become degenerate with one another and are then

described as entangled, but they must remain separated from all other *Bloch* states with $n' \notin \{m, m+1, ..., m+J\}$. Generalised *Wannier* functions can then be constructed as

$$w_{j\mathbf{R}}(\mathbf{r}) = \frac{1}{N_k} \sum_{\mathbf{k}} e^{-i\mathbf{kR}} \sum_{n=m}^{m+J} U_{\mathbf{k},nj} \psi_{n\mathbf{k}}(\mathbf{r}). \tag{2.1.17}$$

Here $U_{\mathbf{k}}$ are $J \times J$ unitary matrices describing the generalised multiband gauge freedom in choosing the *Bloch* basis for the Hamiltonian subspace spanned by bands $n \in \{m, m+1, ..., m+J\}$ [19]. These are called unitary mixing matrices. The same work introduced maximally localised *Wannier* functions (MLWFs), obtained through unitary transformations $U_{\mathbf{k}}$ of the *Bloch* functions that minimise the quadratic spread, or localisation functional, of the corresponding *Wannier* functions:

$$\Omega = \sum_{j=1}^{J} \left(\left| \langle \mathbf{0}j | \, \mathbf{r}^2 \, | \mathbf{0}j \rangle \right| - | \langle \mathbf{0}j | \, \mathbf{r} \, | \mathbf{0}j \rangle |^2 \right), \tag{2.1.18}$$

where $|\mathbf{0}j\rangle$ corresponds to the *Wannier* function $w_{j\mathbf{0}}(\mathbf{r})$. This functional and its gradient with respect to infinitesimal gauge transformations can be represented and evaluated in a plane-wave basis. The MLWF construction implemented in WANNIER90 is based on this principle. The resulting MLWFs can be used to recover the *Bloch* states as

$$\psi_{n\mathbf{k}}(\mathbf{r}) = \sum_{\mathbf{R}} e^{i\mathbf{kR}} \sum_{j=1}^{J} U^{\dagger}_{\mathbf{k},jn} w_{j\mathbf{R}}(\mathbf{r}), \tag{2.1.19}$$

at arbitrary crystal momenta $\mathbf{k}$ outside the original coarse DFT k-point grid, at far lower computational cost than direct diagonalisation of the electronic Hamiltonian in the plane-wave representation. The electronic Hamiltonian in the *Wannier* representation has dimension $J \times J$, whereas the *Bloch* representation typically requires a much larger plane-wave basis. Further theoretical and implementation details of MLWF construction are given in Ref. [18].

2.2 Influence of Spin-Orbit Coupling on the Electronic Structure

The preceding treatment neglects spin-dependent relativistic effects. In a crystal, an electron experiences a term proportional to the scalar product of its spin magnetic moment and the cross product of its velocity with the electric field. This term gives rise to spin-orbit coupling (SOC), which can lift band degeneracies, particularly at high-symmetry points of the first Brillouin zone. The strength of SOC generally increases with atomic number; it may therefore be negligible in some crystals but substantially modify the electronic structure of others [7]. When SOC is included in a band-structure calculation, each band from a calculation without SOC corresponds to a time-reversal-related pair known as a *Kramers* pair [20].

2.3 Effective-Mass Approximation

In the semiclassical description of charge carriers, the inverse effective-mass tensor near a band minimum for electrons or a band maximum for holes is defined as

$$[m^{-1}(\mathbf{k})]_{ij} = \pm \frac{\partial^2 \epsilon(\mathbf{k})}{\partial k_i \partial k_j} = \pm \frac{\partial v_i}{\partial k_j}, \tag{2.3.1}$$

where the right-hand side is taken with the + sign for electrons and the − sign for holes, so that the effective mass is positive by definition for all carriers [7]. This approximation describes semiconductor effective masses well when the dispersion near a conduction-band minimum or valence-band maximum can be represented accurately by [21]

$$\epsilon(\mathbf{k}) = \epsilon_0 \pm \frac{1}{2}\sum_{ij}[m^{-1}(\mathbf{k})]_{ij}k_i k_j. \tag{2.3.2}$$

In the semiclassical description of a crystal, the equation of motion is [7]

$$\mathbf{a} = \pm m^{-1}(\mathbf{k})\dot{\mathbf{k}}. \tag{2.3.3}$$

For a diagonal inverse effective-mass tensor, the inverse of each diagonal element is the carrier effective mass m^* along the corresponding direction. Bands with a diagonal inverse effective-mass tensor are referred to as parabolic, while those associated with a non-diagonal tensor are described as ellipsoidal [21]. Transforming to a basis in which the tensor is diagonal yields its principal axes. Equation 2.3.3 shows that, for carrier motion along a principal axis, the acceleration and applied force are parallel; this is generally not true along other directions.

2.4 Lattice Dynamics, Phonon Dispersions, and DFPT

The *Born-Oppenheimer* approximation reduces the many-particle *Schrödinger* equation for the electrons and nuclei of a crystal to the purely electronic Eq. 2.1.4. DFT provides an approximate solution for electrons in the field of stationary nuclei. In real systems, however, the nuclei move even at $T = 0$. Because nuclei are much heavier than electrons, it is reasonable to treat their motion classically. For many materials, at least near room temperature, the nuclear displacements from equilibrium may also be assumed small relative to the dimensions of the primitive unit cell.

For nuclei in the effective potential of the electrons and all other nuclei, let $\mathbf{R}_{\mu s}$ denote the equilibrium positions and $\mathbf{u}_{\mu s}$ their displacements, where $\mu \in \{1, ..., N_{uc}\}$ labels unit cells and $s \in \{1, ..., N_n\}$ labels nuclei within a unit cell. In the harmonic approximation, the classical nuclear Hamiltonian can be expanded in the displacements as

$$H(\mathbf{R}+\mathbf{u}) = \sum_{\mu s\alpha}\frac{P^2_{\mu s\alpha}}{2M_s} + \frac{1}{2}\sum_{\mu s\alpha}\sum_{\nu s'\beta}\frac{\partial^2 E_{tot}}{\partial u_{\mu s\alpha}\partial u_{\nu s'\beta}}\Big|_{\mathbf{u}=\mathbf{0}} u_{\mu s\alpha}u_{\nu s'\beta}. \tag{2.4.1}$$

Here $\mathbf{R}+\mathbf{u} \equiv \{\mathbf{R}_{\mu s}+\mathbf{u}_{\mu s} : \mu \in \{1, ..., N_{uc}\}, s \in \{1, ..., N_n\}\}$, $P_{\mu s\alpha}$ are the generalised nuclear momenta, and E_{tot} is the total energy of the electrons and nuclei, with the electronic subsystem in its ground state for the specified nuclear configuration. The indices α and β label Cartesian components of $\mathbf{u}_{\mu s}$, with $\alpha, \beta \in \{1, 2, 3\}$ for a three-dimensional crystal. Equation 2.4.1 yields the nuclear equations of motion

$$M_s\ddot{u}_{\mu s\alpha} = -\sum_{\nu s'\beta}\frac{\partial^2 E_{tot}}{\partial u_{\mu s\alpha}\partial u_{\nu s'\beta}}\Big|_{\mathbf{u}=\mathbf{0}} u_{\nu s'\beta}. \tag{2.4.2}$$

Solutions are sought in the form

$$u_{\mu s\alpha}(t) = \frac{1}{\sqrt{M_s}}u_{s\alpha}(\mathbf{q})e^{i(\mathbf{q}\mathbf{R}_\mu - \omega_{\mathbf{q}}t)}, \tag{2.4.3}$$

where $\mathbf{q}$ is the phonon wave vector in the first Brillouin zone. The dynamical matrix is defined as

$$D_{s\alpha s'\beta}(\mathbf{q}) \equiv \frac{1}{\sqrt{M_s M_{s'}}} \frac{1}{N_{uc}} \sum_{\mu\nu} \frac{\partial^2 E_{tot}}{\partial u_{\mu s\alpha} \partial u_{\nu s'\beta}}\Big|_{\mathbf{u}=\mathbf{0}} e^{i\mathbf{q}(\mathbf{R}_\nu - \mathbf{R}_\mu)}. \tag{2.4.4}$$

Diagonalising this matrix yields the phonon dispersions $\omega^\nu(\mathbf{q})$:

$$\sum_{s'\beta} D_{s\alpha s'\beta}(\mathbf{q}) u^\nu_{s'\beta}(\mathbf{q}) = \omega^2_\nu(\mathbf{q}) u^\nu_{s\alpha}(\mathbf{q}). \tag{2.4.5}$$

The index $\nu \in \{1, ..., 3N_n - 1, 3N_n\}$ labels the linearly independent eigenvectors of the dynamical matrix and is referred to as the phonon-branch index. Determining the phonon dispersions therefore requires the dynamical matrix. The *Hellmann-Feynman* theorem gives

$$\frac{\partial E_{tot}(\mathbf{R}+\mathbf{u})}{\partial u_{\mu s\alpha}} = \langle \Psi^{\mathbf{R}+\mathbf{u}} | \frac{\partial H_{BO}}{\partial u_{\mu s\alpha}} | \Psi^{\mathbf{R}+\mathbf{u}} \rangle, \tag{2.4.6}$$

which makes it possible to determine the dynamical matrix from the ground-state electron density at the equilibrium nuclear positions and its first derivatives with respect to nuclear displacements:

$$\frac{\partial^2 E_{tot}(\mathbf{R}+\mathbf{u})}{\partial u_{\mu s\alpha} \partial u_{\nu s'\beta}} = \int d\mathbf{r} \frac{\partial n(\mathbf{r})}{\partial u_{\mu s\alpha}} \frac{\partial V_n(\mathbf{r})}{\partial u_{\nu s'\beta}} + \int d\mathbf{r} n(\mathbf{r}) \frac{\partial^2 V_n(\mathbf{r})}{\partial u_{\mu s\alpha} \partial u_{\nu s'\beta}}. \tag{2.4.7}$$

For crystals with time-reversal symmetry, applying first-order perturbation theory and reducing the integrals over all space in the preceding expressions to unit-cell integrals leads, after a non-trivial derivation, to

$$\begin{aligned} \left(e^{-i(\mathbf{k}+\mathbf{q})\mathbf{r}} H_{KS} e^{i(\mathbf{k}+\mathbf{q})\mathbf{r}} - \epsilon_{i\mathbf{k}}\right) P_c^{\mathbf{k}+\mathbf{q}} \left(e^{-i\mathbf{q}\mathbf{r}} \frac{\partial \sum_{\mathbf{G}} c^{\mathbf{G}}_{i\mathbf{k}} e^{i\mathbf{G}\mathbf{r}}}{\partial u_{s\alpha}(\mathbf{q})} \right) = \\ = -P_c^{\mathbf{k}+\mathbf{q}} \left(e^{-i\mathbf{q}\mathbf{r}} \frac{\partial V(\mathbf{r})}{\partial u_{s\alpha}(\mathbf{q})} \sum_{\mathbf{G}} c^{\mathbf{G}}_{i\mathbf{k}} e^{i\mathbf{G}\mathbf{r}} \right). \end{aligned} \tag{2.4.8}$$

In this equation, $P_c = 1 - P_v$ projects onto the subspace of conduction eigenstates of H_{KS}, whereas P_v projects onto the valence-state subspace. The operator $P_c^{\mathbf{k}}$ is defined by $P_c = \sum_{\mathbf{k}} e^{i\mathbf{k}\mathbf{r}} P_c^{\mathbf{k}} e^{-i\mathbf{k}\mathbf{r}}$. The operator $\frac{\partial}{\partial u_{s\alpha}(\mathbf{q})}$ is defined as $\frac{\partial}{\partial u_{s\alpha}(\mathbf{q})} \equiv \frac{1}{\sqrt{M_s}} \sum_\nu e^{i\mathbf{q}\mathbf{R}_\nu} \frac{\partial}{\partial u_{\nu s\alpha}}\Big|_{\mathbf{u}=\mathbf{0}}$. The derivative of the electron density with respect to collective displacements of nuclei s along α, with propagation described by the phonon wave vector $\mathbf{q}$, is

$$\frac{\partial n(\mathbf{r})}{\partial u_{s\alpha}(\mathbf{q})} = 2 e^{i\mathbf{q}\mathbf{r}} \sum_{n\mathbf{k}} \sum_{\mathbf{G}} c^{\mathbf{G}}_{n-\mathbf{k}} e^{i\mathbf{G}\mathbf{r}} P_c^{\mathbf{k}+\mathbf{q}} \left(e^{-i\mathbf{q}\mathbf{r}} \frac{\partial \sum_{\mathbf{G}'} c^{\mathbf{G}'}_{n\mathbf{k}} e^{i\mathbf{G}'\mathbf{r}}}{\partial u_{s\alpha}(\mathbf{q})} \right). \tag{2.4.9}$$

The factor of 2 arises from spin degeneracy. Self-consistent solution of Eqs. 2.4.7, 2.4.8, and 2.4.9 yields the dynamical matrices as functions of phonon wave vector and hence the corresponding phonon dispersions and eigenvectors. This requires the effective potential experienced by the electrons and the electronic eigenstates of the unperturbed Hamiltonian, both of which can be obtained using DFT. The procedure described above for calculating the "electronic response" to a small perturbation of the potential is called density functional perturbation theory (DFPT) [6].

DFPT can also describe the linear electronic response to a homogeneous electric field by treating the field as a perturbation of the electrostatic potential experienced by the

electrons [6]. The corresponding self-consistent equations yield, among other quantities, the high-frequency relative dielectric tensor and the *Born* effective-charge tensors.

Phonon dispersions can be interpolated from a coarse q-point grid to an arbitrarily dense grid using standard *Fourier* interpolation. In polar crystals, long-wavelength longitudinal optical modes generate a long-range macroscopic electric field, producing a non-analyticity of the dynamical matrix at the Γ point. The non-analytic part must therefore be subtracted from the full dynamical matrix, the analytic part *Fourier*-interpolated, and the appropriately treated non-analytic term added back. This non-analytic correction can be calculated from the *Born* effective-charge tensors and the high-frequency relative dielectric tensor. Phonon dispersions obtained in this way exhibit LO-TO splitting, i.e. the lifting of the degeneracy between longitudinal and transverse optical-mode energies.

2.5 Electron-Phonon Interaction and *Wannier-Fourier* Interpolation

The electron-phonon interaction scatters an electron from a state $\psi_{n\mathbf{k}}(\mathbf{r})$ into a state $\psi_{m\mathbf{k+q}}(\mathbf{r})$ through the change $\Delta_{\nu\mathbf{q}}V(\mathbf{r})$ in the *Kohn-Sham* potential induced by a phonon with wave vector $\mathbf{q}$ and branch index ν. The electron-phonon coupling matrix element is defined as

$$\gamma_{mn,\nu}(\mathbf{k},\mathbf{q}) = \frac{1}{\sqrt{2\omega_\nu(\mathbf{q})}} \langle \psi_{m\mathbf{k+q}} | \, \Delta_{\nu\mathbf{q}} V \, | \psi_{n\mathbf{k}} \rangle \, . \tag{2.5.1}$$

The total change in the potential experienced by the electrons is

$$\Delta_{\nu\mathbf{q}} V = \sum_{\mu s\alpha} \frac{1}{\sqrt{M_s}} e^{i\mathbf{q}\mathbf{R}_\mu} u^\nu_{s\alpha} \frac{\partial V(\mathbf{r};\mathbf{R}+\mathbf{u})}{\partial u_{\mu s\alpha}}\Big|_{\mathbf{u}=\mathbf{0}}. \tag{2.5.2}$$

The factor $1/\sqrt{2\omega_\nu(\mathbf{q})}$ normalises the oscillation amplitude following quantisation of the collective vibrations into phonons. The squared magnitude of the electron-phonon, or hole-phonon, coupling matrix element is proportional to the probability of the corresponding scattering event. Hole-phonon coupling is defined analogously because holes correspond to unoccupied electron states below the *Fermi* level.

Above approximately 100 K, phonon scattering is typically the dominant mechanism limiting carrier mobility in sufficiently pure bulk semiconductors. Electron-phonon coupling matrix elements vary rapidly with phonon wave vector $\mathbf{q}$ and electron crystal momentum $\mathbf{k}$, particularly near Γ [3]. Accurate calculations of macroscopic properties that depend on these matrix elements therefore require extremely dense k- and q-point grids, much denser than those needed to converge typical DFT calculations. Direct DFPT calculations on such grids would be prohibitively expensive. *Wannier-Fourier* interpolation instead allows phonons and electron-phonon coupling matrix elements to be calculated on relatively coarse grids and interpolated onto arbitrarily dense k- and q-point grids [1].

Lattice periodicity permits the electron-phonon coupling matrix element to be defined in the *Wannier* basis as

$$\gamma_{m'n',s\alpha}(\mathbf{R}_e,\mathbf{R}_\mu) = \langle m'\mathbf{0}_e | \, \frac{\partial V}{\partial u_{\mu s\alpha}} \, | n'\mathbf{R}_e \rangle \, . \tag{2.5.3}$$

It can be calculated according to

$$\gamma(\mathbf{R}_e,\mathbf{R}_\mu) = \frac{1}{N_q} \sum_{\mathbf{k},\mathbf{q}} e^{-i(\mathbf{k}\mathbf{R}_e+\mathbf{q}\mathbf{R}_\mu)} U^\dagger_{\mathbf{k+q}} \gamma(\mathbf{k},\mathbf{q}) U_{\mathbf{k}}. \tag{2.5.4}$$

Inverse *Fourier* transformation at arbitrary $\mathbf{k}$ and $\mathbf{q}$ then gives the interpolated electron-phonon coupling matrix element.

2.6 The *Fröhlich* Interaction

In polar crystals such as ZnO, longitudinal optical (LO) phonons generate a macroscopic electric field. The interaction of electrons with this field is known as the *Fröhlich* interaction. It causes the electron-phonon coupling matrix element to diverge as $1/|\mathbf{q}|$ in the long-wavelength limit and is not captured by standard *Wannier-Fourier* interpolation, which relies on a short-ranged scattering potential [1][2]. In 2015, *Verdi* and *Giustino* generalised the *Fröhlich* vertex [22] to anisotropic polar materials with multiple phonon branches. Their long-range contribution $\gamma^L_{mn,\nu}(\mathbf{k},\mathbf{q})$ is

$$\gamma^L_{mn,\nu}(\mathbf{k},\mathbf{q}) \propto \sum_{s,\mathbf{G}\neq-\mathbf{q}} \frac{1}{\sqrt{2M_s\omega_\nu(\mathbf{q})}} \frac{(\mathbf{q}+\mathbf{G})\hat{Z}^*_s\mathbf{u}^\nu_s(\mathbf{q})}{(\mathbf{q}+\mathbf{G})\hat{\varepsilon}_\infty(\mathbf{q}+\mathbf{G})} \langle\psi_{m\mathbf{k}+\mathbf{q}}| e^{i(\mathbf{q}+\mathbf{G})\mathbf{r}} |\psi_{n\mathbf{k}}\rangle , \tag{2.6.1}$$

where $\hat{Z}^*_s$ is the *Born* effective-charge tensor of atom s, $\hat{\varepsilon}_\infty$ is the high-frequency relative dielectric tensor of the crystal, and $\mathbf{u}^\nu_s(\mathbf{q})$ is the vector with components $u^\nu_{s\alpha}(\mathbf{q})$ along the corresponding directions α.

Subtracting this long-range term from the electron-phonon coupling matrix element in Eq. 2.5.1 leaves a regular, short-ranged contribution that is amenable to *Wannier-Fourier* interpolation. After interpolating this contribution to arbitrary $\mathbf{k}$ and $\mathbf{q}$, the analytically evaluated long-range term is added back at the same points.

2.7 Momentum Relaxation Time and Charge-Carrier Mobility

Within the momentum-relaxation-time approximation, the mobility of conduction-band electrons or valence-band holes is the tensor

$$\mu_{ij} = -\frac{\sum_{n\mathbf{k}} v^{(i)}_{n\mathbf{k}} v^{(j)}_{n\mathbf{k}} \tau_{n\mathbf{k}} \frac{\partial f_{n\mathbf{k}}}{\partial \epsilon_{n\mathbf{k}}}}{\sum_{n\mathbf{k}} f_{n\mathbf{k}}}. \tag{2.7.1}$$

Here n is the carrier band index, $f_{n\mathbf{k}} \propto e^{-\frac{\epsilon_{n\mathbf{k}}}{k_B T}}$ is the *Maxwell-Boltzmann* occupation of a state with energy $\epsilon_{n\mathbf{k}}$, $v^{(i)}_{n\mathbf{k}} = \frac{\partial \epsilon_{n\mathbf{k}}}{\partial k_i}$, k_B is the *Boltzmann* constant, T is temperature, and $\tau_{n\mathbf{k}}$ is the momentum relaxation time of a carrier in state $\psi_{n\mathbf{k}}$. The use of the *Maxwell-Boltzmann*, rather than *Fermi-Dirac*, distribution is justified by the assumption of very low carrier concentrations, as in pure, undoped semiconductor samples [21]. In the low-concentration limit, the carrier relaxation time is

$$\begin{aligned}\frac{1}{\tau_{n\mathbf{k}}} = \frac{2\pi}{N_{q'}} \sum_{\mathbf{q},\nu,m} \sum_{\pm} |\gamma_{mn,\nu}(\mathbf{k},\mathbf{q})|^2 \left(n_{\nu\mathbf{q}} + \frac{1}{2} \mp \frac{1}{2}\right) \times \\ \times \delta\left(\epsilon_{n\mathbf{k}} \pm \omega_\nu(\mathbf{q}) - \epsilon_{m\mathbf{k}\pm\mathbf{q}}\right)(1 - cos\theta_{\mathbf{k},\mathbf{k}\pm\mathbf{q}}),\end{aligned} \tag{2.7.2}$$

where $n_{\nu\mathbf{q}}$ is the *Bose-Einstein* occupation of the phonon mode $\nu\mathbf{q}$, and $N_{q'}$ is the number of q-points in the dense interpolated grid. The final factor in the preceding expression is given by

$$cos\theta_{\mathbf{k},\mathbf{k}\pm\mathbf{q}} = \frac{\mathbf{v}_{n\mathbf{k}} \cdot \mathbf{v}_{m\mathbf{k}\pm\mathbf{q}}}{|\mathbf{v}_{n\mathbf{k}}| \cdot |\mathbf{v}_{m\mathbf{k}\pm\mathbf{q}}|}. \tag{2.7.3}$$

The delta function in Eq. 2.7.2 enforces energy conservation, while the sum over $\pm$ includes phonon absorption $(+)$ and emission $(-)$.

Calculating a carrier momentum relaxation time from Eq. 2.7.2 requires the electron-phonon or hole-phonon coupling matrix elements. Because they vary rapidly with carrier crystal momentum and phonon wave vector, many mobility studies evaluate them on predetermined, extremely dense k- and q-point grids, ranging from approximately 45^3 to 600^3, obtained by *Wannier-Fourier* interpolation from coarse grids of order 8^3 [23][24][25][26][27]. Interpolation onto grids of this size is computationally very demanding [4]. A method was therefore developed that evaluates the momentum relaxation time without using a predetermined dense q-point grid, substantially reducing the cost of carrier relaxation-time and mobility calculations [4]. The method converts the sum over phonon wave vectors in Eq. 2.7.2 into an integral in spherical coordinates and rewrites the delta function as

$$\delta[g(q_r, q_\varphi, q_\theta)] = \sum_i \frac{\delta^{(3)}(\mathbf{q} - \mathbf{q}_i)}{|\nabla g(\mathbf{q}_i)|}, \tag{2.7.4}$$

where i labels the zeros of the function

$$g(q_r, q_\varphi, q_\theta) = \epsilon_{n\mathbf{k}} - \epsilon_{n\mathbf{k}\pm\mathbf{q}} \pm \omega_\nu(\mathbf{q}). \tag{2.7.5}$$

The integration is carried out for N_Ω phonon-wave-vector directions $(q^s_\varphi, q^s_\theta)$, $s \in \{1, ..., N_\Omega\}$, selected randomly by *Monte Carlo* sampling. For each direction, the delta function reduces the integral to a sum over radial components $q^i_r(q^s_\varphi, q^s_\theta)$ that are zeros of g. Consequently, the electron-phonon coupling matrix elements need be interpolated from the coarse grid only to the q-points with spherical coordinates $(q^i_r(q^s_\varphi, q^s_\theta), q^s_\varphi, q^s_\theta)$. The average carrier momentum relaxation time along a selected phonon-wave-vector direction can thus be approximated using far fewer *Wannier-Fourier*-interpolated coupling matrix elements.

3 Material Studied: Wurtzite ZnO

This section describes the crystal structure of ZnO, the semiconductor for which carrier momentum relaxation times and mobilities were calculated.

Zinc oxide crystallises in the wurtzite structure with space group $P6_3mc$ and point group C_{6v} [28] (Figure 3.1). Its crystal structure can be described as two interpenetrating hexagonal close-packed (HCP) sublattices of equal dimensions, one formed by Zn^{2+} and the other by O^{2-}. The ions are tetrahedrally coordinated, and the two sublattices are displaced relative to one another by a distance u along the z axis (Figure 3.2).

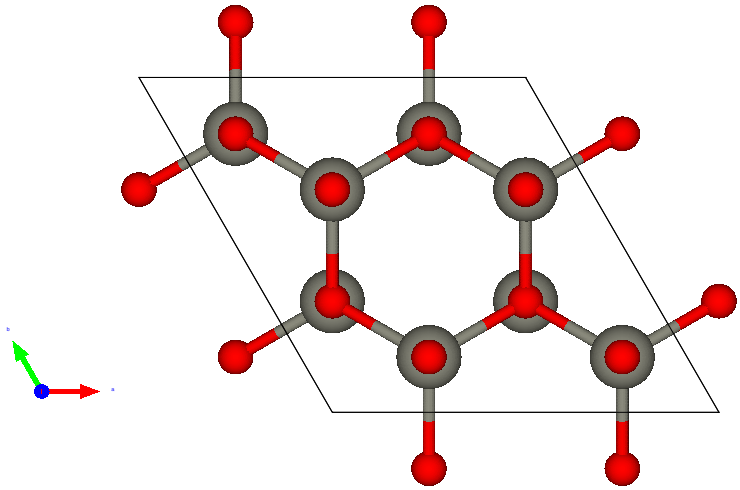

Figure 3.1: Projection of the wurtzite ZnO crystal structure onto the plane normal to the primitive lattice vector **c**, i.e. the plane spanned by the primitive lattice vectors **a** and **b**. Zn^{2+} ions are shown as grey spheres and O^{2-} ions as red spheres.

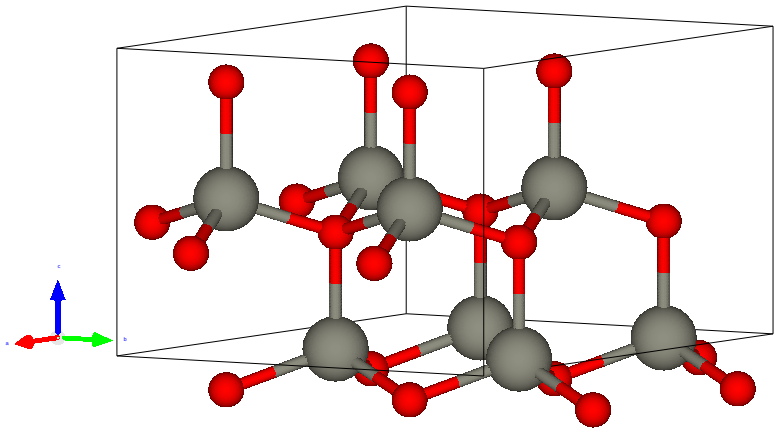

Figure 3.2: Crystal structure of wurtzite ZnO.

The primitive unit cell is shown in Figs. 3.3 and 3.4. The conventional unit cell contains two zinc atoms and two oxygen atoms. The in-plane primitive lattice vectors forming the hexagonal structure are denoted by **a** and **b**. They have equal magnitudes a and enclose an angle of 120°, while the primitive vector **c** normal to their plane has

magnitude c. The ZnO structure is close to ideal: $c/a \approx 1.6081(7)$ [28], compared with $c/a \approx 1.63299$ for an ideal wurtzite crystal. Zn and O atoms are aligned along **c**, giving rise to spontaneous polarisation in this direction. Wurtzite ZnO lacks inversion symmetry.

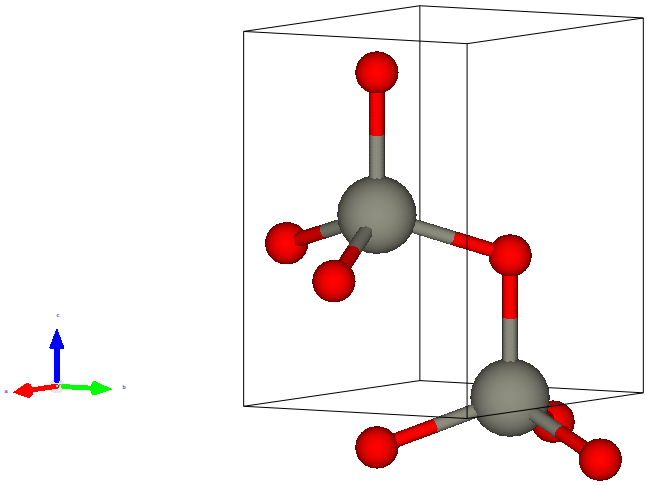

Figure 3.3: Primitive unit cell of wurtzite ZnO.

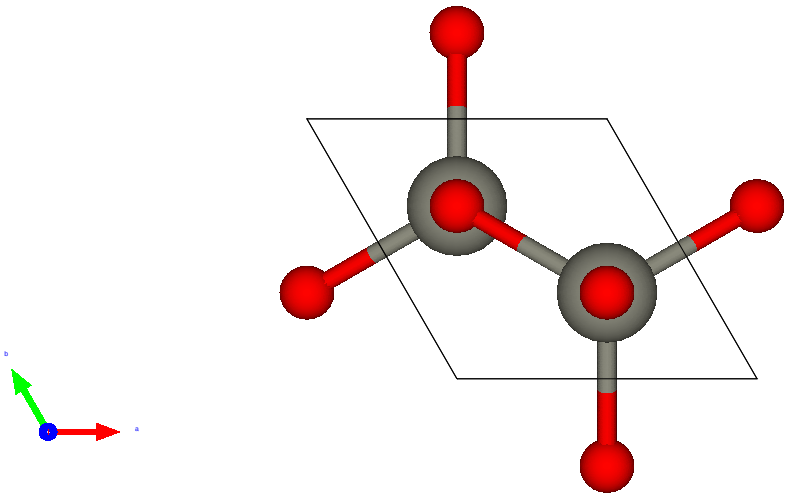

Figure 3.4: Primitive unit cell of wurtzite ZnO projected onto the plane normal to **c**, i.e. the plane containing the primitive lattice vectors **a** and **b**.

4 Method

This section describes the electronic-structure and phonon calculations, the construction of *Wannier* functions, and the evaluation of electron-phonon coupling matrix elements using *Wannier-Fourier* interpolation for polar semiconductors. It then presents the procedures used to calculate carrier momentum relaxation times and mobilities. The final part of the methodology specifies where and why spin-orbit coupling was included.

4.1 Electronic-Structure Calculations

The DFT electronic-structure calculations for wurtzite ZnO were performed using ABINIT [29][30]. The *Perdew-Burke-Ernzerhof* (PBE) generalised gradient approximation to the exchange-correlation functional was employed [16]. Standard-accuracy norm-conserving pseudopotentials from the PseudoDojo project were used [31]: scalar-relativistic ONCVPSP v0.4.1 pseudopotentials for calculations without spin-orbit coupling (SOC), and fully relativistic ONCVPSP v0.4 pseudopotentials for calculations with SOC. In these pseudopotentials, the $1s$, $2s$, and $2p$ electrons of Zn are treated as core electrons, whereas only the $1s$ electrons of O are treated as core states. Thus, the electronic structure is calculated explicitly for 20 electrons per Zn atom and 6 per O atom. Because the primitive wurtzite ZnO unit cell contains two atoms of each element, 52 valence electrons are included. A calculation without SOC consequently contains 26 valence bands, since two opposite-spin electrons may occupy each *Kohn-Sham* state $\psi_{n\mathbf{k}}(\mathbf{r})$. With SOC, the eigenstates of the *Kohn-Sham* Hamiltonian are spinors $\psi_{n\mathbf{k}}(\mathbf{r}) = \begin{pmatrix} \psi^{\uparrow}_{n\mathbf{k}}(\mathbf{r}) \\ \psi^{\downarrow}_{n\mathbf{k}}(\mathbf{r}) \end{pmatrix}$, each accommodating at most one electron. The number of valence bands is therefore doubled to 52.

Experimental lattice constants from the literature were used in all calculations [28], while the atomic positions within the unit cell, expressed as *Wyckoff* coordinates in the primitive-lattice basis, were obtained from the *Materials Project* database [32]. The first *Brillouin* zone was sampled using a $6 \times 6 \times 4$ Γ-centred *Monkhorst-Pack* k-point grid [17]. The plane-wave kinetic-energy cutoff was 45 Ha.
Details of the electronic-structure convergence tests are given in Appendix A. Following the self-consistent calculation on the grid specified above, non-self-consistent electronic-structure calculations were performed by diagonalising the *Kohn-Sham* Hamiltonian in the plane-wave basis. These calculations yielded eigenstates and eigenvalues at crystal momenta $\mathbf{k}$ along a path connecting selected high-symmetry points in the first *Brillouin* zone (Figure 4.1). The high-symmetry-point coordinates and labels were generated with *SeeK-path* through *Materials Cloud* [33][34].

4.2 Influence of Spin-Orbit Coupling on the Band Structure

The DFT calculations with and without SOC were used to plot the band structures in Fig. 4.2 along the high-symmetry path in the first *Brillouin* zone shown in Fig. 4.1. The bands most relevant to momentum-relaxation-time and mobility calculations are the uppermost valence bands within several k_BT of the *Fermi* level and the lowest conduction bands within several k_BT of the conduction-band minimum, particularly near Γ (Figure 4.3). Figures 4.2 and 4.3 show that, without SOC, the relevant bands are the three uppermost valence bands and the lowest conduction band; with SOC, they are the corresponding *Kramers* pairs. To quantify the influence of SOC on these states, inverse

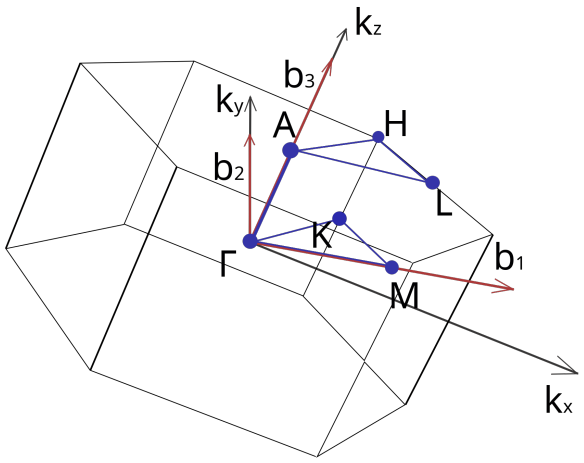

Figure 4.1: First *Brillouin* zone of wurtzite ZnO. The blue line marks the path connecting selected high-symmetry points used to plot the band structure. The reciprocal-lattice vectors are denoted by $\mathbf{b}_1$, $\mathbf{b}_2$, and $\mathbf{b}_3$.

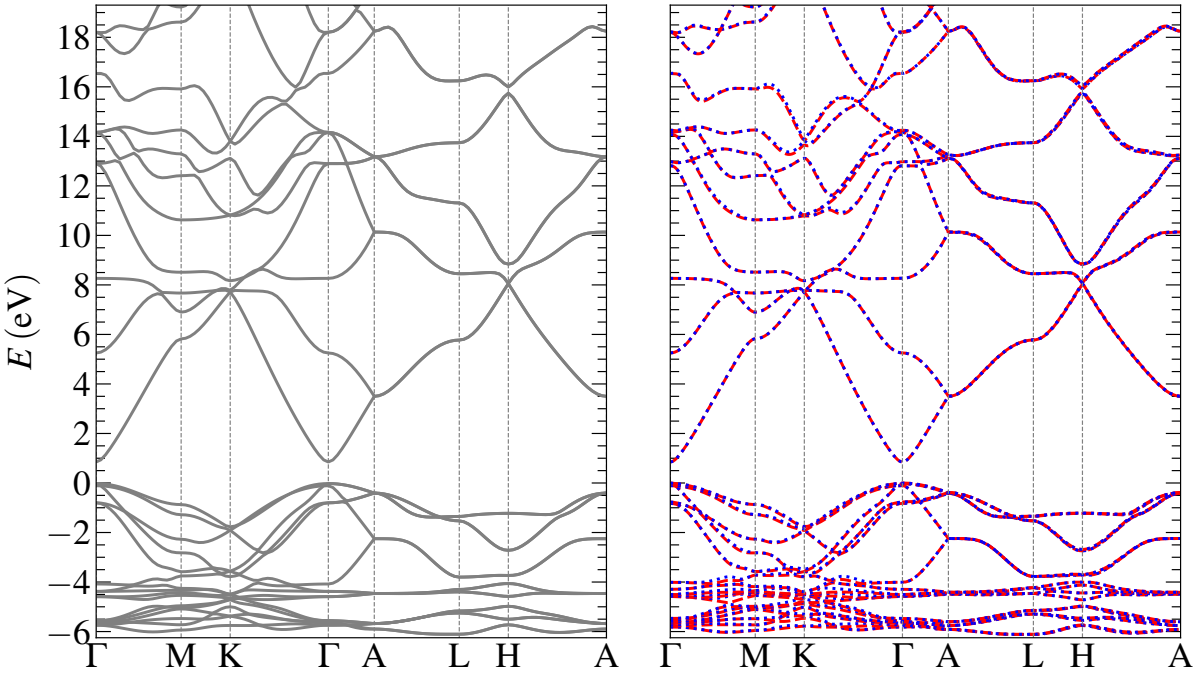

Figure 4.2: Band structures obtained from DFT calculations without SOC (left) and with SOC (right). In the SOC band structure, odd-indexed bands are shown as blue dotted lines and even-indexed bands as red dashed lines.

effective-mass tensors were calculated for the two uppermost valence bands and the lowest conduction band obtained without SOC, as well as for their corresponding spin-split pairs from the calculations with SOC.

Figure 4.3 also shows that including SOC lifts the twofold degeneracy of the *Kohn-Sham* eigenvalues associated with the two uppermost valence bands at Γ, producing spin-orbit splitting [20].

4.2.1 Charge-Carrier Effective-Mass Calculations

DFT calculations were used to obtain the *Kohn-Sham* eigenvalues of the two uppermost valence bands, $n = 25$ and $n = 26$, and the lowest conduction band, $n = 27$, along three high-symmetry directions near Γ: Γ − K, equivalent to $\mathbf{k}_x$; Γ − M, equivalent to $\mathbf{k}_y$; and Γ − A, equivalent to $\mathbf{k}_z$. The eigenvalues were calculated at equally spaced k-points along each reciprocal-space coordinate axis, beginning at Γ. For every band, the *Kohn-Sham* eigenvalue associated with $\psi^{KS}_{n\mathbf{k}}$ was plotted against $\mathbf{k}^2/2$ separately along $\mathbf{k}_x$, $\mathbf{k}_y$, and $\mathbf{k}_z$. The slopes of straight lines fitted to these points are the diagonal elements m^{-1}_{ii} of the inverse effective-mass tensor, where i labels the three reciprocal-space directions. One such fit is shown in Fig. 4.4.

The off-diagonal elements $(m^{-1})_{ij}$ were calculated similarly. The eigenvalues corresponding to *Kohn-Sham* states $\psi_{n\mathbf{k}}$, with $\mathbf{k}$ along $\mathbf{k}_i + \mathbf{k}_j$ for $i, j \in \{x, y, z\}$ and $i \neq j$, were plotted against $k_i^2/2$. Straight-line fits yielded slopes c_{ij}, from which the off-diagonal elements were calculated as

$$\left(m^{-1}\right)_{ij} = \frac{c_{ij} - (m^{-1})_{ii} - (m^{-1})_{jj}}{2}. \tag{4.2.1}$$

The same procedure was applied to the *Kramers* pairs corresponding to the two uppermost valence bands and the lowest conduction band in the calculations with SOC.

Because the wurtzite structure lacks spatial-inversion symmetry, bands belonging to a *Kramers* pair with indices $2n$ and $2n + 1$ strictly satisfy

$$E_{2n}(\mathbf{k}) = E_{2n+1}(-\mathbf{k}). \tag{4.2.2}$$

These individual bands need not possess k-space inversion symmetry near Γ. When they do not, an effective mass defined through the curvature of a single band at Γ is not physically meaningful because the curvature is not well defined there. New pairs of functions of crystal momentum, E_{na} and E_{nb}, are therefore constructed from the *Kramers* pair $2n$, $2n + 1$ according to

$$\text{For } E_{2n+1}(\mathbf{k}) \geq E_{2n}(\mathbf{k}): \quad \begin{cases} E_{na}(\mathbf{k}) = E_{2n}(\mathbf{k}) \\ E_{nb}(\mathbf{k}) = E_{2n+1}(\mathbf{k}) \end{cases} \qquad \text{For } E_{2n}(\mathbf{k}) > E_{2n+1}(\mathbf{k}): \quad \begin{cases} E_{na}(\mathbf{k}) = E_{2n+1}(\mathbf{k}) \\ E_{nb}(\mathbf{k}) = E_{2n}(\mathbf{k}) \end{cases}$$

For brevity, these constructed functions will hereafter be referred to as band pairs, although they are not individual *Kramers* pairs in the strict sense. This convention does not affect the calculated inverse effective-mass tensors because the crystal momenta used in the calculation can be chosen such that $\mathbf{k} \in \mathbb{R}^3_{\geq 0}$, as was done here.

For the two uppermost valence-band pairs in the calculations with SOC, the energy ranges over which a straight line could be fitted while retaining stable inverse effective-mass elements were substantially reduced. Here stability refers to the sensitivity of a

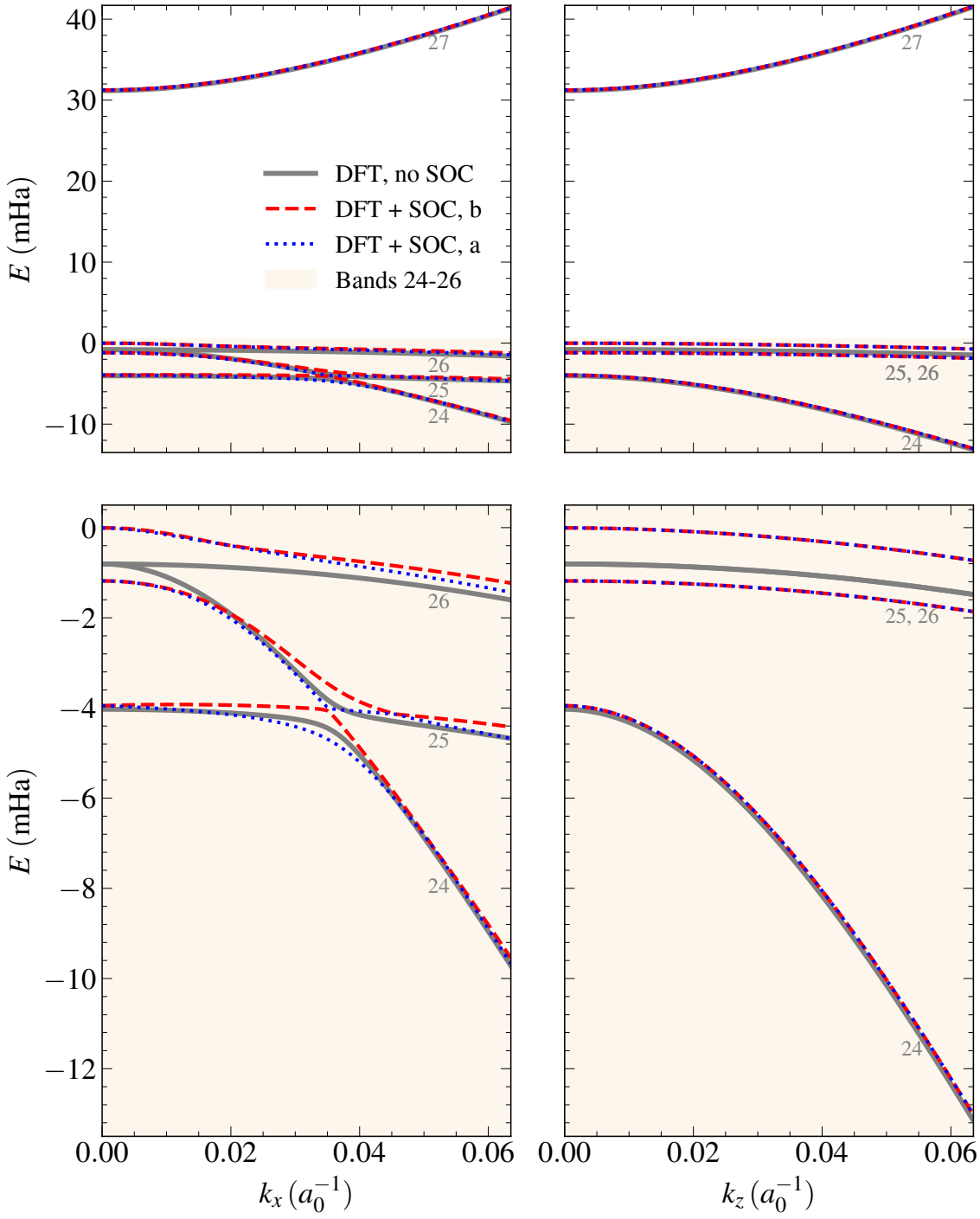

Figure 4.3: Dispersion relations near Γ for the three uppermost valence bands (24, 25, and 26) and the lowest conduction band (27), along $\Gamma - \mathrm{K}$, equivalent to $\mathbf{k}_x$ (left), and $\Gamma - \mathrm{A}$, equivalent to $\mathbf{k}_z$ (right). Results without SOC are shown as solid grey lines. In the calculations with SOC, the lower-energy member of each corresponding pair is shown by a blue dotted line and the higher-energy member by a red dashed line. The upper panels show all three valence bands, or three *Kramers* pairs with SOC, and the lowest conduction band, or one *Kramers* pair with SOC. The lower panels are vertical enlargements of the shaded valence-band regions in the upper panels.

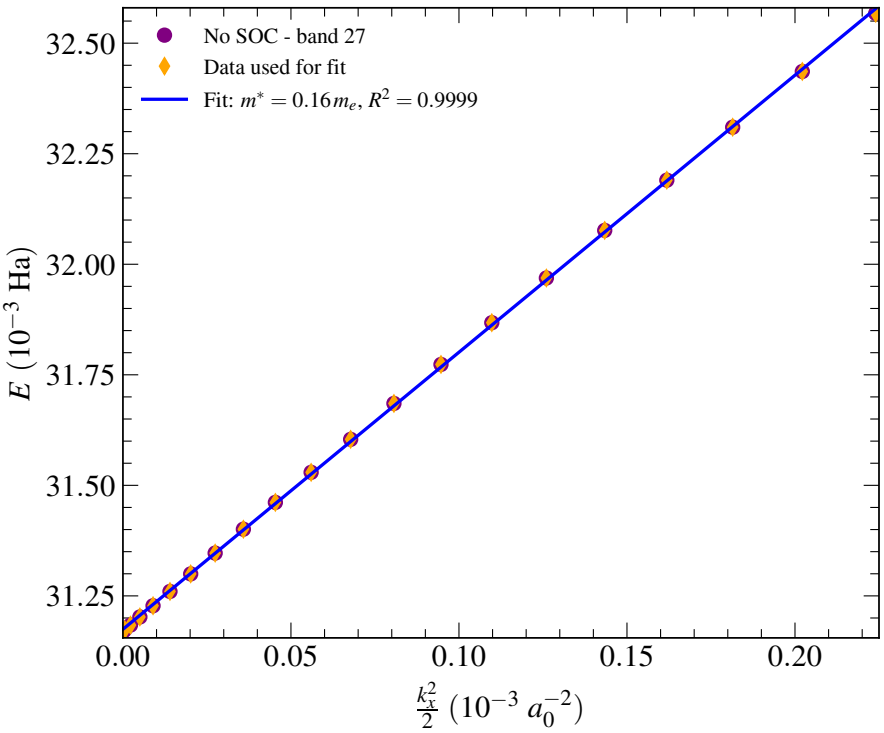

Figure 4.4: *Kohn-Sham* eigenvalues from DFT calculations without SOC for the state $\psi_{n\mathbf{k}}$ in the lowest conduction band, $n = 27$, plotted against $\mathbf{k}^2/2$. The crystal momenta lie along $\mathbf{k}_x$, equivalent to $\Gamma - \mathrm{K}$. A straight line is fitted through the points; the electron effective mass m^* along x is the inverse of its slope.

fitted tensor element to the distance from Γ of the outermost point included in the fit. An example is shown in Fig. 4.5.

Without SOC, the inverse effective-mass tensors of the two uppermost valence bands and the lowest conduction band are diagonal to within numerical precision. Their diagonal elements can therefore be inverted directly to obtain the carrier effective masses along the corresponding directions. With SOC, some valence-band inverse effective-mass tensors contain non-zero off-diagonal elements that mix the direction parallel to the primitive vector **c** with directions normal to it. Diagonalising these tensors showed that, although the two in-plane principal axes rotate within the plane normal to **c**, one remains in that plane and the other deviates from it by less than 5°. Similarly, the third axis deviates from **c** by less than 5°. Effective masses along the principal axes, obtained as the inverses of the eigenvalues of the inverse effective-mass tensor, differ by less than 10% from the inverses of the corresponding diagonal tensor elements.

For a qualitative assessment of the influence of SOC on the carrier effective masses, it is therefore sufficient to compare the inverses of the diagonal tensor elements obtained without SOC directly with the corresponding values for the associated band pairs obtained with SOC.

Because the effective-mass tensors of the two uppermost valence bands differ substantially along some directions between calculations with and without SOC (Table 5.1, Appendix B), and because SOC produces splitting at Γ, SOC was included in all subsequent calculations except those of the high-frequency relative dielectric tensor and *Born* effective charges, as explained in Section 4.4.

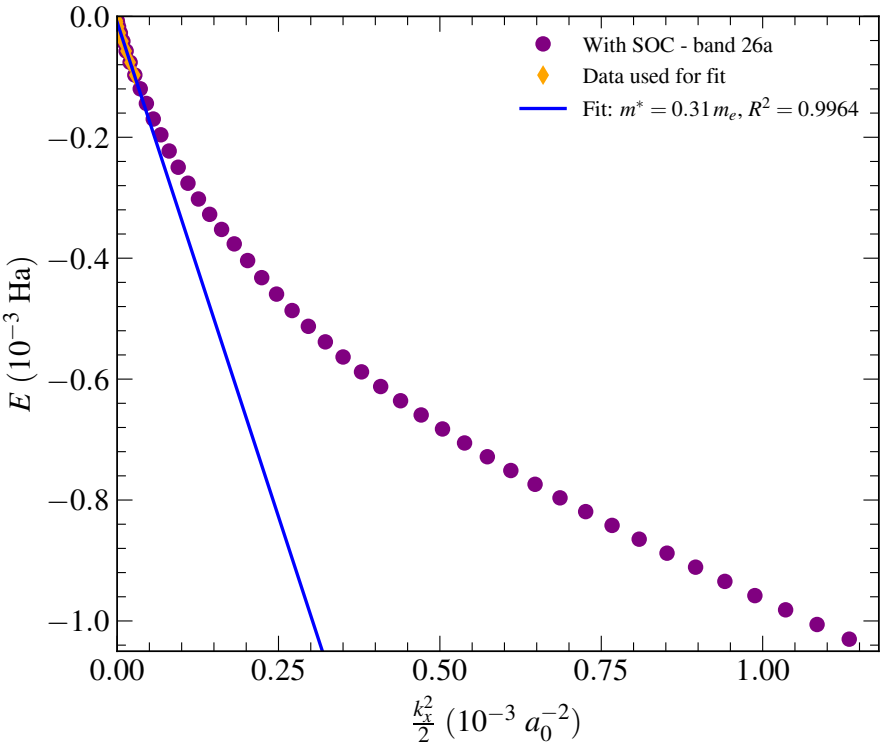

Figure 4.5: *Kohn-Sham* eigenvalues from calculations with SOC for states $\psi_{n\mathbf{k}}$ of band $n = 26a$, plotted against $k_x^2/2$. The crystal momenta lie along $\mathbf{k}_x$. A straight line is fitted through the points for which the slope remains stable, shown as orange diamonds.

4.3 Construction of Maximally Localised *Wannier* Functions

Maximally localised *Wannier* functions were constructed using WANNIER90 [35], called as a library from ABINIT. The construction included 24 *Kramers* pairs obtained from the DFT calculations with SOC: the uppermost 16 valence-band pairs and the lowest 8 conduction-band pairs. The standard disentanglement procedure was used for entangled bands [36]. The "frozen energy window" [35], i.e. the energy range in which the original *Kohn-Sham* states are preserved when constructing the MLWF subspace, is shown in Fig. 4.6. The window was chosen to maximise agreement between the Wannier-interpolated and directly calculated DFT bands for the three uppermost valence-band pairs and the lowest conduction-band pair.

4.4 High-Frequency Relative Dielectric Tensor and *Born* Effective Charges

The high-frequency relative dielectric tensor $\hat{\varepsilon}_\infty$ and the *Born* effective-charge tensors $\hat{Z}^*$(Zn) and $\hat{Z}^*$(O) were calculated using ABINIT [37][38][39]. These calculations combine a DFT electronic-structure calculation with a DFPT linear-response calculation. Converging the elements of $\hat{\varepsilon}_\infty$, $\hat{Z}^*$(Zn), and $\hat{Z}^*$(O) often requires a denser k-point grid than is needed to converge the *Kohn-Sham* energies [6]. The computational cost therefore increases rapidly with the number of k-points used to sample the first *Brillouin* zone (Figure D.1). At a fixed number of bands, including SOC increases the cost by several-fold.

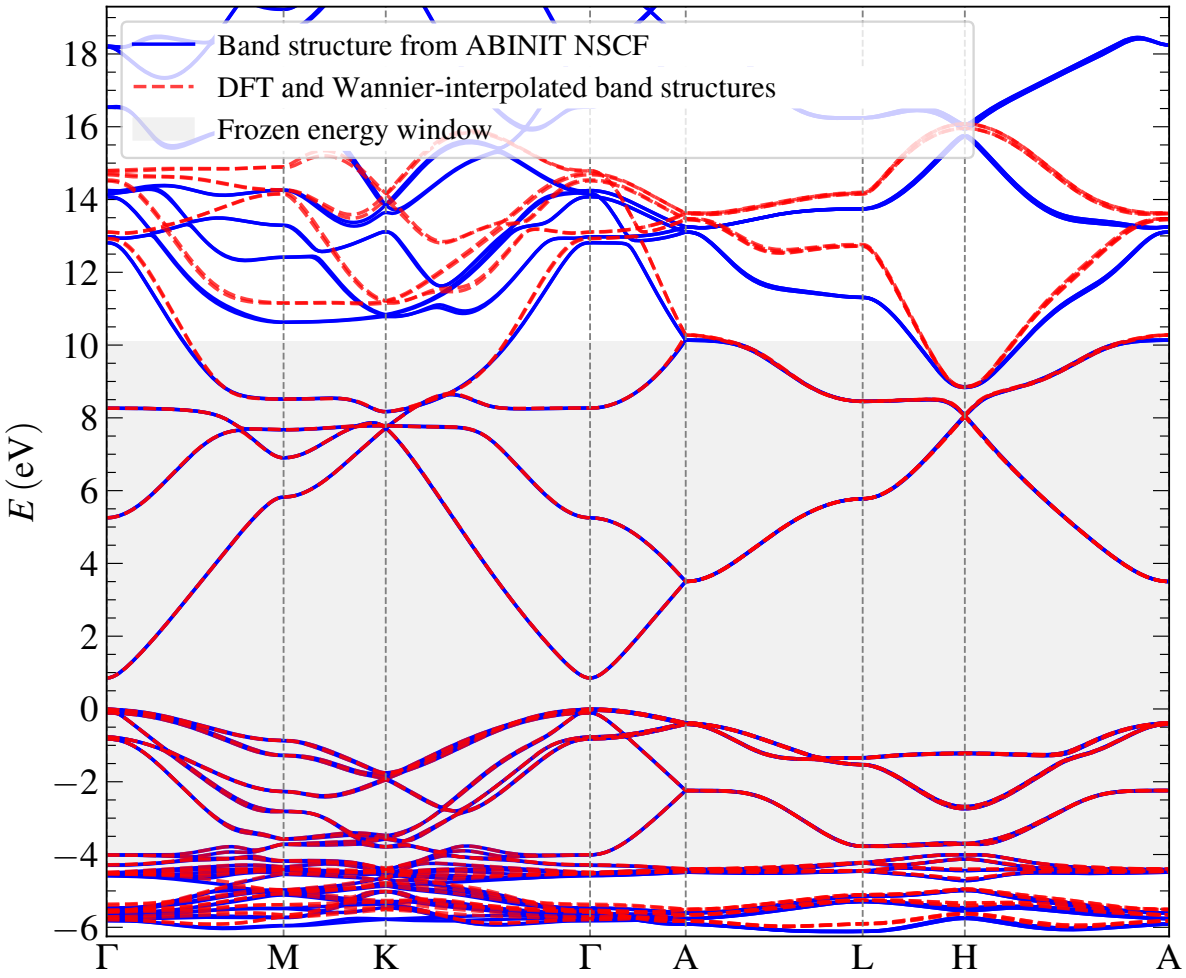

Figure 4.6: ZnO band structure obtained directly from DFT calculations with spin-orbit coupling (solid blue lines) and by *Wannier* interpolation (dashed red lines). The shaded region is the "frozen energy window" [35].

Before undertaking the convergence tests, the effect of SOC was assessed on a coarse $6 \times 6 \times 4$ k-point grid. The high-frequency dielectric and *Born* effective-charge tensors obtained with and without SOC differed only slightly (Table D.1); the subsequent convergence tests were therefore performed without SOC (Figure A.3, Figure A.4, and Figure A.5). The values used in the remaining calculations were obtained on a Γ-centred $18 \times 18 \times 12$ *Monkhorst-Pack* grid.

4.5 Phonon Dispersions and Carrier–Phonon Coupling Matrix Elements

Dynamical matrices and phonon frequencies were calculated with ABINIT on a coarse Γ-centred 6×6×4 *Monkhorst-Pack* q-point grid using DFPT [37][38]. Brillouin-zone symmetries were not used in the underlying DFT electronic-structure calculation. Convergence of the phonon frequencies was tested at selected high-symmetry q-points (Tables A.1, A.2, and A.3).

The resulting coarse-grid phonon dispersions were interpolated to arbitrary wave vectors $\mathbf{q}$ in the first *Brillouin* zone while accounting for the non-analyticity of the dynamical

matrix near Γ. The interpolation used code developed and adapted by Dr. Nenad Vukmirović from the code collection available on *Zenodo* [40], together with the previously calculated high-frequency dielectric and *Born* effective-charge tensors. The phonon dispersions were plotted along the same high-symmetry path as the electronic band structure and compared with experiment (Figure 5.1).

Electron-phonon and hole-phonon coupling matrix elements were calculated with code from the same collection [40], using the inputs employed for the phonon interpolation together with the unitary *Bloch*-function mixing matrices obtained from ABINIT and WANNIER90. The implemented procedure is based on *Wannier-Fourier* interpolation and includes the long-range *Fröhlich* interaction [41][42]. The magnitude of the coupling between an electron at $\mathbf{k} = \mathbf{0}$ in the lowest conduction band and an electron at $\mathbf{k}+\mathbf{q}$ in the same band was plotted as a function of the wave vector $\mathbf{q}$ for a phonon in branch ν. The selected phonon wave vectors follow the same high-symmetry path used for the electronic band structure and phonon dispersion (Figure 5.2 and Figure 5.3).

4.6 Charge-Carrier Momentum Relaxation Times

Carrier momentum relaxation times were calculated with code from the collection cited above [40], using the method of Ref. [4], which does not rely on predetermined dense k- and q-point grids. Calculations were performed for holes in the three uppermost valence-band *Kramers* pairs and electrons in the lowest conduction-band *Kramers* pair. The long-range *Fröhlich* interaction and carrier scattering mediated by all 12 phonon branches were included. For electrons, the relaxation time was expressed as a function of the excess energy above the conduction-band minimum, $\epsilon_{n\mathbf{k}} - \epsilon_{m\mathbf{0}}$, where m labels the lowest conduction band. For holes, it was expressed as a function of the energy below the valence-band maximum, $\epsilon_{m'\mathbf{0}} - \epsilon_{n\mathbf{k}}$, where m' labels the uppermost valence band. Electrons in the lowest conduction-band pair were allowed to scatter into states of that same pair, while holes in the three uppermost valence-band pairs were allowed to scatter among states of all three pairs.

For a carrier in band n with crystal momentum $\mathbf{k}$ scattering into a state in band m with momentum $\mathbf{k}+\mathbf{q}$, the method finds the zeros of the function g in Eq. 2.7.5 for N_Ω randomly selected directions (q_θ, q_φ), where $(q_r, q_\theta, q_\varphi)$ are the spherical coordinates of $\mathbf{q}$. The value $N_\Omega = 100$ was used.

Solutions of $g(q_r(q_\varphi, q_\theta)) = 0$ were sought numerically on $q_r \in [q_{min}, q_{max}]$, where q_{max} is the distance from Γ to the edge of the first Brillouin zone along the direction (q_θ, q_ϕ) and $q_{min} = 10^{-4} a_0^{-1}$. The interval $[q_{min}, q_{max}]$ was divided into $N_1 = 20$ closed subintervals with shared boundaries. Their boundaries form a geometric progression, giving the highest subinterval density near Γ. Wherever g had opposite signs at the two boundaries, its zero was located by $N_2 = 10$ bisection iterations. At each resulting q-point, the electron-phonon or hole-phonon coupling matrix elements were calculated as described in the preceding subsection.

To plot the relaxation times as functions of excess carrier energy, crystal momenta were selected along $\mathbf{k}_x$, $\mathbf{k}_y$, and $\mathbf{k}_z$, corresponding to Γ − K, Γ − M, and Γ − A, respectively. The k-points were equally spaced along each direction. Relaxation-time calculations were performed from 100 K to 500 K in steps of 50 K.

4.7 Temperature Dependence of Charge-Carrier Mobility

The temperature-dependent mobility calculations apply Eq. 2.7.1 to the momentum relaxation times obtained by the procedure above. For the relaxation-time-versus-energy plots, the crystal momenta $\mathbf{k}$ were selected along predetermined directions, thereby fixing the states $\psi_{n\mathbf{k}}$ to be evaluated. In the mobility calculations, by contrast, both $\mathbf{k}$ and the band n within the selected scattering manifold were chosen randomly by *Monte Carlo* sampling, with the k-point selection optimised for the state-occupation distribution at a reference temperature T_{ref}. Each individual valence- or conduction-band mobility calculation used $N_k = 100$ pairs $(\mathbf{k}, n)$. For each band group, the calculation was repeated ten times with different random-number seeds (Figs. C.1 and C.2). The states sampled at $T_{ref} = 500\,\mathrm{K}$ were used to evaluate the mobility tensors from 100 K to 500 K in steps of 50 K. Means and standard deviations were determined at every temperature, and the diagonal tensor elements were plotted as functions of temperature (Figs. 5.10 and 5.11). One additional calculation with $N_k = 1000$ was performed for each of the two band groups. These results were compared with the corresponding averages of the ten $N_k = 100$ calculations to provide an additional convergence check (Figs. C.3 and C.4).

5 Results and Discussion

This section presents the principal results of the calculations, many of which are compared with experiment. They include phonon dispersions, electron-phonon coupling matrix elements, and charge-carrier momentum relaxation times and mobilities in ZnO. The results are analysed in the context of the models and approximations employed, previous theoretical results for polar semiconductor crystals, and reliable experimental data where available.

5.1 DFT and DFPT Calculations

Table 5.1 lists the hole effective masses in the two uppermost valence bands, 25 and 26, and the electron effective mass in the lowest conduction band, 27, obtained from DFT calculations without spin-orbit coupling. The off-diagonal elements of the inverse effective-mass tensors are at least three orders of magnitude smaller than their corresponding diagonal elements and are therefore effectively zero (Table B.1). The tensors are consequently almost diagonal, so the effective masses along the coordinate axes are the inverses of the corresponding diagonal elements. Equal values are obtained along the two mutually orthogonal directions normal to **c**; the effective masses are therefore isotropic in that plane.

Table 5.1 also gives the inverses of the diagonal elements of the inverse effective-mass tensors for the corresponding band pairs obtained with SOC: 25a, 25b, 26a, 26b, 27a, and 27b. The tensors for bands 25a, 25b, and 26a are not diagonal (Table B.1), so these inverse diagonal elements are not, strictly speaking, the effective masses along the corresponding directions. Diagonalisation shows, however, that two principal axes remain almost in the plane normal to **c**, deviating by less than 5°, although they rotate within that plane by approximately 45°. The inverses of the tensor eigenvalues differ by less than 10% from the inverses of the corresponding diagonal elements. Thus, for the two uppermost valence bands, SOC transforms parabolic bands into ellipsoidal, anisotropic bands.

Table 5.1: Inverses of the diagonal elements of the inverse effective-mass tensors, in units of the free-electron mass m_0, for the two uppermost valence bands and the lowest conduction band. Results without SOC are compared with those for the corresponding lower-energy (a) and higher-energy (b) band partners obtained with SOC. Directions normal and parallel to **c** are denoted by $\perp$ and $\parallel$, respectively.

Band (n)	Direction	Without SOC	With SOC - a	With SOC - b
25 (v)	$\perp$	0.18	0.27	0.30
	$\parallel$	3.0	3.0	3.0
26 (v)	$\perp$	2.5	0.31	0.41
	$\parallel$	3.0	2.4	2.4
27 (c)	$\perp$, $\parallel$	0.16	0.16	0.16

For bands 25 and 26, the in-plane effective masses differ greatly between calculations with and without SOC. Without SOC, the two uppermost valence bands are degenerate at Γ, whereas SOC lifts this degeneracy (Fig. 4.3). Because SOC may therefore have a substantial effect on carrier mobility, all calculations required to obtain the final mobility

used DFT results with SOC, except for the high-frequency relative dielectric tensor and *Born* effective charges. Table 5.1 also shows that the lowest conduction band is isotropic and only negligibly affected by SOC.

Table 5.2 compares several quantities obtained from the DFT and DFPT calculations with experiment [28]. It gives the gaps between the lowest conduction-band pair, 27, and the three uppermost valence-band pairs, 26, 25, and 24, from DFT with SOC; the conduction-electron effective mass m_e^*/m_0, also obtained with SOC; and the components of the high-frequency relative dielectric tensor $\hat{\varepsilon}_\infty$ normal and parallel to **c**, $\varepsilon_\infty^\perp$ and $\varepsilon_\infty^\parallel$, obtained from DFT and DFPT without SOC. The off-diagonal tensor elements are zero. The calculated band gaps are substantially underestimated relative to experiment. This is a well-known limitation of DFT calculations employing LDA or GGA exchange-correlation functionals and also leads to an underestimated electron effective mass in the lowest conduction band. Electronic-structure calculations using the hybrid *Heyd-Scuseria-Ernzerhof* (HSE06) functional [43] generally yield substantially improved band gaps and carrier effective masses [44][3].

Table 5.2: Comparison of calculated and experimental values [28] for wurtzite ZnO: the band gaps E_g between the lowest conduction band and the three uppermost valence bands (26, 25, and 24), the conduction-electron effective mass m_e^*/m_0, and the components of the high-frequency relative dielectric tensor normal and parallel to **c**, $\varepsilon_\infty^\perp$ and $\varepsilon_\infty^\parallel$.

Quantity	Theory (this work)	Experiment
E_g (eV)	0.850, 0.882, 0.976	3.441, 3.443, 3.482
m_e^*/m_0	0.16	0.28
$\varepsilon_\infty^\perp$	4.97	3.70
$\varepsilon_\infty^\parallel$	5.00	3.75

SOC was found to have a negligible influence on the high-frequency relative dielectric and *Born* effective-charge tensors of ZnO. On the $6\times6\times4$ *Monkhorst-Pack* grid, the relative difference between values calculated with and without SOC is below 1% (Table D.1). The values obtained without SOC were therefore used subsequently because including SOC substantially increases the computational cost without materially improving the accuracy. Both tensors are diagonal and isotropic in the plane normal to **c**.

The calculated components $\varepsilon_\infty^\perp$ and $\varepsilon_\infty^\parallel$ are overestimated relative to experiment. The high-frequency dielectric response is highly sensitive to the exchange-correlation approximation used in the calculation [3].

Figure 5.1 shows the phonon dispersion along selected high-symmetry directions obtained from DFT and DFPT calculations with SOC, together with experimental data at high-symmetry points [45][46].

The calculated high-frequency relative dielectric and *Born* effective-charge tensors were used to interpolate the phonon dispersion from the coarse q-point grid and to treat the non-analyticity of the dynamical matrix near $\mathbf{q} = \mathbf{0}$. Because the non-analytic part is inversely proportional to the high-frequency relative permittivity [6], it is underestimated in the present calculations. Despite this, the calculated phonon dispersions agree reasonably well with experiment.

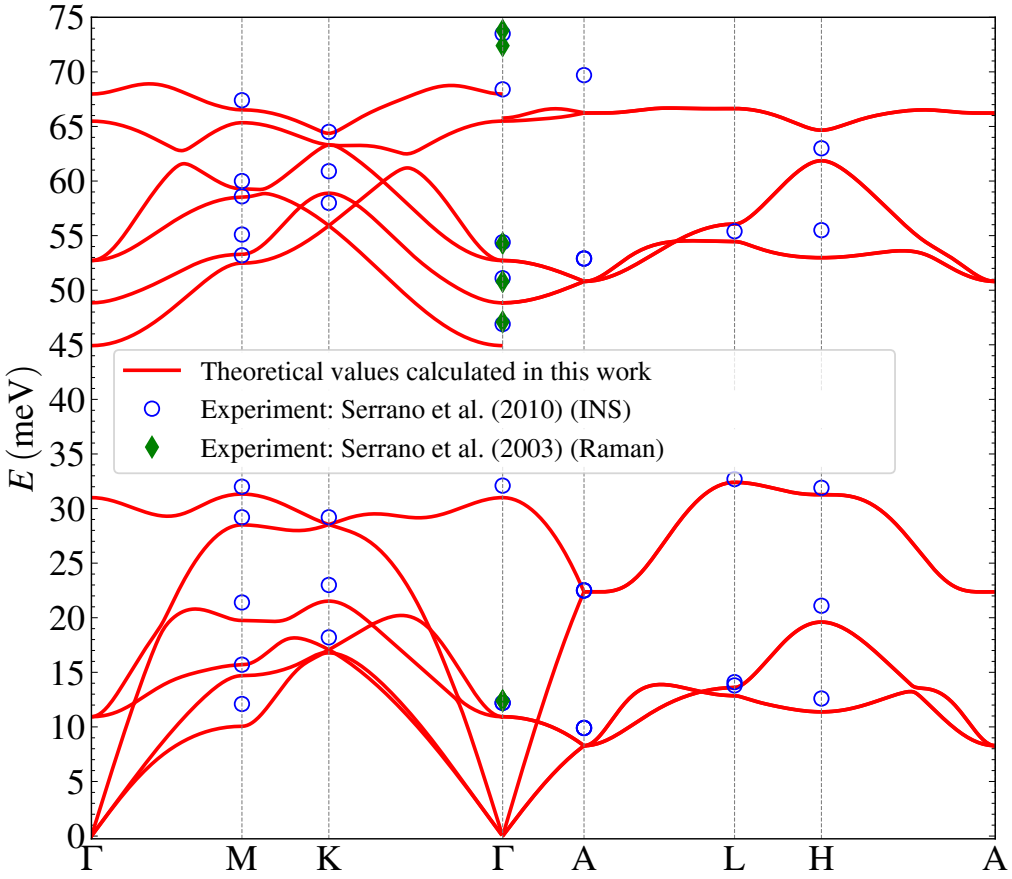

Figure 5.1: Phonon dispersions calculated in this work (red lines), together with experimental values at high-symmetry points obtained by inelastic neutron scattering [45] (blue circles) and Raman spectroscopy [46] (green diamonds).

5.2 Electron-Phonon Coupling Matrix Elements

Figure 5.2 shows the calculated magnitudes of the coupling matrix elements between an electron at $\mathbf{k} = \mathbf{0}$ in the lowest conduction band and an electron at $\mathbf{k} + \mathbf{q}$ in the same band, mediated by phonons in the three acoustic branches, as functions of $\mathbf{q}$. The phonon wave vectors follow a path connecting selected high-symmetry points in the first Brillouin zone.

Figure 5.3 shows the corresponding coupling magnitudes mediated by the three highest-energy optical branches, 10, 11, and 12. The selected wave vectors again follow the high-symmetry path, and the coupling magnitudes are plotted on a logarithmic vertical scale.

These plots illustrate the general behaviour of the coupling for electrons with $\mathbf{k} \approx \mathbf{0}$ scattering by acoustic phonons and the three highest-energy optical branches. Scattering by branch-12 phonons with $\mathbf{q} \approx \mathbf{0}$ is clearly the dominant channel. For phonon emission, this channel opens when the electron energy exceeds the conduction-band minimum by the energy of a branch-12 LO phonon near $\mathbf{q} = \mathbf{0}$. Figure 5.3 also shows that the coupling to these phonons varies extremely rapidly with wave vector near the centre of the first Brillouin zone, where its magnitude is largest.

Couplings mediated by the six lower-energy optical branches are not shown because

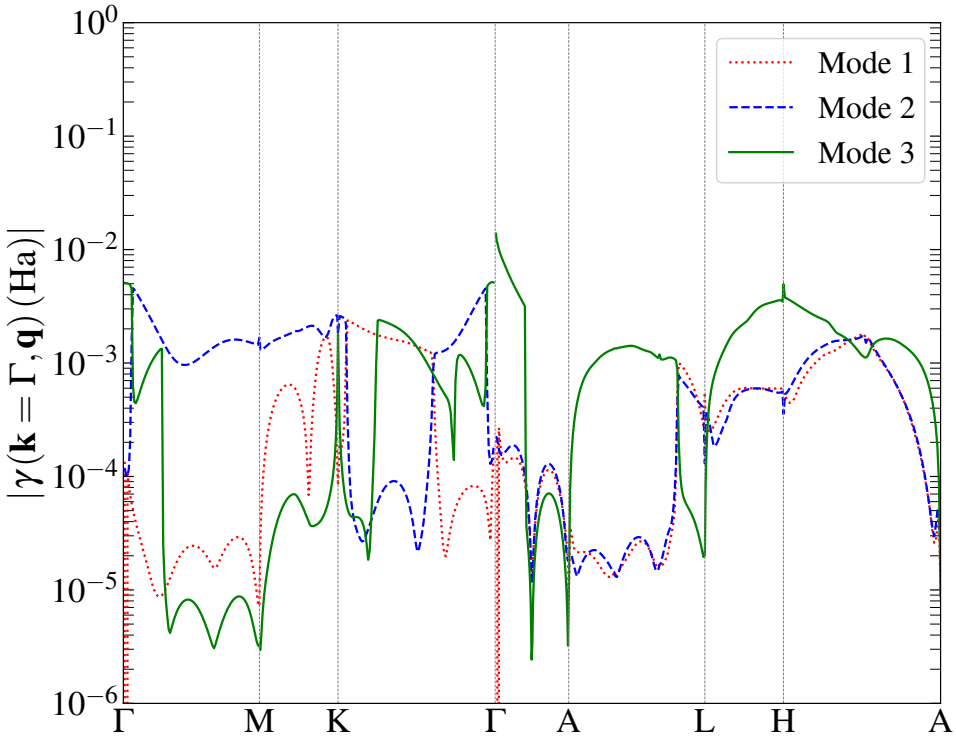

Figure 5.2: Calculated magnitudes of the electron-phonon coupling matrix elements between an electron in the lowest conduction band at Γ and an electron in the same band with crystal momentum $\mathbf{q}$, mediated by acoustic phonons with wave vector $\mathbf{q}$ along selected high-symmetry directions.

they are much smaller than those for the three highest-energy branches. The coupling for acoustic-phonon scattering is likewise much weaker than that for branch-12 optical phonons.

Comparison with results for the II-VI semiconductors ZnSe, ZnTe, CdSe, and CdTe [3] shows that, in wurtzite ZnO, the branch-12 LO-phonon coupling decreases much more slowly with phonon wave-vector magnitude. Conduction-electron scattering by branch-12 LO phonons at larger wave vectors is therefore more probable in ZnO than in those materials. Electron momentum relaxation times are consequently expected to be shorter when scattering by these phonons is the dominant relaxation mechanism.

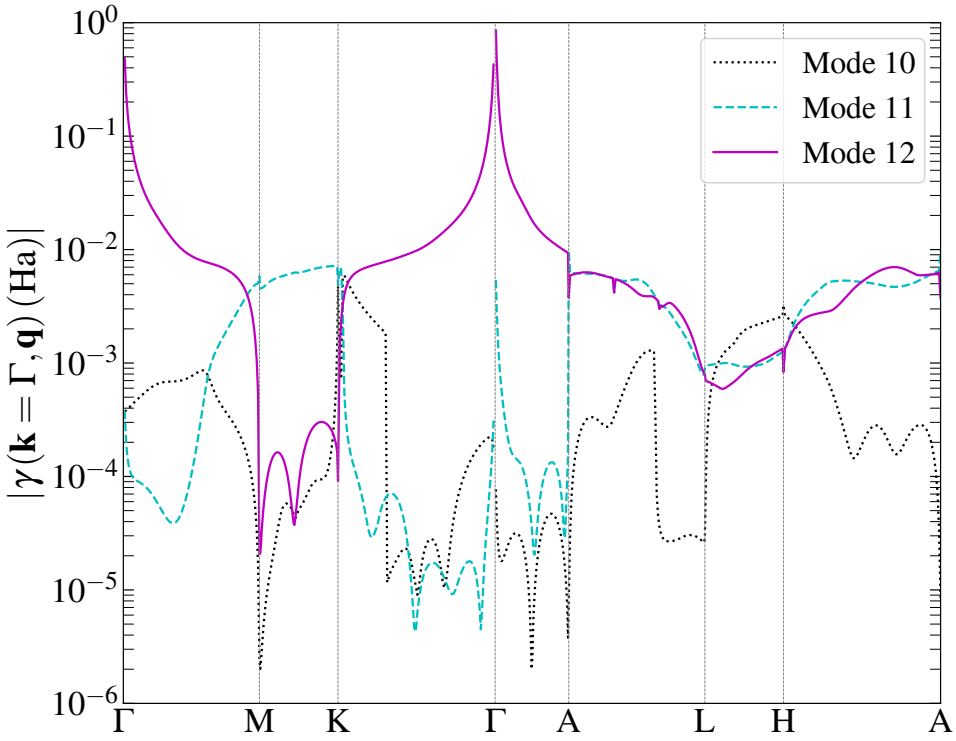

Figure 5.3: Calculated magnitudes of the electron-phonon coupling matrix elements between an electron in the lowest conduction band at Γ and an electron in the same band with crystal momentum $\mathbf{q}$, mediated by phonons in the three highest-energy optical branches along selected high-symmetry directions.

5.3 Charge-Carrier Momentum Relaxation Times

Figure 5.4 shows the calculated electron momentum relaxation time at $T = 300\,\mathrm{K}$ as a function of electron energy relative to the minimum of the lowest conduction band at Γ. The electrons belong to the lowest conduction-band pair near Γ, and their crystal momenta lie along $\Gamma - \mathrm{K}$, $\Gamma - \mathrm{M}$, or $\Gamma - \mathrm{A}$.

Because only $N_\Omega = 100$ randomly selected phonon-wave-vector directions were used, the plotted values are not fully converged, as expected [4]. More thoroughly converged calculations would produce smoother relaxation-time curves while preserving the same overall trend [4].

The overall energy dependence is the same along all three high-symmetry directions. This is consistent with the isotropy of the lowest conduction-band pair near Γ (Table 5.1 and Table B.1) and the near-isotropy of the high-frequency relative dielectric tensor (Table 5.2).

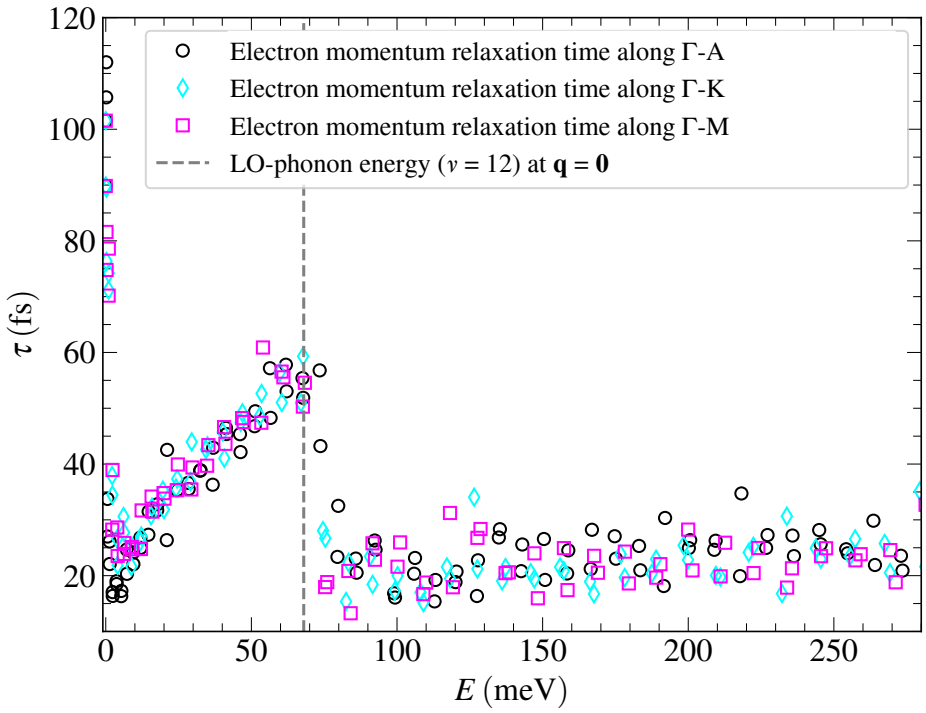

Figure 5.4: Calculated electron momentum relaxation time versus energy relative to the minimum of the lowest conduction band at $T = 300\,\mathrm{K}$. The electrons belong to the lowest conduction-band pair, with crystal momenta along $\Gamma - \mathrm{A}$ (black circles), $\Gamma - \mathrm{K}$ (turquoise diamonds), or $\Gamma - \mathrm{M}$ (pink squares). The dashed vertical line marks the energy of the branch-12 LO phonon at $\mathbf{q} = \mathbf{0}$.

The overall energy dependence agrees with that obtained for ZnTe using the same method [4], as well as with previous results for ZnSe, ZnTe, CdSe, and CdTe [3]. The relaxation times calculated for ZnO are substantially shorter than those reported for these materials.

Figure 5.5 shows the electron momentum relaxation time near Γ as a function of energy relative to the conduction-band minimum at $T = 100\,\mathrm{K}$, $300\,\mathrm{K}$, and $500\,\mathrm{K}$, combining crystal momenta along all three high-symmetry directions.

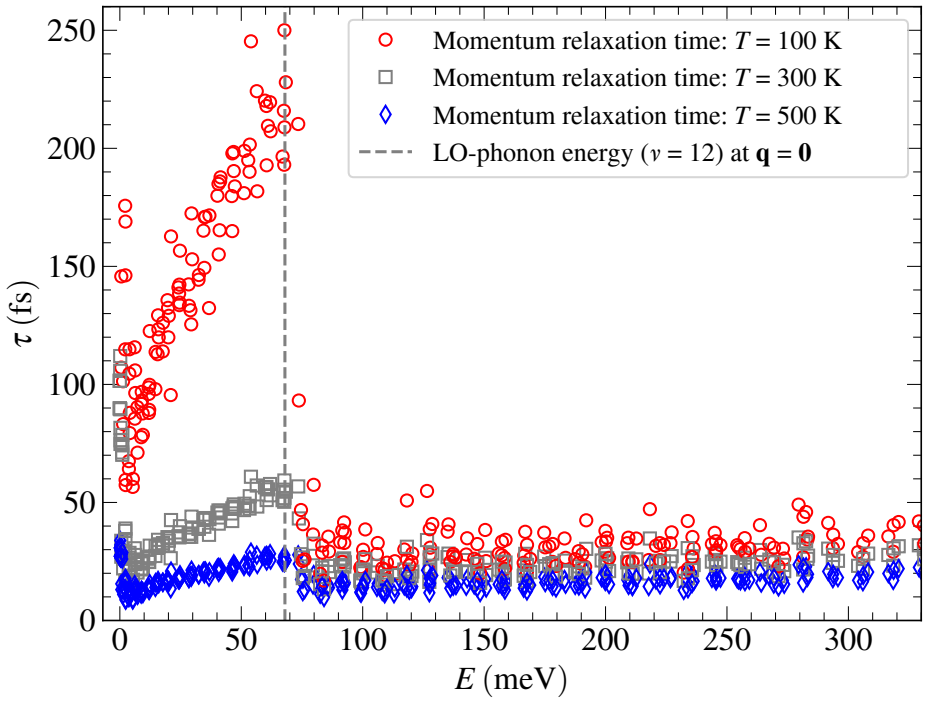

Figure 5.5: Calculated electron momentum relaxation time versus energy relative to the lowest conduction-band minimum at $T = 100\,\mathrm{K}$ (red circles), 300 K (grey squares), and 500 K (blue diamonds). The electrons belong to the lowest conduction-band pair and have crystal momenta along $\Gamma - \mathrm{A}$, $\Gamma - \mathrm{K}$, or $\Gamma - \mathrm{M}$. The dashed vertical line marks the energy of the branch-12 LO phonon at $\mathbf{q} = \mathbf{0}$.

Between a few meV and the branch-12 LO-phonon energy, the relaxation time increases with electron energy. As the electron momentum and energy increase, the phase space of final states accessible through emission grows and additional channels open because higher-energy phonon branches become available. In isolation, this effect would shorten the relaxation time. At the same time, the electron speed increases, so scattering by a given phonon produces a smaller relative change in the direction of $\mathbf{v}_\mathbf{k} = \mathbf{k}/m^*(\mathbf{k})$ than it does for a lower-momentum electron. In this sense, phonon scattering relaxes the momentum of faster electrons less effectively.

When the electron reaches the branch-12 LO-phonon energy, a small further increase in energy produces a sharp decrease in relaxation time. The branch-12 LO-phonon emission channel has opened, and its coupling is several orders of magnitude stronger than that of the other branches. The slight increase in relaxation time at still higher electron energies can again be explained by the decreasing fractional change in velocity direction during scattering.

The temperature dependence is strongest below the branch-12 LO-phonon energy: relaxation times are substantially longer at lower temperatures and rise more rapidly with electron energy. Above the LO-phonon threshold, the temperature dependence remains visible but is much weaker. These observations indicate that branch-12 LO-phonon emission dominates momentum relaxation above the threshold. For this process, the factor entering the inverse relaxation time is $n_\mathbf{q}^{12}(100\,\mathrm{K})+1 \approx n_\mathbf{q}^{12}(300\,\mathrm{K})+1 \approx n_\mathbf{q}^{12}(500\,\mathrm{K})+1 \approx 1$.

To investigate the low-energy behaviour more closely, the relaxation time at $T = 300\,\mathrm{K}$ was recalculated near Γ including only scattering by the six highest-energy phonon branches (Figure 5.6).

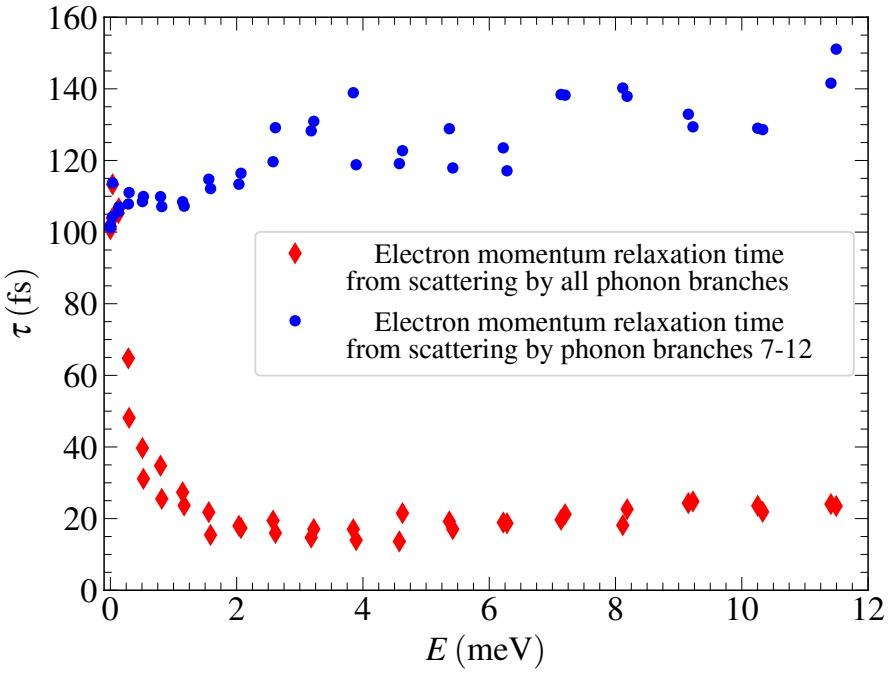

Figure 5.6: Calculated electron momentum relaxation time versus energy relative to the conduction-band minimum at $T = 300\,\mathrm{K}$, including scattering by only the six highest-energy phonon branches (blue circles) or by all phonon branches (red diamonds). The electrons belong to the lowest conduction-band pair and have crystal momenta along $\Gamma - \mathrm{A}$.

The results indicate that, below approximately 1 meV, momentum relaxation is dominated by absorption of optical phonons from the six highest-energy branches. Above this threshold, scattering by the six lower-energy branches rapidly becomes dominant. A numerical origin for the behaviour within the first few meV cannot be ruled out completely. Theoretical models predict that, for deformation-potential scattering by longitudinal acoustic phonons, the squared coupling behaves as $\propto q$ as $q \to 0$. Polar semiconductors also exhibit piezoelectric scattering by acoustic phonons, for which the squared coupling diverges as $\propto 1/q$ near $\mathbf{q} = \mathbf{0}$ [47]. It is therefore not straightforward to predict which mechanism dominates acoustic-phonon momentum relaxation. The code used here can resolve the individual contributions of these mechanisms [40]. For the mobility calculation, however, relaxation of extremely low-energy electrons contributes negligibly because their group velocities are very small. For electron energies above a few meV but below the branch-12 LO-phonon energy, Fig. 5.6 indicates that acoustic-phonon scattering is the dominant mechanism. The occupation of branch-12 phonons remains extremely small even at 500 K, whereas acoustic-phonon occupations are appreciable at all three temperatures. Relaxation times in this energy range consequently depend strongly on temperature, just as the acoustic-phonon occupations do.

Figure 5.7 shows the hole momentum relaxation time at $T = 300\,\mathrm{K}$ as a function of hole energy relative to the maximum of the uppermost valence band at Γ. The holes belong to the three uppermost valence-band pairs near Γ, with crystal momenta along $\Gamma - \mathrm{K}$, $\Gamma - \mathrm{M}$, or $\Gamma - \mathrm{A}$.

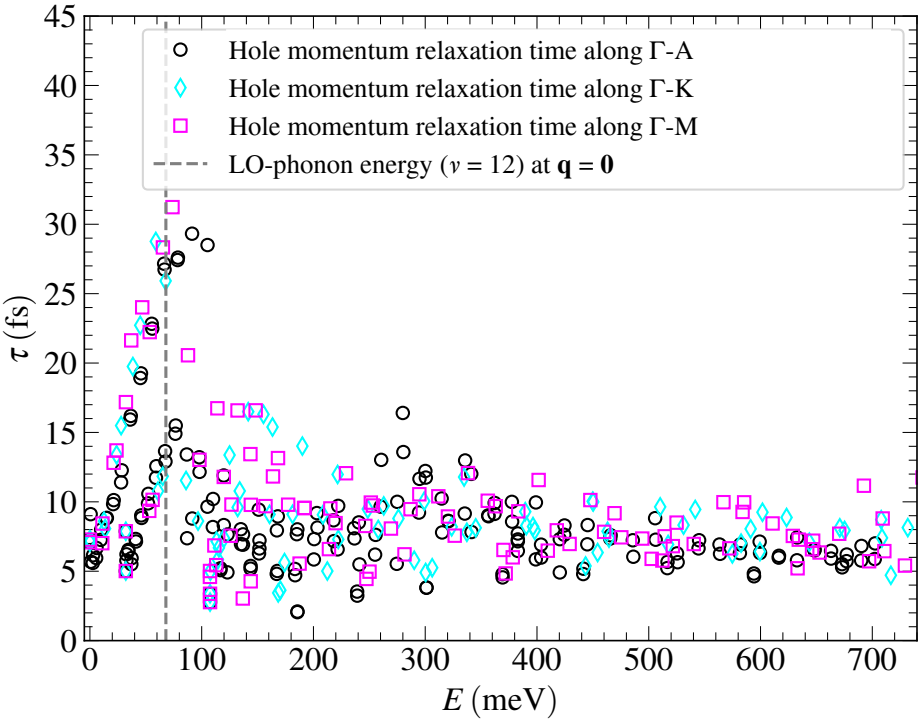

Figure 5.7: Calculated hole momentum relaxation time versus energy relative to the maximum of the uppermost valence band at $T = 300\,\mathrm{K}$. The holes belong to the three uppermost valence-band pairs, with crystal momenta along $\Gamma - \mathrm{A}$ (black circles), $\Gamma - \mathrm{K}$ (turquoise diamonds), or $\Gamma - \mathrm{M}$ (pink squares). The dashed vertical line marks the energy of the branch-12 LO phonon at $\mathbf{q} = \mathbf{0}$.

Below the branch-12 LO-phonon energy, two groups of states exhibit relaxation times that rise with hole energy. They originate from the two uppermost valence-band pairs. For holes moving along $\Gamma - \mathrm{A}$, parallel to $\mathbf{c}$, the relaxation time does not fall sharply on crossing the LO-phonon energy, whereas such a drop is observed for momenta normal to $\mathbf{c}$.

Figures 5.8 and 5.9 show the corresponding temperature dependence along $\Gamma - \mathrm{A}$ and along $\Gamma - \mathrm{M}$ or $\Gamma - \mathrm{K}$, respectively, at $T = 100\,\mathrm{K}$, $300\,\mathrm{K}$, and $500\,\mathrm{K}$.

The temperature dependence of the hole momentum relaxation times is similar to that found for electrons.

Comparison of Figs. 5.8 and 5.9 shows that the lighter in-plane holes undergo a sharp decrease in relaxation time above the LO-phonon energy, whereas the heavier holes moving parallel to $\mathbf{c}$ do not. The effect is clear at all three temperatures.

The influence of hole mass can be understood from the kinematics of scattering by small-wave-vector branch-12 LO phonons, for which the coupling is strongest. Emission of a phonon of energy $\omega_{\mathbf{q}}^{12}$ by a hole requires $\epsilon(\mathbf{k}) - \epsilon(\mathbf{k} - \mathbf{q}) = \omega_{\mathbf{q}}^{12}$. Linearisation gives $\nabla_{\mathbf{k}}\epsilon \cdot \mathbf{q} = \omega_{\mathbf{q}}^{12}$, or $\mathbf{v}(\mathbf{k}) \cdot \mathbf{q} = \omega_{\mathbf{q}}^{12}$. Within the effective-mass approximation, $\mathbf{v} = m^{-1}\mathbf{k}$; for a parabolic band and momentum parallel to direction i, the kinematic condition becomes $m_{ii}^{-1} k_i q = \omega_{\mathbf{q}}^{12}$. A heavier hole must therefore have a larger momentum, and hence greater kinetic energy, to emit an LO phonon with $\mathbf{q} \approx \mathbf{0}$. In the calculations, this condition is met when the hole energy is approximately 50% greater than the branch-12 LO-phonon energy.

A rough numerical estimate illustrates the effect. Suppose branch-12 LO-phonon emis-

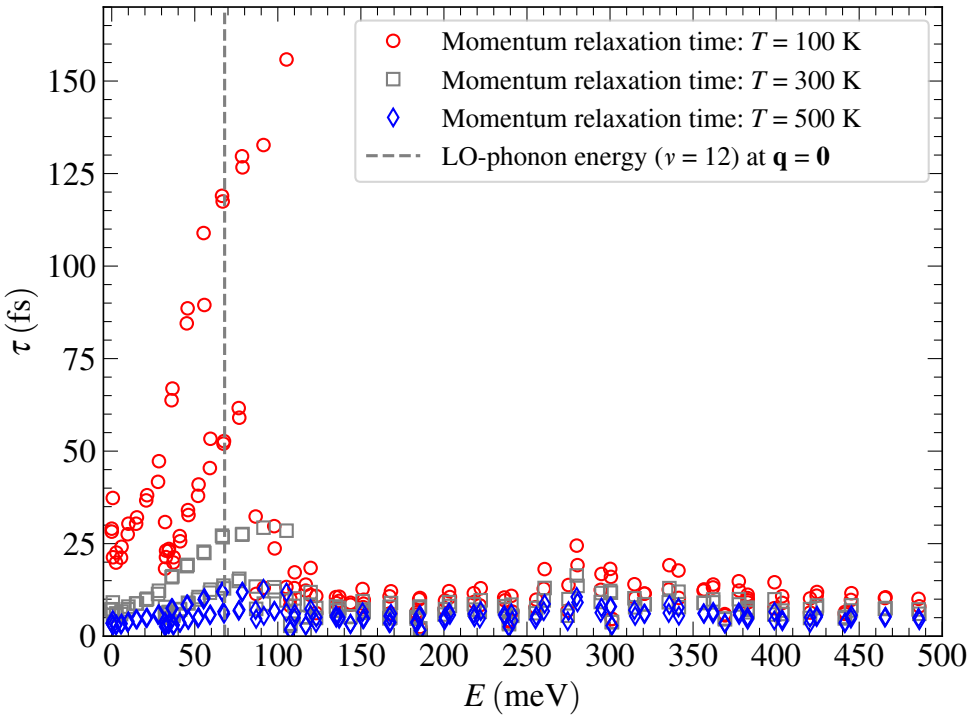

Figure 5.8: Calculated hole momentum relaxation time versus energy relative to the uppermost valence-band maximum at $T = 100\,\mathrm{K}$ (red circles), 300 K (grey squares), and 500 K (blue diamonds). The holes belong to the three uppermost valence-band pairs and have crystal momenta along $\Gamma - \mathrm{A}$. The dashed vertical line marks the energy of the branch-12 LO phonon at $\mathbf{q} = \mathbf{0}$.

sion becomes dominant for hole energies $\epsilon(\mathbf{k}_1) \approx 110\,\mathrm{meV} \approx 4\,\mathrm{mHa}$ and above, and approximate the uppermost valence-band dispersion along $\Gamma - \mathrm{A}$ as quadratic. With $m^* \approx 2.4 m_0$, the initial hole momentum is $k_1 = \sqrt{2m^*E} \approx 0.14 a_0^{-1}$. The final hole energy after emission is $\epsilon(\mathbf{k}_2) = \epsilon(\mathbf{k}_1) - \omega^{12}(\mathbf{q}) = 1.43\,\mathrm{mHa}$, corresponding to $k_2 \approx 0.083 a_0^{-1}$. The kinematic condition therefore requires $q > 0.057 a_0^{-1}$. At this limiting value, the direction of momentum and velocity is unchanged, so the momentum has not yet been relaxed; an actual change of velocity direction requires a still larger q. The estimated minimum wave-vector magnitude is approximately 15% of the Γ–A distance. At wave vectors of this order, the branch-12 hole-phonon coupling may become sufficiently strong for LO-phonon emission to dominate hole momentum relaxation.

Applying the same analysis along $\Gamma - \mathrm{K}$ or $\Gamma - \mathrm{M}$ gives a minimum emitted-phonon wave vector of $q = 0.039 a_0^{-1}$ for a hole whose energy is approximately equal to the branch-12 LO-phonon energy. This is about 7% of the Γ–K distance. At this smaller wave vector, the corresponding hole-phonon coupling is expected to be sufficiently large for LO-phonon emission to become the dominant momentum-relaxation mechanism.

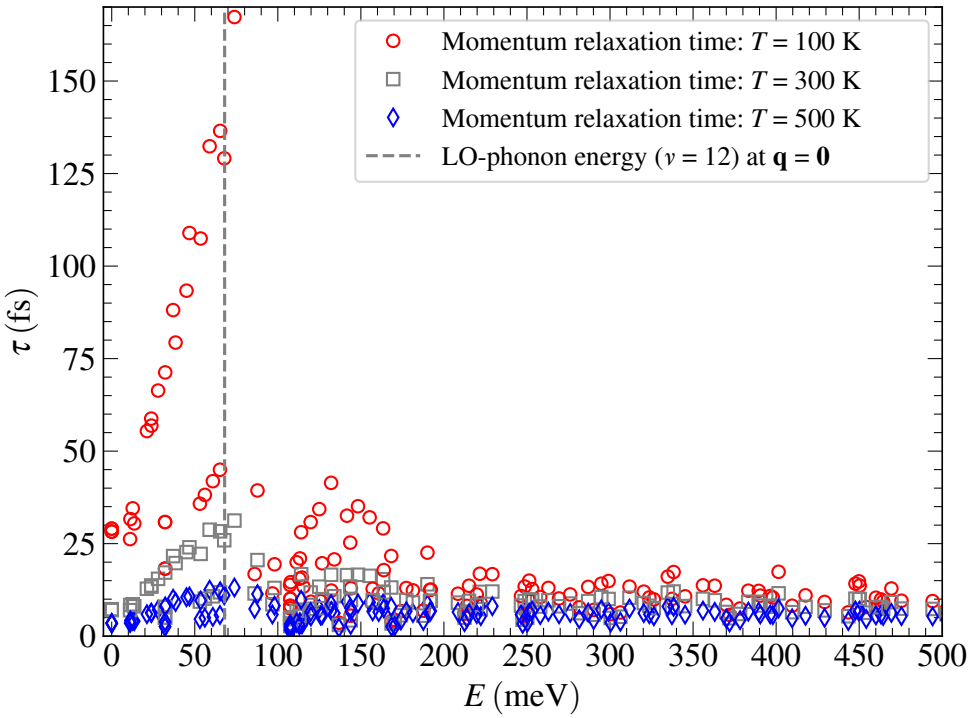

Figure 5.9: Calculated hole momentum relaxation time versus energy relative to the uppermost valence-band maximum at $T = 100\,\mathrm{K}$ (red circles), 300 K (grey squares), and 500 K (blue diamonds). The holes belong to the three uppermost valence-band pairs and have crystal momenta along $\Gamma - \mathrm{K}$ or $\Gamma - \mathrm{M}$. The dashed vertical line marks the energy of the branch-12 LO phonon at $\mathbf{q} = \mathbf{0}$.

5.4 Mobility

The mobility tensors were calculated using the method of Ref. [4], based on random *Monte Carlo* sampling of charge carriers and of the phonon-wave-vector directions involved in their scattering. For each carrier type, $N_k = 100$ states and $N_\Omega = 100$ phonon-wave-vector directions were sampled, with carrier sampling optimised for $T_{ref} = 500\,\mathrm{K}$. The calculation was repeated ten times with different random-number seeds. The reported mobility-tensor components are the means of these ten calculations, with their standard deviations also shown. The standard error of the mean electron mobility is sufficiently small for the calculations to be regarded as converged.

Figure 5.10 shows the calculated temperature dependence of the mobility of electrons in the lowest conduction-band pair along the coordinate axes on a logarithmic scale. Experimental results for bulk [48] and thin-film [49] single-crystalline ZnO are included.

The two in-plane mobilities are identical, as expected from the in-plane isotropy of the electron dispersion and high-frequency relative dielectric tensor. The mobility along $\mathbf{c}$ is nearly the same; when the standard error is taken into account, the conduction-electron mobility can be considered isotropic in three dimensions.

As expected, the mobility decreases with increasing temperature as phonon occupations rise. The theoretical mobility is expected to be overestimated because the conduction-electron effective mass is underestimated and the high-frequency relative permittivity is overestimated. Comparison with the bulk-ZnO measurement [48] confirms this expectation. Interestingly, the measured thin-film mobility [49] exceeds the

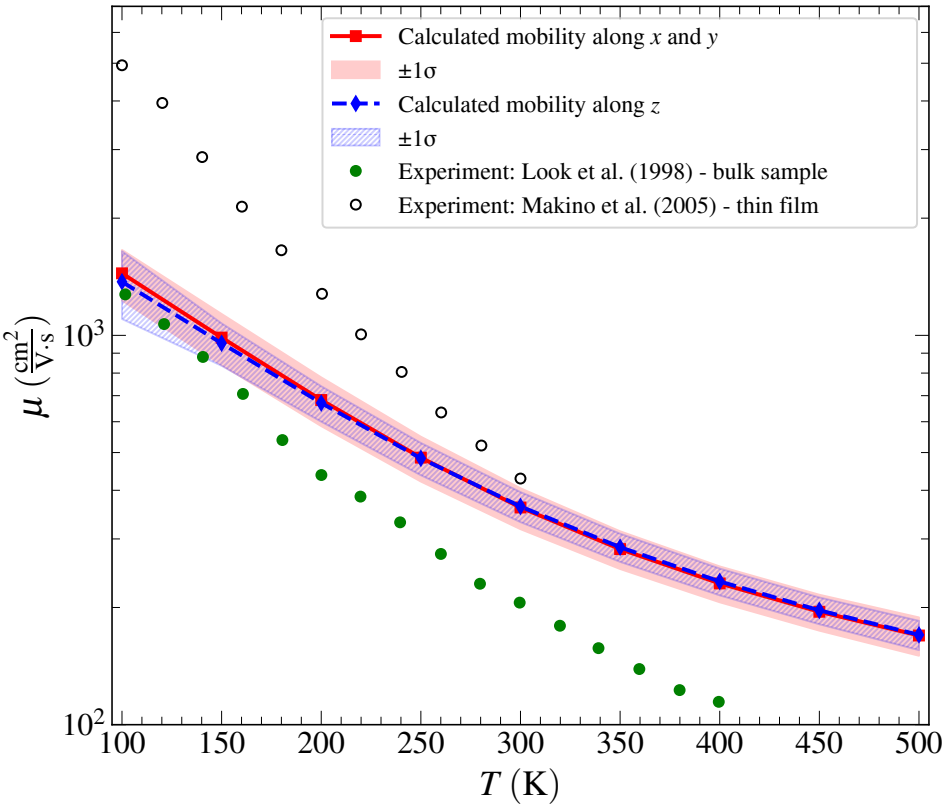

Figure 5.10: Calculated temperature dependence of the mobility of electrons in the lowest conduction-band pair along the coordinate axes, together with experimental values for bulk wurtzite ZnO [48] and a ZnO thin film [49].

value calculated here. Figure 5.10 also shows that the experimental mobilities decrease more rapidly with temperature than the theoretical prediction. Further investigation is required to understand these differences.

The electron mobilities obtained for wurtzite ZnO are approximately one order of magnitude lower than the calculated mobilities of ZnSe, ZnTe, CdSe, and CdTe [3]. Those semiconductors have substantially longer electron momentum relaxation times, higher high-frequency relative permittivities, and smaller conduction-electron effective masses than ZnO.

Figure 5.11 shows the calculated temperature dependence of hole mobility in the three uppermost valence-band pairs along the coordinate axes.

Although the calculated hole mobility is isotropic in the plane normal to **c**, it is not isotropic in three dimensions. The in-plane mobility is significantly greater than the mobility along **c**, consistent with the much smaller in-plane hole effective masses. The theoretical results were not compared with experiment because reliable p-type ZnO is exceptionally difficult to achieve. Whereas n-type conductivity occurs naturally in ZnO containing impurities and defects, stable and reproducible p-type ZnO has not yet been established. Although several studies report p-type samples [50][51][52][53], their hole mobilities vary widely and appear to depend strongly on the individual sample. There is consequently no reliable experimental reference against which the calculated ZnO hole mobility can be compared meaningfully.

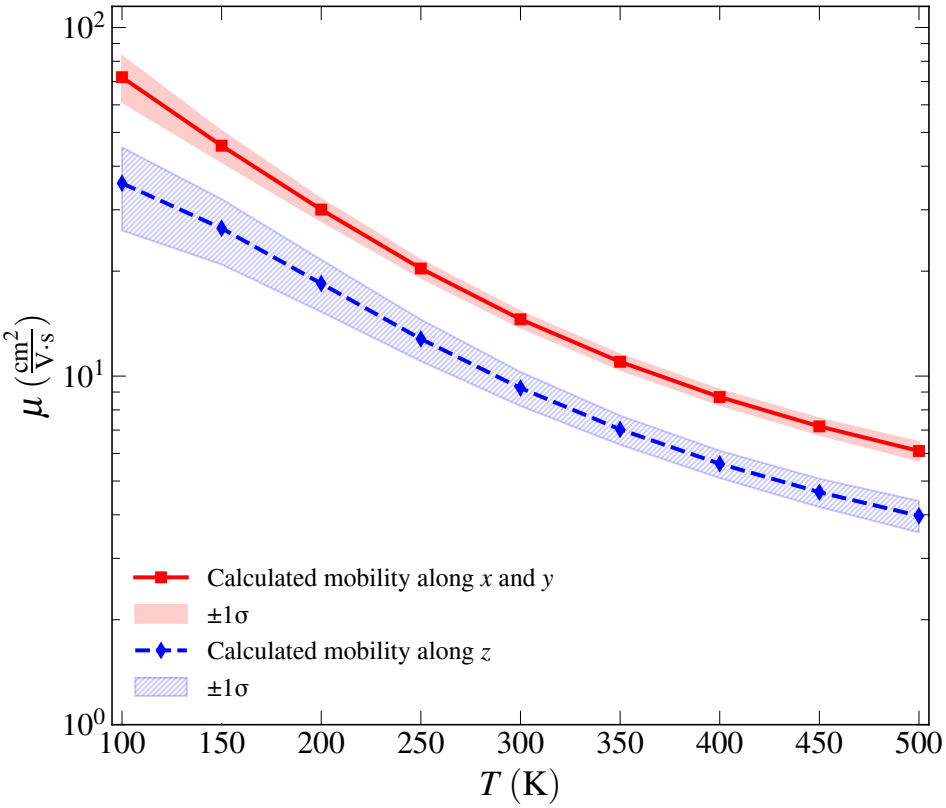

Figure 5.11: Calculated temperature dependence of the mobility of holes in the three uppermost valence-band pairs along the coordinate axes.

6 Conclusion

This work used *ab initio* calculations of the electronic structure, phonon dispersions, and electron-phonon coupling matrix elements to investigate quantitatively the temperature dependence of charge-carrier mobility in wurtzite ZnO. Momentum relaxation times as functions of carrier energy at different temperatures were analysed to identify the dominant relaxation mechanisms that directly limit mobility.

Despite major methodological and software advances during the past two decades, *ab initio* carrier-transport calculations in polar semiconductors remain computationally intensive. The grid-free method of Ref. [4] substantially reduces the cost by evaluating *Wannier-Fourier*-interpolated coupling matrix elements only at selected k- and q-points rather than throughout predetermined dense grids. Previously demonstrated for cubic ZnTe, the method was applied here to anisotropic wurtzite ZnO.

The PBE electronic structure underestimates the ZnO band gap by a factor of approximately four and the conduction-electron effective mass by more than 40%, which should lead to overestimated electron mobilities (Table 5.2). By contrast, the calculated phonon dispersions agree reasonably well with experiment, with deviations below 15% (Figure 5.1).

The coupling matrix elements indicate that scattering by small-wave-vector LO phonons in the highest-energy branch is the dominant channel. The energy-dependent momentum relaxation times follow the trend reported for ZnSe, ZnTe, CdSe, and CdTe [3], but the ZnO values are approximately 50% shorter. The *Fröhlich* interaction limits

mobility once LO-phonon emission is kinematically allowed. LO-phonon absorption dominates at extremely low carrier energies, whereas acoustic-phonon scattering dominates between a few meV and the emission threshold.

The calculated electron mobilities are approximately an order of magnitude lower than theoretical values for ZnSe, ZnTe, CdSe, and CdTe [3][4]. The underestimated electron effective mass and overestimated high-frequency relative permittivity should cause the ZnO mobility to exceed experiment; nevertheless, measurements on a thin single-crystalline n-type ZnO film yielded still higher mobilities (Figure 5.10).

The calculated hole mobilities are substantially lower than the electron mobilities, consistent with the much larger hole effective masses.

Using the method of Ref. [4], well-converged relaxation-time and mobility calculations for wurtzite ZnO can be completed in approximately one week on 64 Intel Xeon E5-2670 CPU cores. The required inputs are an electronic structure including SOC and phonon data obtained on coarse $6 \times 6 \times 4$ k- and q-point grids.

Future calculations could use electronic structures obtained with HSE06 or the GW approximation, which generally yield more accurate effective masses, band gaps, and high-frequency relative permittivities [54]. Because an efficient method for evaluating electron-phonon coupling directly from such band structures is not yet available, coupling matrix elements obtained as in this work are usually rescaled. Comparing the resulting mobilities with those reported here would clarify the influence of the exchange-correlation approximation.

References

[1] F. Giustino, M. L. Cohen, and S. G. Louie. *Phys. Rev. B*, 76:165108, (2007). 10.1103/PhysRevB.76.165108.

[2] C. Verdi and F. Giustino. *Phys. Rev. Lett.*, 115:176401, (2015). 10.1103/PhysRevLett.115.176401.

[3] N. Vukmirović. *Phys. Rev. B*, 104:085203, (2021). 10.1103/PhysRevB.104.085203.

[4] N. Vukmirović. *Comput. Phys. Commun.*, 312:109583, (2025). 10.1016/j.cpc.2025.109583.

[5] M. C. Payne, M. P. Teter, D. C. Allan, T. A. Arias, and J. D. Joannopoulos. *Rev. Mod. Phys.*, 64:1045–1097, (1992). 10.1103/RevModPhys.64.1045.

[6] S. Baroni, S. de Gironcoli, A. Dal Corso, and P. Giannozzi. *Rev. Mod. Phys.*, 73:515–562, (2001). 10.1103/RevModPhys.73.515.

[7] N. W. Ashcroft and N. D. Mermin. *Solid State Physics*. Saunders College, (1976).

[8] R. M. Martin. *Electronic Structure: Basic Theory and Practical Methods*. Cambridge University Press, (2004).

[9] P. Hohenberg and W. Kohn. *Phys. Rev.*, 136:B864–B871, (1964). 10.1103/PhysRev.136.B864.

[10] W. Kohn and L. J. Sham. *Phys. Rev.*, 140:A1133–A1138, (1965). 10.1103/PhysRev.140.A1133.

[11] J. F. Janak. *Phys. Rev. B*, 18:7165–7168, (1978). 10.1103/PhysRevB.18.7165.

[12] J. P. Perdew, R. G. Parr, M. Levy, and J. L. Balduz. *Phys. Rev. Lett.*, 49:1691–1694, (1982). 10.1103/PhysRevLett.49.1691.

[13] F. Giustino. *Materials Modelling using Density Functional Theory*. Oxford University Press, (2014).

[14] D. M. Ceperley and B. J. Alder. *Phys. Rev. Lett.*, 45:566–569, (1980). 10.1103/PhysRevLett.45.566.

[15] J. P. Perdew and A. Zunger. *Phys. Rev. B*, 23:5048–5079, (1981). 10.1103/PhysRevB.23.5048.

[16] J. P. Perdew, K. Burke, and M. Ernzerhof. *Phys. Rev. Lett.*, 77:3865–3868, (1996). 10.1103/PhysRevLett.77.3865.

[17] H. J. Monkhorst and J. D. Pack. *Phys. Rev. B*, 13(12):5188–5192, (1976). 10.1103/PhysRevB.13.5188.

[18] A. Marrazzo et al. *Rev. Mod. Phys.*, 96:045008, (2024). 10.1103/RevModPhys.96.045008.

[19] N. Marzari and D. Vanderbilt. *Phys. Rev. B*, 56:12847–12865, (1997). 10.1103/PhysRevB.56.12847.

[20] M. S. Dresselhaus, G. Dresselhaus, and A. Jorio. *Group Theory: Application to the Physics of Condensed Matter*. Springer Berlin Heidelberg, Berlin, Heidelberg, 1st edition, (2008). 10.1007/978-3-540-32899-8.

[21] C. Jacoboni. *Theory of Electron Transport in Semiconductors: A Pathway from Elementary Physics to Nonequilibrium Green Functions*. Springer, (2010).

[22] H. Fröhlich. *Adv. Phys.*, 3(11):325–361, (1954). 10.1080/00018735400101213.

[23] J.-J. Zhou and M. Bernardi. *Phys. Rev. B*, 94:201201, (2016). 10.1103/PhysRevB.94.201201.

[24] T.-H. Liu, J. Zhou, B. Liao, D. J. Singh, and G. Chen. *Phys. Rev. B*, 95:075206, (2017). 10.1103/PhysRevB.95.075206.

[25] G. Brunin et al. *Phys. Rev. B*, 102:094308, (2020). 10.1103/PhysRevB.102.094308.

[26] A. S. Chaves, A. Antonelli, D. T. Larson, and E. Kaxiras. *Phys. Rev. B*, 102:125116, (2020). 10.1103/PhysRevB.102.125116.

[27] S. Poncé et al. *Phys. Rev. Res.*, 3:043022, (2021). 10.1103/PhysRevResearch.3.043022.

[28] O. Madelung. *Semiconductors: Data Handbook*. Springer, Berlin, Heidelberg, 3rd edition, (2004). 10.1007/978-3-540-30488-3.

[29] X. Gonze et al. *Comput. Phys. Commun.*, 180(12):2582–2615, (2009). 10.1016/j.cpc.2009.07.007.

[30] X. Gonze et al. *Comput. Phys. Commun.*, 205:106–131, (2016). 10.1016/j.cpc.2016.04.003.

[31] M. J. van Setten et al. *Comput. Phys. Commun.*, 226:39–54, (2018). 10.1016/j.cpc.2018.01.012.

[32] A. Jain et al. *APL Mater.*, 1(1):011002, (2013). 10.1063/1.4812323.

[33] Y. Hinuma, G. Pizzi, Y. Kumagai, F. Oba, and I. Tanaka. *Computational Materials Science*, 128:140–184, (2017). 10.1016/j.commatsci.2016.10.015.

[34] A. Togo, K. Shinohara, and I. Tanaka. `Spglib`: a software library for crystal symmetry search, (2024).

[35] A. A. Mostofi et al. *Comput. Phys. Commun.*, 185(8):2309–2310, (2014). 10.1016/j.cpc.2014.05.003.

[36] I. Souza, N. Marzari, and D. Vanderbilt. *Phys. Rev. B*, 65:035109, (2001). 10.1103/PhysRevB.65.035109.

[37] X. Gonze. *Phys. Rev. B*, 55(16):10337–10354, (1997). 10.1103/physrevb.55.10337.

[38] X. Gonze and C. Lee. *Phys. Rev. B*, 55(16):10355–10368, (1997). 10.1103/physrevb.55.10355.

[39] P. Ghosez, J.-P. Michenaud, and X. Gonze. *Phys. Rev. B*, 58(10):6224–6240, (1998). 10.1103/physrevb.58.6224.

[40] N. Vukmirović. Grid-free evaluation of phonon-limited relaxation times and electrical transport properties, (2025). Version 2. 10.5281/zenodo.15036095.

[41] C. Verdi and F. Giustino. *Phys. Rev. Lett.*, 115:176401, (2015). 10.1103/PhysRevLett.115.176401.

[42] J. Sjakste, N. Vast, M. Calandra, and F. Mauri. *Phys. Rev. B*, 92:054307, (2015). 10.1103/PhysRevB.92.054307.

[43] K. Hummer, J. Harl, and G. Kresse. *Phys. Rev. B*, 80:115205, (2009). 10.1103/PhysRevB.80.115205.

[44] A. V. Krukau, O. A. Vydrov, A. F. Izmaylov, and G. E. Scuseria. *J. Chem. Phys.*, 125(22):224106, (2006). 10.1063/1.2404663.

[45] J. Serrano et al. *Phys. Rev. B*, 81:174304, (2010). 10.1103/PhysRevB.81.174304.

[46] J. Serrano et al. *Phys. Status Solidi B*, 235:260, (2003). 10.1002/pssb.200301566.

[47] P. Y. Yu and M. Cardona. *Fundamentals of Semiconductors: Physics and Materials Properties*. Springer, Berlin, Heidelberg, 4th edition, (2010). 10.1007/978-3-642-00710-1.

[48] D. Look et al. *Solid State Commun.*, 105:399–401, (1998). 10.1016/S0038-1098(97)10145-4.

[49] T. Makino, Y. Segawa, A. Tsukazaki, A. Ohtomo, and M. Kawasaki. *Appl. Phys. Lett.*, 87:022101, (2005). 10.1063/1.1991994.

[50] D. C. Look, B. Claflin, S. B. Park, and S. J. Lee. *J. Mater. Sci.*, 41:8054–8057, (2006). 10.1007/s10853-005-2279-y.

[51] H. Liu et al. *J. Semicond.*, 31(4):043001, (2010). 10.1088/1674-4926/31/4/043001.

[52] H. Zhang et al. *Appl. Phys. A*, 105(1):147–151, (2011). 10.1007/s00339-011-6390-4.

[53] C. Pan et al. *J. Am. Chem. Soc.*, 132(22):7269–7271, (2010). 10.1021/ja908521s.

[54] I.-H. Chu et al. *Phys. Rev. B*, 93(12), (2016). 10.1103/physrevb.93.125210.

A Convergence Tests

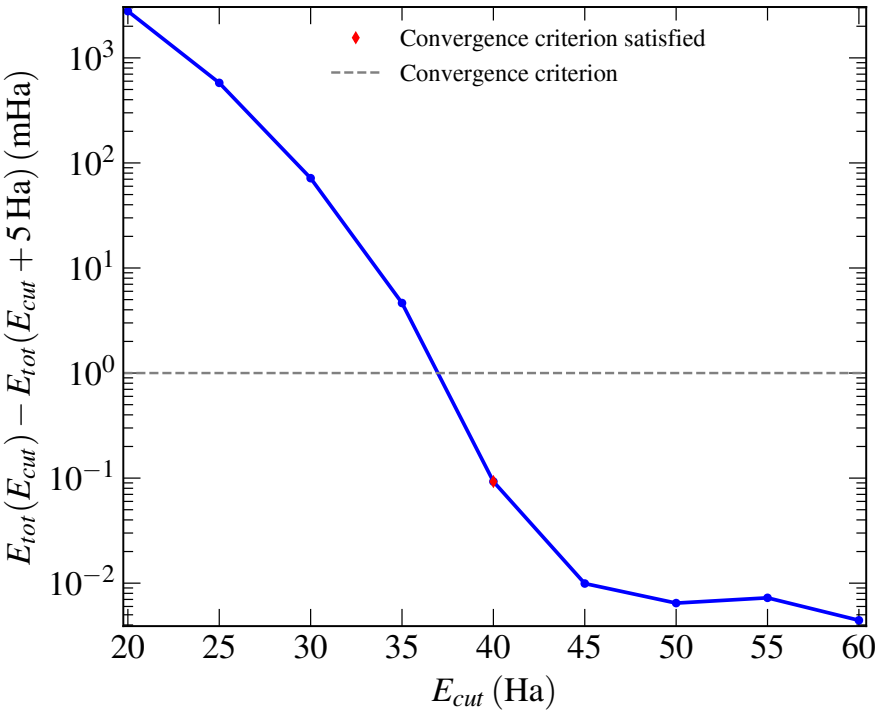

Figure A.1: Convergence test of the DFT calculation with respect to the maximum plane-wave kinetic energy (E_{cut}). The plotted quantity is the difference between the ground-state total energies obtained in two calculations whose maximum plane-wave energies differ by 5 Ha, $E_{tot}(E_{cut}) - E_{tot}(E_{cut} + 5\,\mathrm{Ha})$, as a function of the lower of the two cutoff energies (E_{cut}). The convergence criterion was considered satisfied when this difference was below 1 mHa; the corresponding cutoff energy was 45 Ha. A $6 \times 6 \times 4$ *Monkhorst–Pack* k-point grid was used.

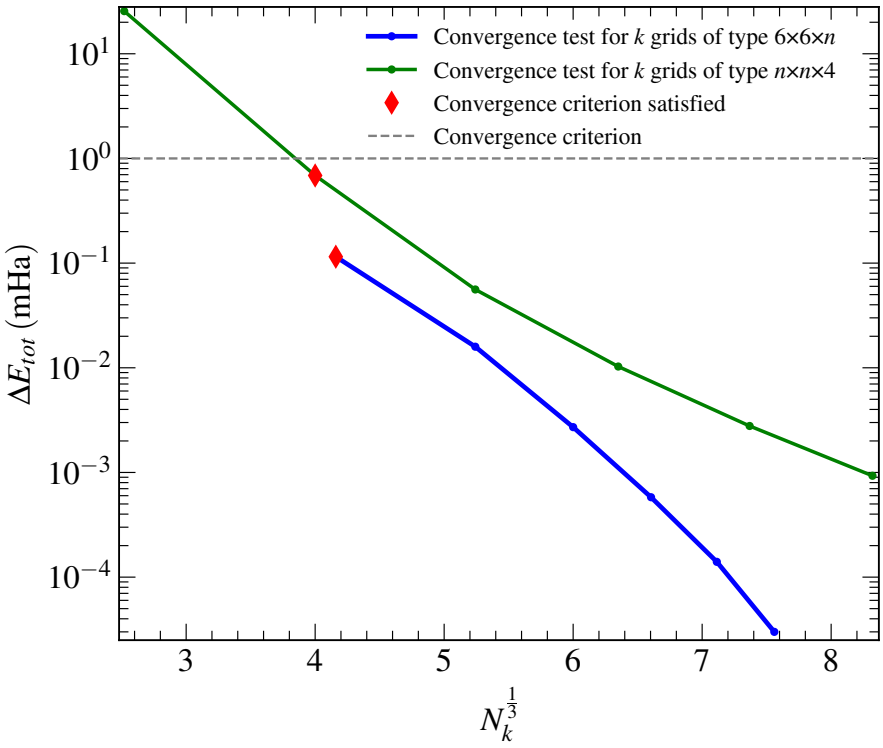

Figure A.2: Convergence test of the DFT calculation with respect to the k-point grid. The plotted quantity is the difference between the ground-state total energies obtained with two grids of different linear density, shown as a function of the denser grid. The convergence criterion was considered satisfied when this energy difference was below 1 mHa; it was met by the $6 \times 6 \times 4$ *Monkhorst–Pack* grid. A plane-wave cutoff of $E_{cut} = 45$ Ha was used. The tested grids were of the form $n \times n \times 4$ ($2 \times 2 \times 4$, $4 \times 4 \times 4$, $6 \times 6 \times 4$, …, $14 \times 14 \times 4$) and $6 \times 6 \times n$ ($6 \times 6 \times 2$, $6 \times 6 \times 4$, …, $6 \times 6 \times 14$).

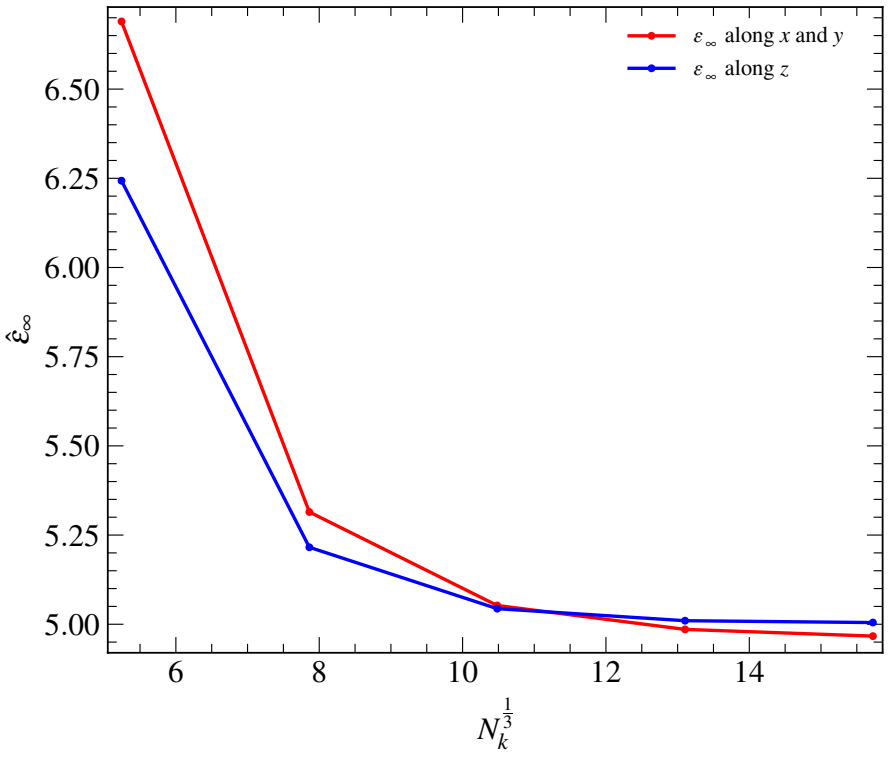

Figure A.3: Convergence test of the high-frequency relative dielectric tensor ($\hat{\varepsilon}_\infty$) with respect to the linear density of the k-point grid used in the DFT calculation. The diagonal tensor components are plotted against the linear k-point density $N_k^{1/3}$. Convergence was taken to be reached at the rightmost point, corresponding to an $18 \times 18 \times 12$ *Monkhorst–Pack* grid. A plane-wave cutoff of $E_{cut} = 45\,\text{Ha}$ was used. The tested grids were $6 \times 6 \times 4$, $9 \times 9 \times 6$, $12 \times 12 \times 8$, $15 \times 15 \times 10$, and $18 \times 18 \times 12$.

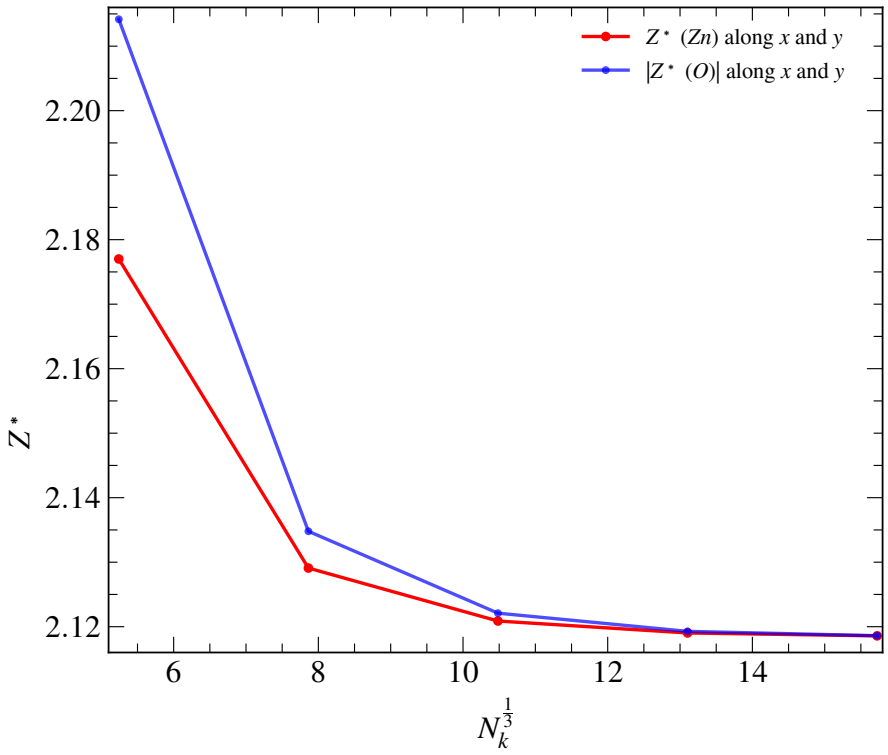

Figure A.4: Convergence test of the Born effective-charge tensors Z^* of the O^{2-} and Zn^{2+} ions in the plane normal to the **c** direction, with respect to the linear density of the k-point grid used in the DFT calculation. The relevant diagonal tensor components are plotted against $N_k^{1/3}$. Convergence was taken to be reached at the rightmost point, corresponding to an $18 \times 18 \times 12$ *Monkhorst–Pack* grid. A plane-wave cutoff of $E_{cut} = 45\,\text{Ha}$ was used. The tested grids were $6 \times 6 \times 4$, $9 \times 9 \times 6$, $12 \times 12 \times 8$, $15 \times 15 \times 10$, and $18 \times 18 \times 12$.

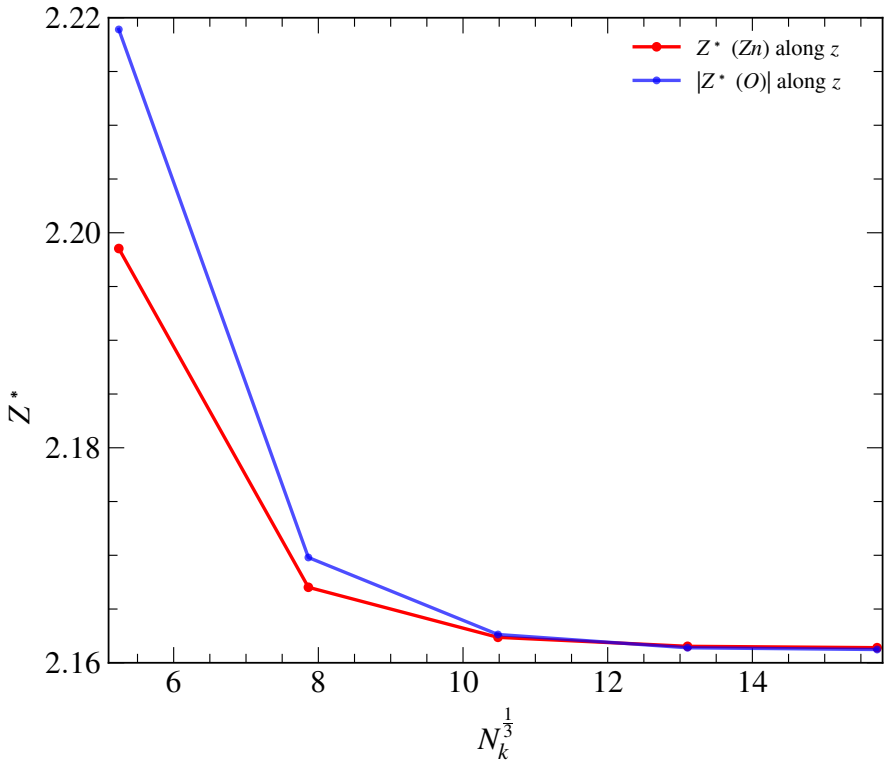

Figure A.5: Convergence test of the Born effective-charge tensors Z^* of the O^{2-} and Zn^{2+} ions along the **c** direction, with respect to the linear density of the k-point grid used in the DFT calculation. The relevant diagonal tensor components are plotted against $N_k^{1/3}$. Convergence was taken to be reached at the rightmost point, corresponding to an $18 \times 18 \times 12$ *Monkhorst–Pack* grid. A plane-wave cutoff of $E_{cut} = 45\,\text{Ha}$ was used. The tested grids were $6 \times 6 \times 4$, $9 \times 9 \times 6$, $12 \times 12 \times 8$, $15 \times 15 \times 10$, and $18 \times 18 \times 12$.

Table A.1: Phonon frequencies (in meV) at the high-symmetry q-points M, A, and Γ for different values of E_{cut} (40 Ha, 45 Ha, and 50 Ha), using a $6 \times 6 \times 4$ *Monkhorst–Pack* k-point grid.

M			A			Γ		
40	45	50	40	45	50	40	45	50
10.1695	10.0699	10.0718	8.3999	8.2838	8.2865	1.3033	-0.3519	-0.2664
14.8344	14.8251	14.7693	8.3999	8.2838	8.2865	1.3033	-0.3519	-0.2664
15.7632	15.6948	15.6954	8.4000	8.2838	8.2865	2.4934	2.4632	1.1954
19.8292	19.8158	19.8034	8.4000	8.2838	8.2865	11.0382	10.9467	10.9484
28.5453	28.5093	28.5011	22.4623	22.4577	22.4047	11.0382	10.9467	10.9484
31.3516	31.3236	31.3244	22.4624	22.4577	22.4047	31.0278	31.0268	31.0362
52.6626	52.6601	52.4242	50.7618	50.7629	50.7630	45.1114	45.1179	44.8659
53.2449	53.2455	53.2455	50.7618	50.7629	50.7630	48.7985	48.8017	48.8017
58.4708	58.4672	58.4672	50.7618	50.7629	50.7630	48.7985	48.8017	48.8017
59.4605	59.4518	59.2274	50.7618	50.7629	50.7630	52.6765	52.6764	52.6764
65.3237	65.3159	65.3134	66.3850	66.3807	66.1943	52.6765	52.6764	52.6764
66.5013	66.4919	66.4910	66.3851	66.3807	66.1943	65.6603	65.6476	65.4362

Table A.2: Phonon frequencies (in meV) at the high-symmetry q-points M, A, and Γ for different *Monkhorst–Pack* k-point grids ($4\times4\times4$, $6\times6\times4$, and $8\times8\times4$), at fixed $E_{cut} = 45\,\mathrm{Ha}$.

M			A			Γ		
$4\times4\times4$	$6\times6\times4$	$8\times8\times4$	$4\times4\times4$	$6\times6\times4$	$8\times8\times4$	$4\times4\times4$	$6\times6\times4$	$8\times8\times4$
10.0209	10.0699	10.0749	8.2944	8.2838	8.2837	-0.3468	-0.3519	-0.3525
14.8064	14.8251	14.8257	8.2944	8.2838	8.2837	-0.3468	-0.3519	-0.3525
15.6653	15.6948	15.7017	8.2944	8.2838	8.2837	2.4634	2.4632	2.4632
19.8096	19.8158	19.8166	8.2944	8.2838	8.2837	10.9516	10.9467	10.9485
28.5123	28.5093	28.5082	22.4471	22.4577	22.4551	10.9516	10.9467	10.9485
31.3226	31.3236	31.3235	22.4472	22.4577	22.4552	31.0269	31.0268	31.0218
52.5277	52.6601	52.6646	50.6999	50.7629	50.7750	45.0763	45.1179	45.1264
53.1510	53.2455	53.2505	50.6999	50.7629	50.7750	48.6802	48.8017	48.8284
58.4116	58.4672	58.4687	50.6999	50.7629	50.7750	48.6802	48.8017	48.8284
59.3012	59.4518	59.4547	50.6999	50.7629	50.7750	52.6286	52.6764	52.6853
65.4603	65.3159	65.2858	66.3386	66.3807	66.3369	52.6286	52.6764	52.6853
66.6486	66.4919	66.4656	66.3386	66.3807	66.3370	65.6497	65.6476	65.6292

Table A.3: Phonon frequencies (in meV) at the high-symmetry q-points M, A, and Γ for different *Monkhorst–Pack* k-point grids ($6\times6\times2$, $6\times6\times4$, and $6\times6\times6$), at fixed $E_{cut} = 45\,\mathrm{Ha}$.

M			A			Γ		
$6\times6\times2$	$6\times6\times4$	$6\times6\times6$	$6\times6\times2$	$6\times6\times4$	$6\times6\times6$	$6\times6\times2$	$6\times6\times4$	$6\times6\times6$
8.3751	10.0699	10.0701	8.3751	8.2838	8.2816	-0.3546	-0.3519	-0.3517
8.3751	14.8251	14.8267	8.3751	8.2838	8.2816	-0.3546	-0.3519	-0.3517
8.3751	15.6948	15.6929	8.3751	8.2838	8.2816	2.4630	2.4632	2.4633
8.3751	19.8158	19.8193	8.3751	8.2838	8.2816	10.9580	10.9467	10.9436
22.4202	28.5093	28.5074	22.4202	22.4577	22.4579	10.9580	10.9467	10.9436
22.4203	31.3236	31.3224	22.4203	22.4577	22.4580	31.0431	31.0268	31.0270
50.7896	52.6601	52.6611	50.7896	50.7629	50.7646	45.0363	45.1179	45.1333
50.7896	53.2455	53.2436	50.7896	50.7629	50.7646	48.8201	48.8017	48.8101
50.7896	58.4672	58.4637	50.7896	50.7629	50.7646	48.8201	48.8017	48.8101
50.7896	59.4518	59.4458	50.7896	50.7629	50.7646	52.6966	52.6764	52.6744
66.4676	65.3159	65.3019	66.4676	66.3807	66.3431	52.6966	52.6764	52.6744
66.4676	66.4919	66.4832	66.4676	66.3807	66.3431	65.6608	65.6476	65.6407

B Effective-Mass Calculations

Table B.1: Components of the inverse effective-mass tensor m_{ij}^{-1} (in units of m_0^{-1}) for the two uppermost valence bands and the lowest conduction band, obtained without spin-orbit coupling (without SOC), and for the corresponding band pairs in the calculation with SOC (with SOC-a and with SOC-b). Tensor symmetry was used, so only the independent components are listed: m_{xx}^{-1}, m_{yy}^{-1}, m_{zz}^{-1}, m_{xy}^{-1}, m_{xz}^{-1}, and m_{yz}^{-1}.

Band (n)	Component	without SOC	with SOC-a	with SOC-b
25 (v)	m_{xx}^{-1}	5.5	3.7	3.3
	m_{yy}^{-1}	5.5	3.7	3.3
	m_{zz}^{-1}	0.33	0.34	0.34
	m_{xy}^{-1}	$2 \cdot 10^{-4}$	$< 10^{-7}$	$6 \cdot 10^{-4}$
	m_{xz}^{-1}	0.06	0.22	0.16
	m_{yz}^{-1}	0.06	0.22	0.16
26 (v)	m_{xx}^{-1}	0.39	3.3	2.4
	m_{yy}^{-1}	0.39	3.3	2.4
	m_{zz}^{-1}	0.34	0.41	0.41
	m_{xy}^{-1}	$8 \cdot 10^{-6}$	$< 10^{-7}$	$< 10^{-7}$
	m_{xz}^{-1}	$6 \cdot 10^{-4}$	0.13	$7 \cdot 10^{-3}$
	m_{yz}^{-1}	$6 \cdot 10^{-4}$	0.13	$7 \cdot 10^{-3}$
27 (c)	m_{xx}^{-1}	6.3	6.4	6.4
	m_{yy}^{-1}	6.3	6.4	6.4
	m_{zz}^{-1}	6.3	6.4	6.4
	m_{xy}^{-1}	$< 10^{-7}$	$< 10^{-7}$	$< 10^{-7}$
	m_{xz}^{-1}	$3 \cdot 10^{-3}$	$3 \cdot 10^{-3}$	$3 \cdot 10^{-3}$
	m_{yz}^{-1}	$3 \cdot 10^{-3}$	$3 \cdot 10^{-3}$	$3 \cdot 10^{-3}$

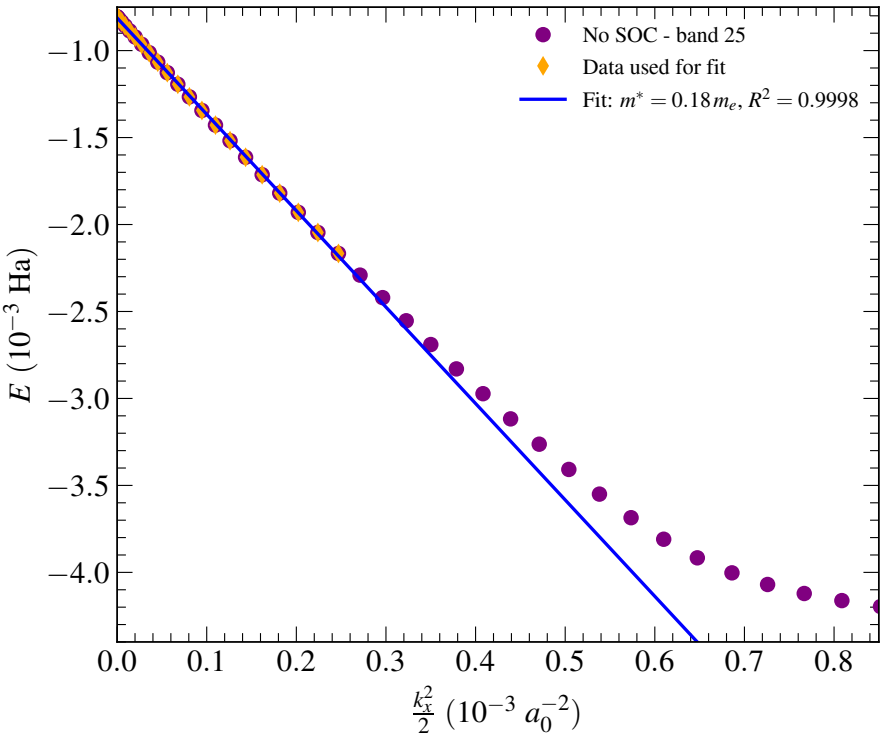

Figure B.1: *Kohn-Sham* eigenvalue E of band $n = 25$ without SOC as a function of $k_x^2/2$.

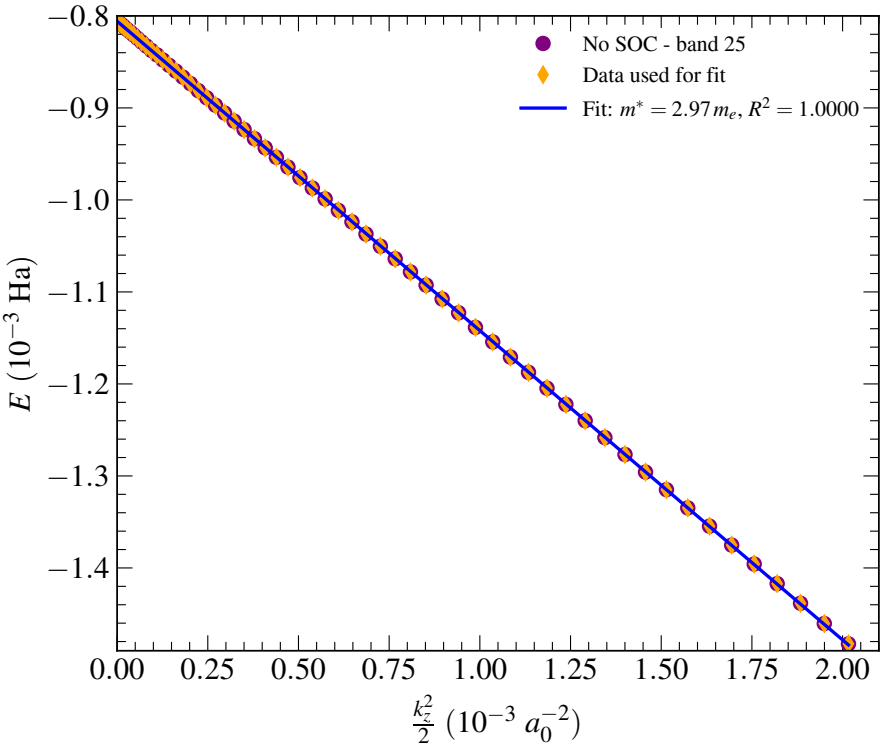

Figure B.2: *Kohn-Sham* eigenvalue E of band $n = 25$ without SOC as a function of $k_z^2/2$.

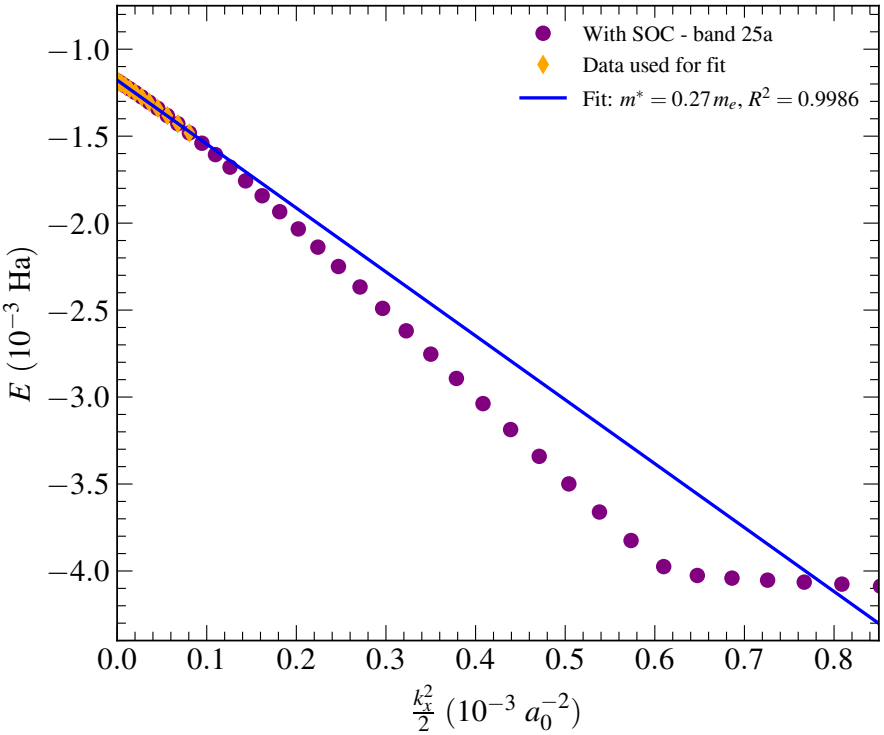

Figure B.3: *Kohn-Sham* eigenvalue E of band $n = 25a$ with SOC as a function of $k_x^2/2$.

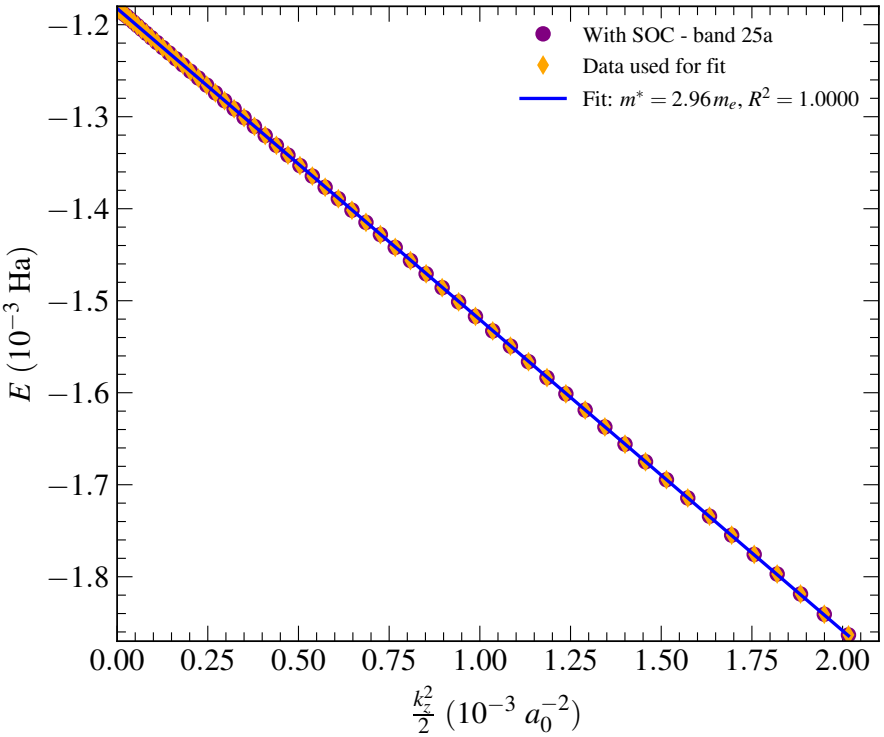

Figure B.4: *Kohn-Sham* eigenvalue E of band $n = 25a$ with SOC as a function of $k_z^2/2$.

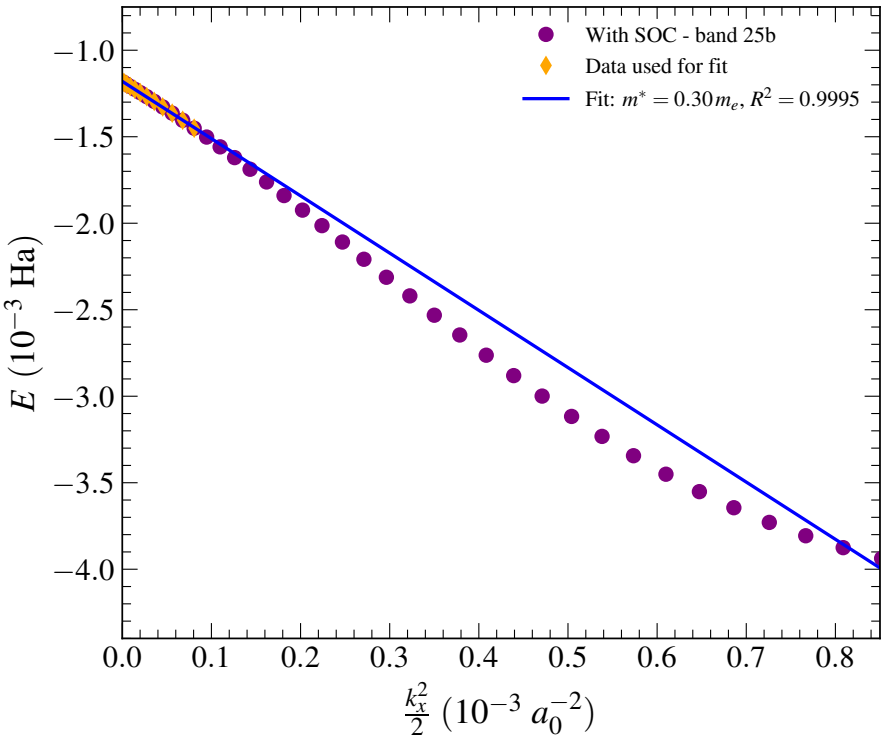

Figure B.5: *Kohn-Sham* eigenvalue E of band $n = 25b$ with SOC as a function of $k_x^2/2$.

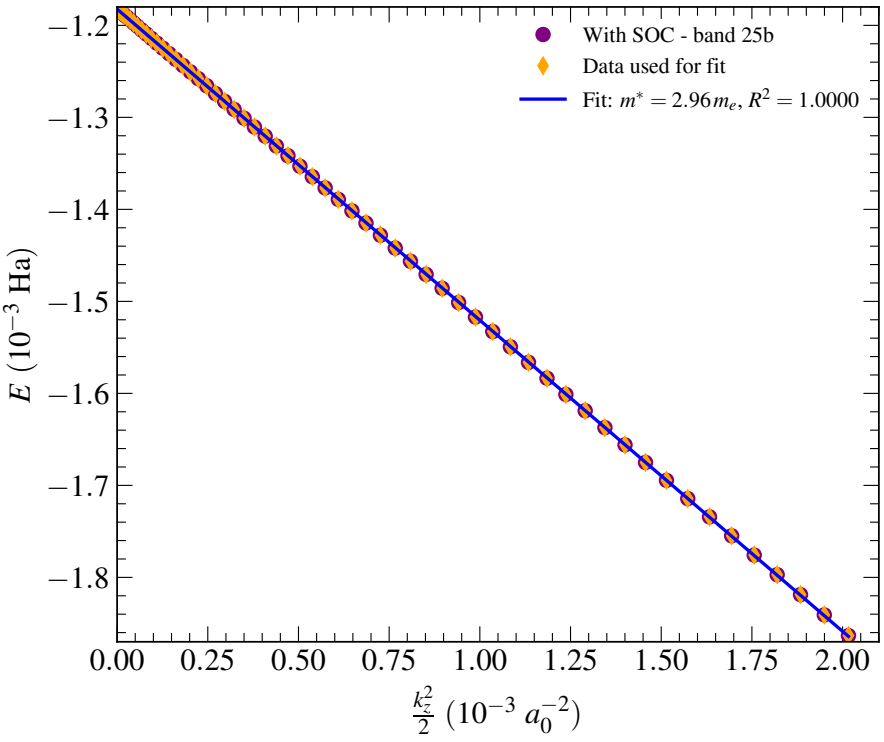

Figure B.6: *Kohn-Sham* eigenvalue E of band $n = 25b$ with SOC as a function of $k_z^2/2$.

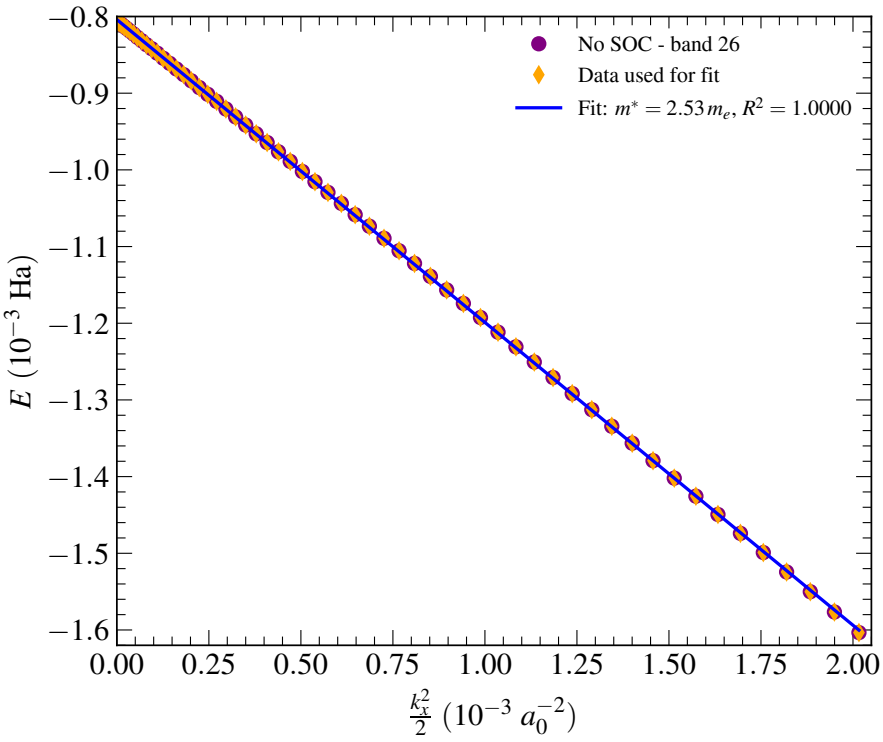

Figure B.7: *Kohn-Sham* eigenvalue E of band $n = 26$ without SOC as a function of $k_x^2/2$.

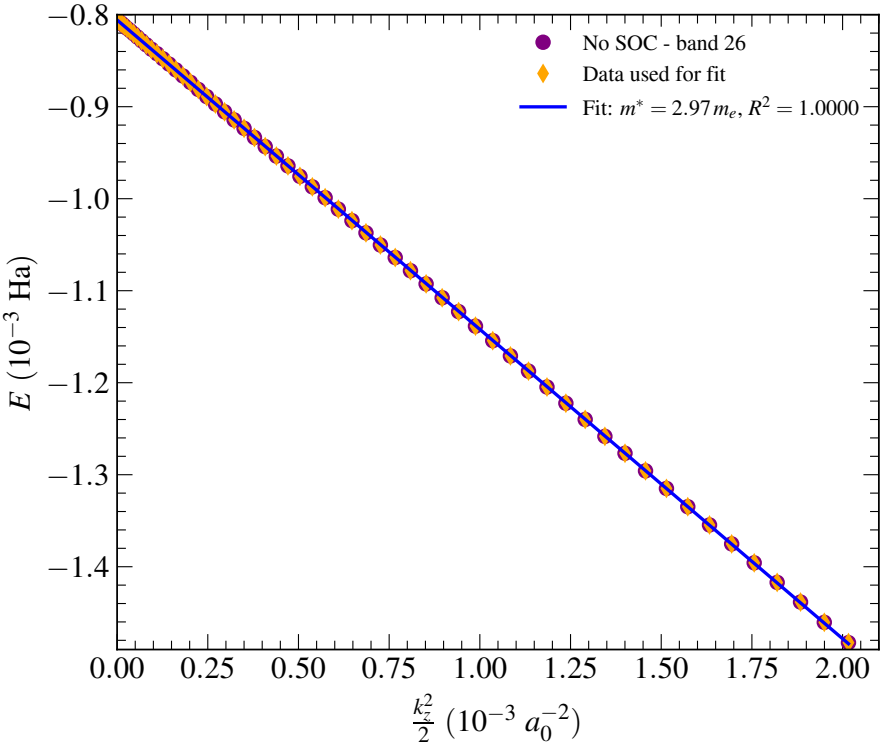

Figure B.8: *Kohn-Sham* eigenvalue E of band $n = 26$ without SOC as a function of $k_z^2/2$.

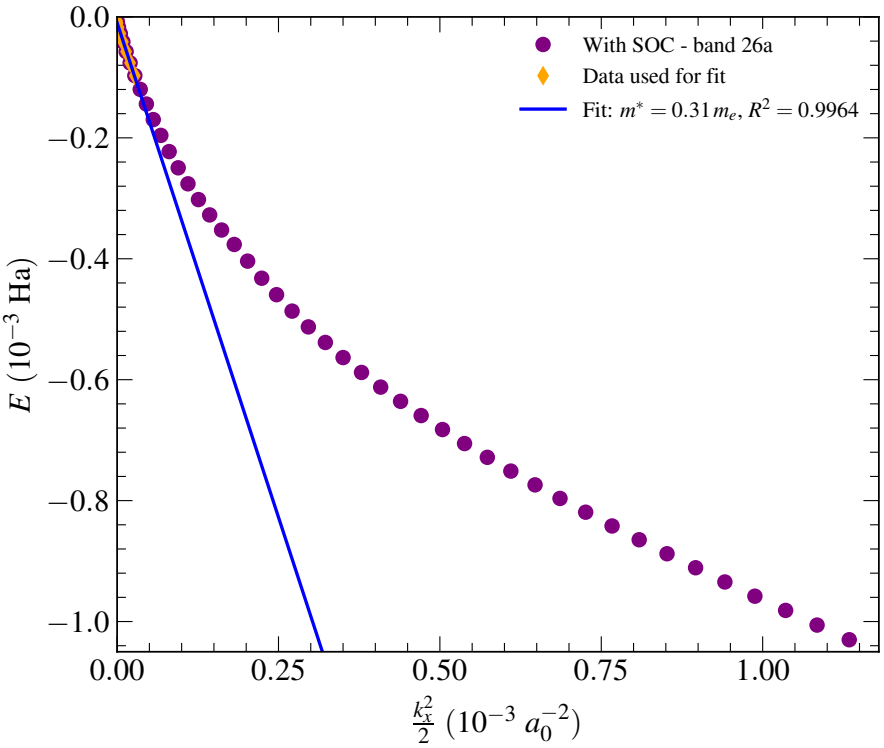

Figure B.9: *Kohn-Sham* eigenvalue E of band $n = 26a$ with SOC as a function of $k_x^2/2$.

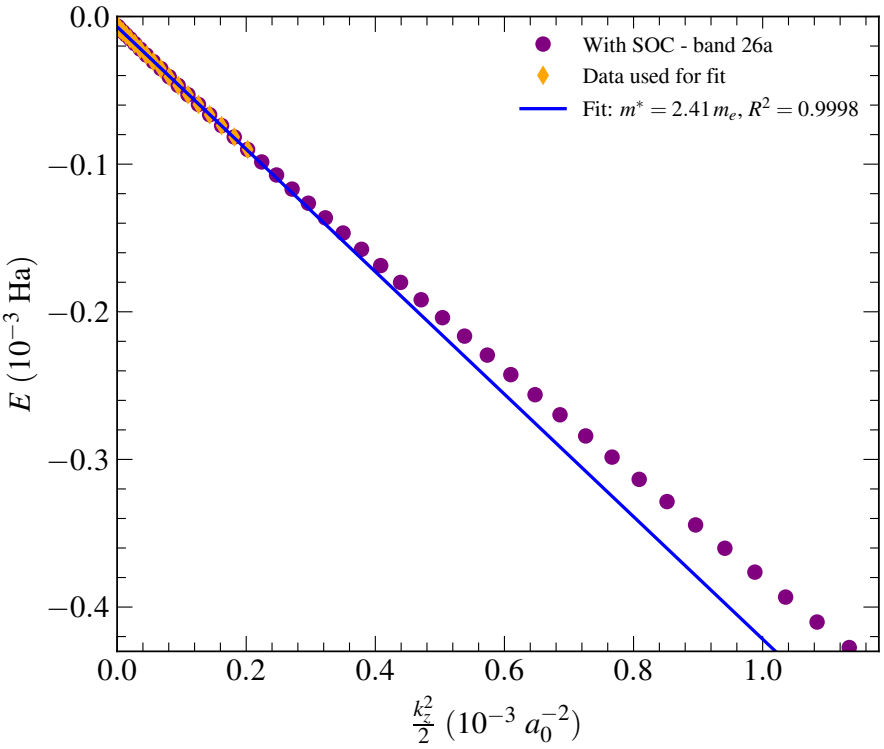

Figure B.10: *Kohn-Sham* eigenvalue E of band $n = 26a$ with SOC as a function of $k_z^2/2$.

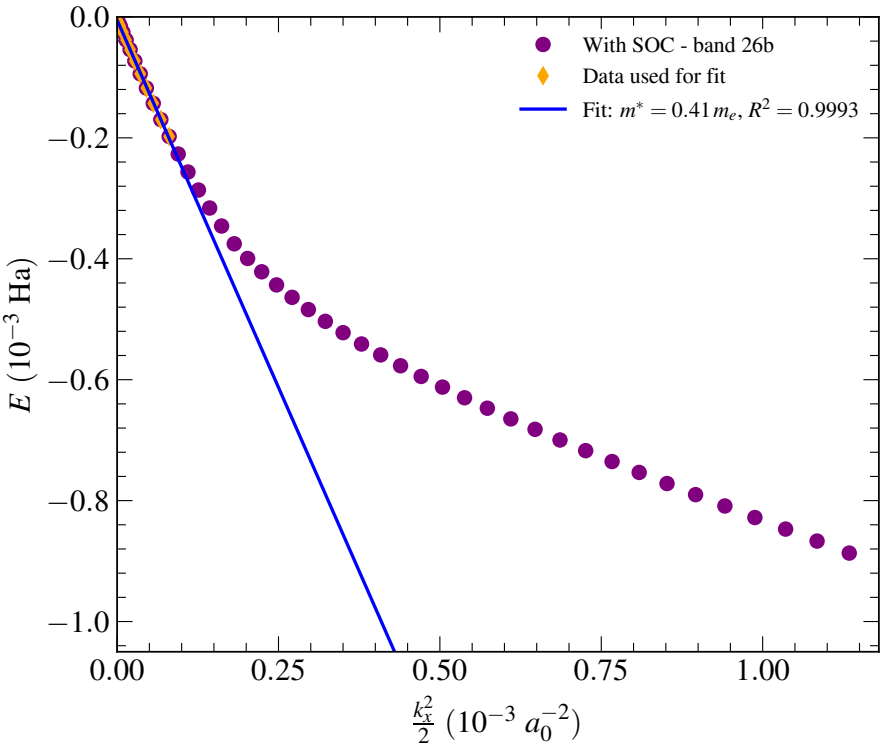

Figure B.11: *Kohn-Sham* eigenvalue E of band $n = 26b$ with SOC as a function of $k_x^2/2$.

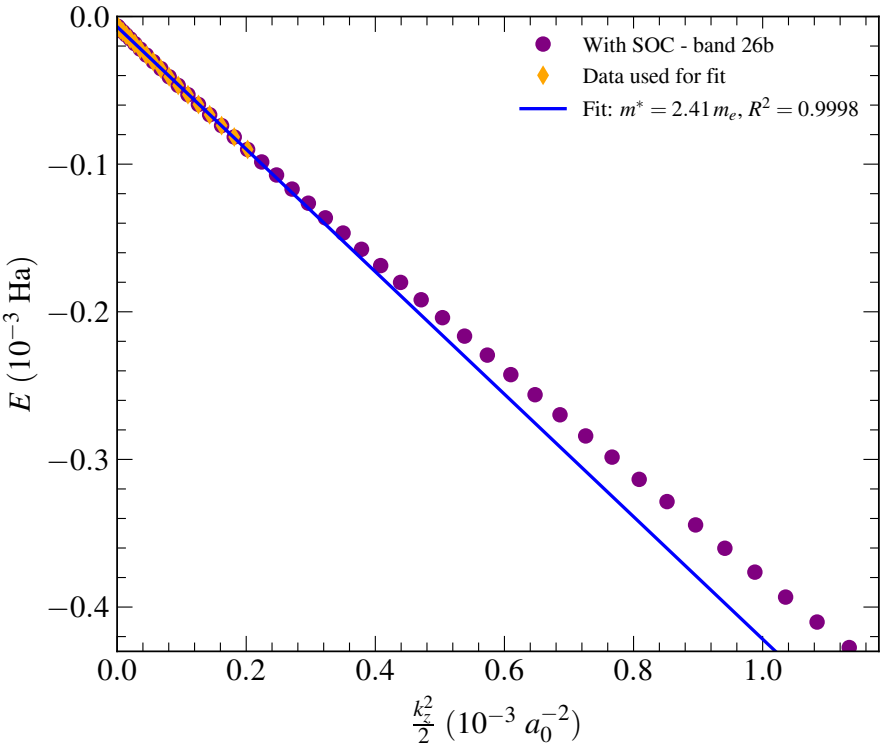

Figure B.12: *Kohn-Sham* eigenvalue E of band $n = 26b$ with SOC as a function of $k_z^2/2$.

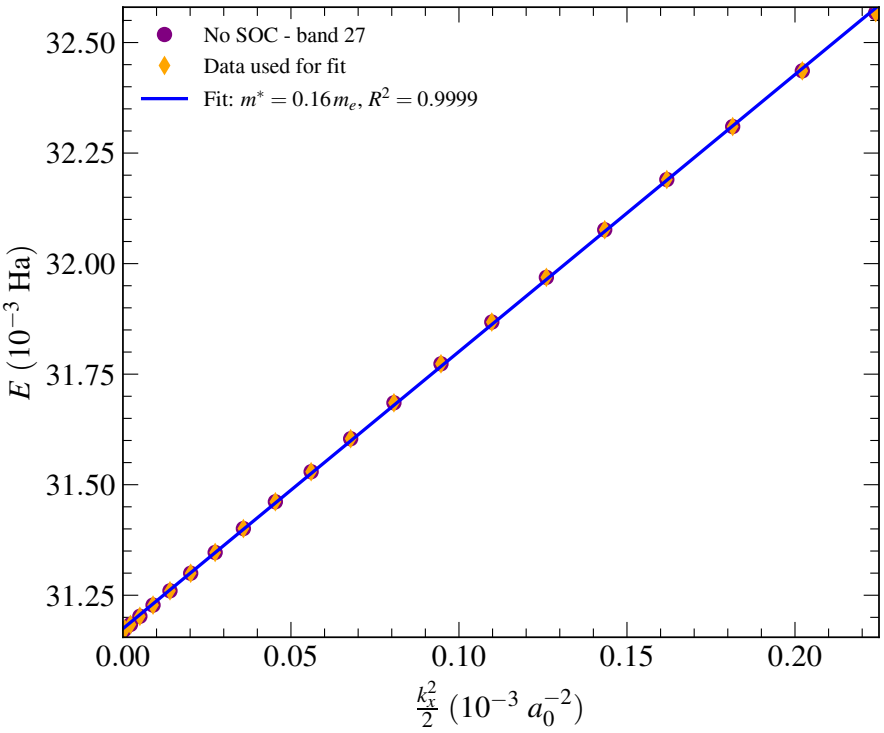

Figure B.13: *Kohn-Sham* eigenvalue E of band $n = 27$ without SOC as a function of $k_x^2/2$.

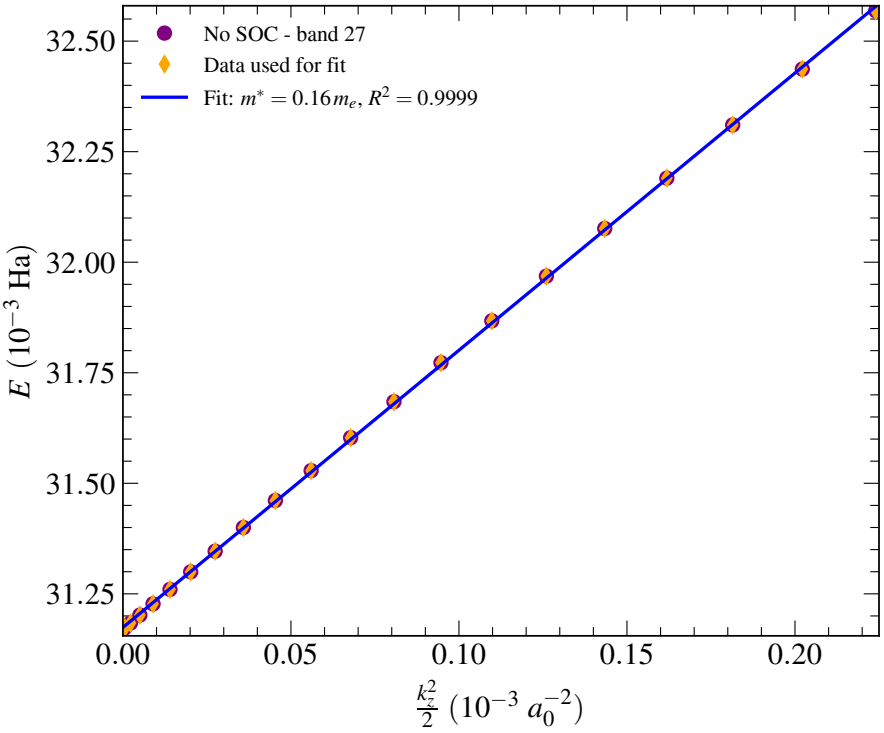

Figure B.14: *Kohn-Sham* eigenvalue E of band $n = 27$ without SOC as a function of $k_z^2/2$.

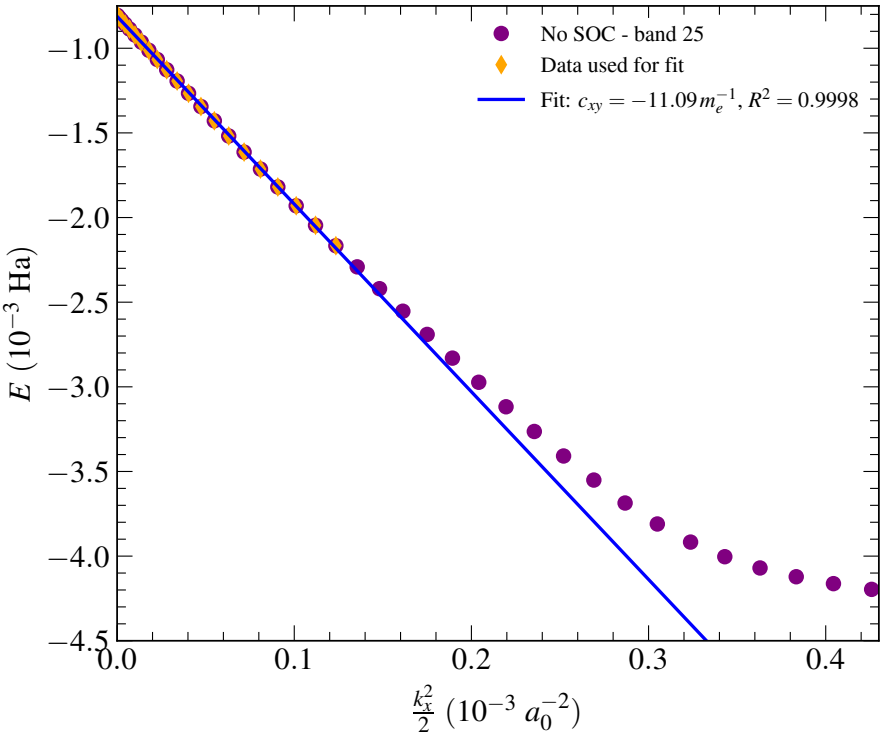

Figure B.15: *Kohn-Sham* eigenvalue E of band $n = 25$ without SOC as a function of $k_x^2/2$ along the xy direction.

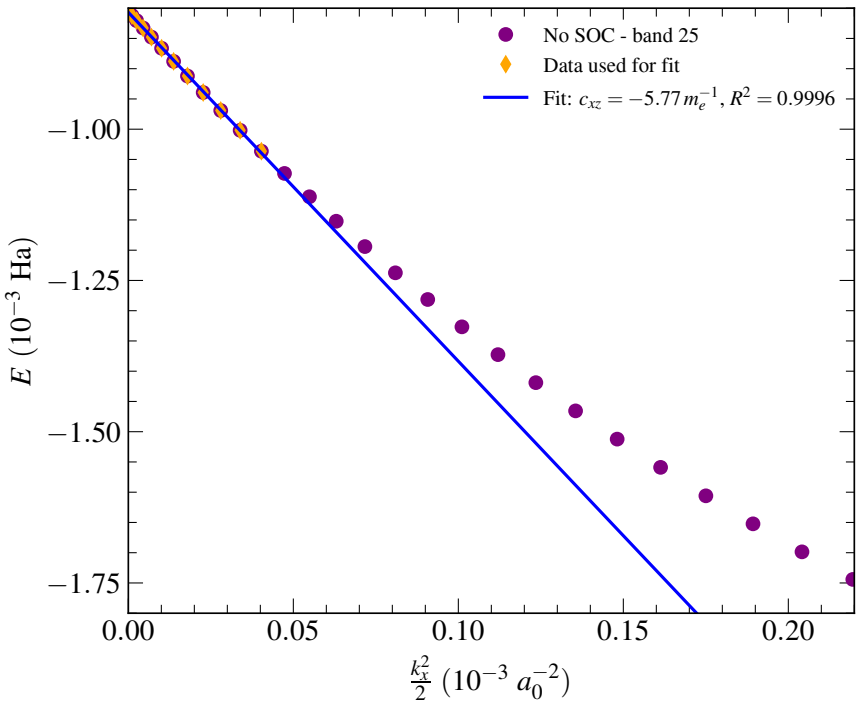

Figure B.16: *Kohn-Sham* eigenvalue E of band $n = 25$ without SOC as a function of $k_x^2/2$ along the xz direction.

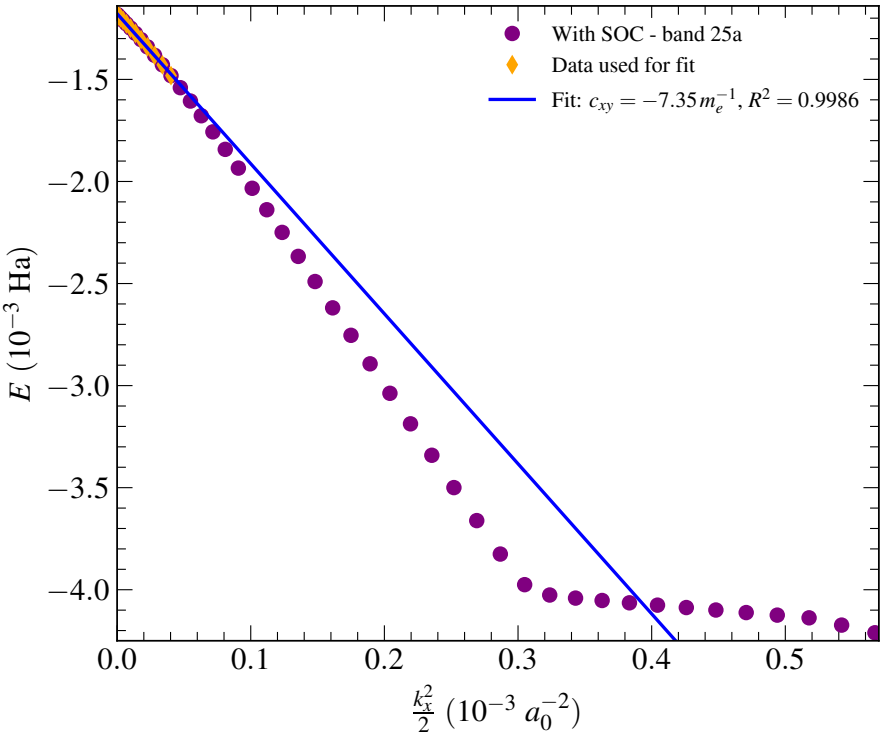

Figure B.17: *Kohn-Sham* eigenvalue E of band $n = 25a$ with SOC as a function of $k_x^2/2$ along the xy direction.

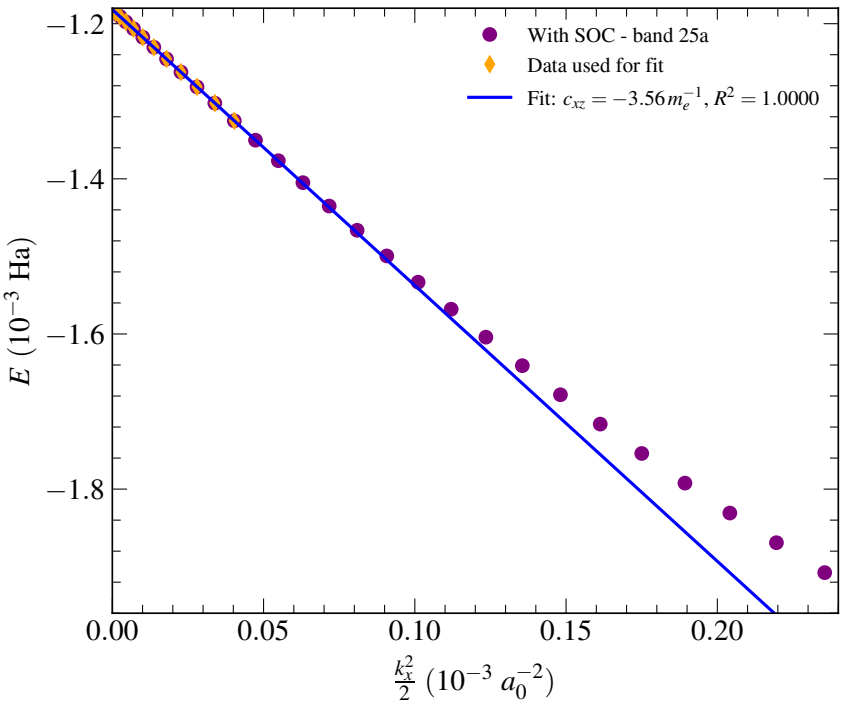

Figure B.18: *Kohn-Sham* eigenvalue E of band $n = 25a$ with SOC as a function of $k_x^2/2$ along the xz direction.

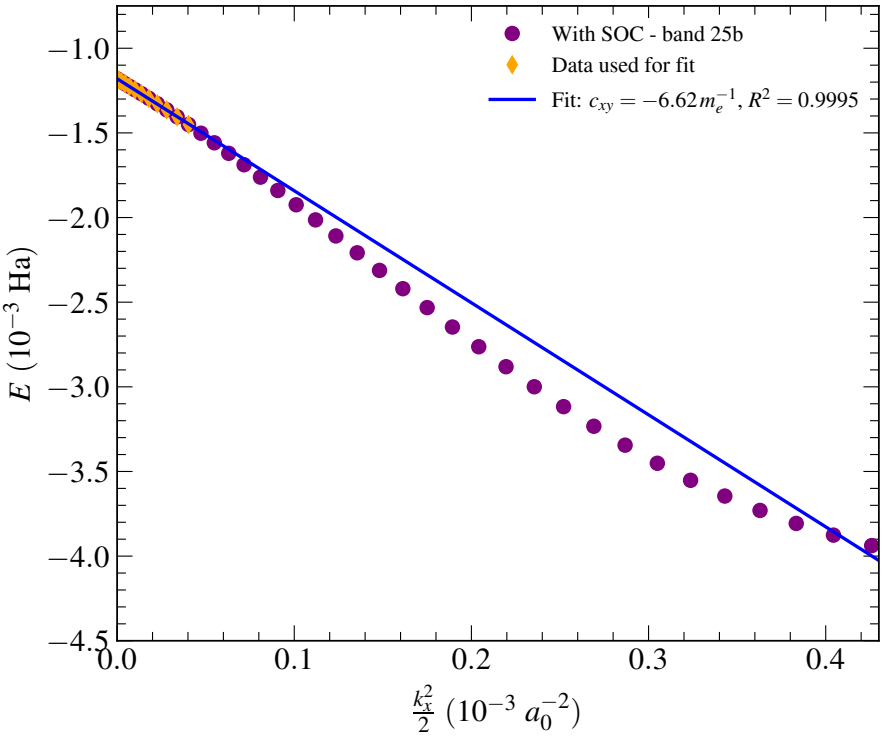

Figure B.19: *Kohn-Sham* eigenvalue E of band $n = 25b$ with SOC as a function of $k_x^2/2$ along the xy direction.

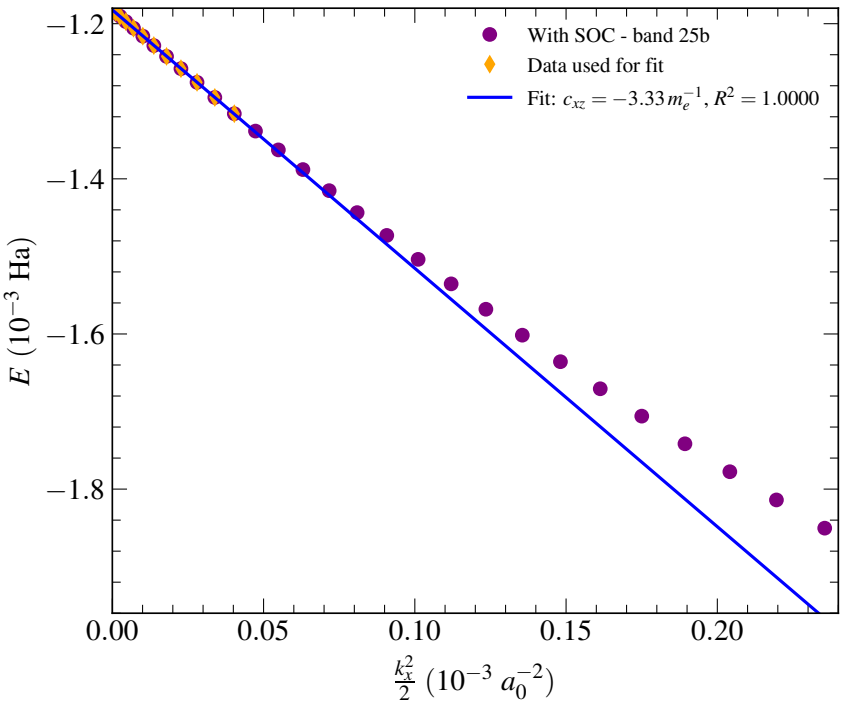

Figure B.20: *Kohn-Sham* eigenvalue E of band $n = 25b$ with SOC as a function of $k_x^2/2$ along the xz direction.

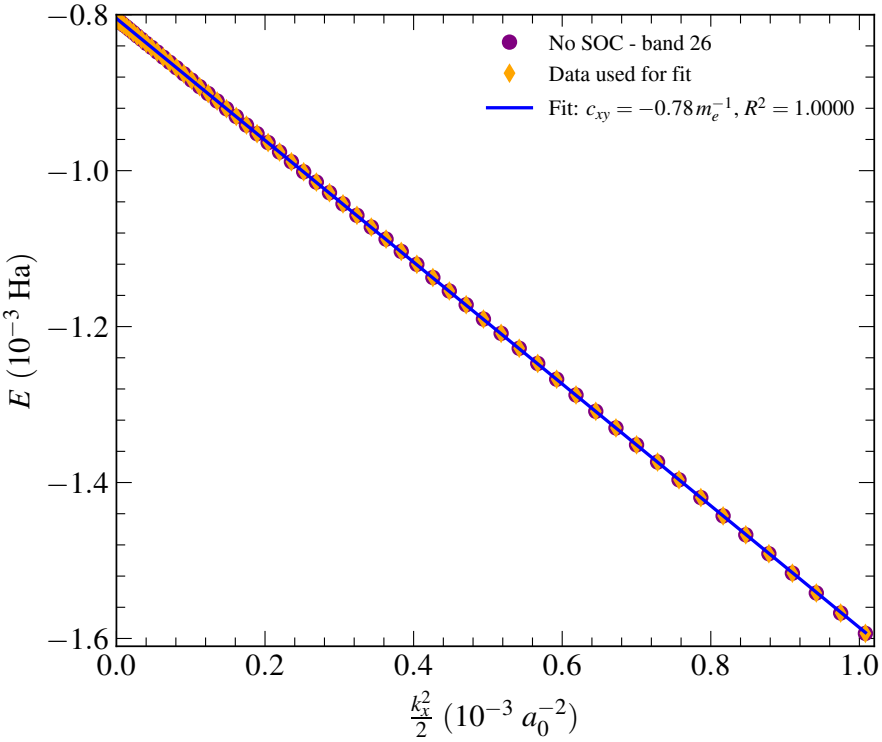

Figure B.21: *Kohn-Sham* eigenvalue E of band $n = 26$ without SOC as a function of $k_x^2/2$ along the xy direction.

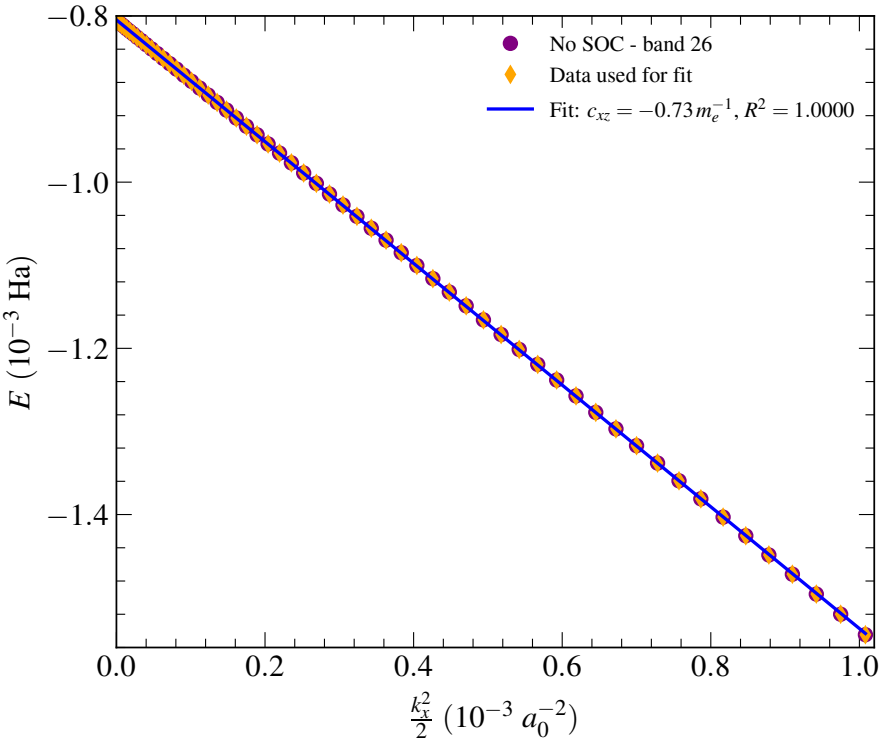

Figure B.22: *Kohn-Sham* eigenvalue E of band $n = 26$ without SOC as a function of $k_x^2/2$ along the xz direction.

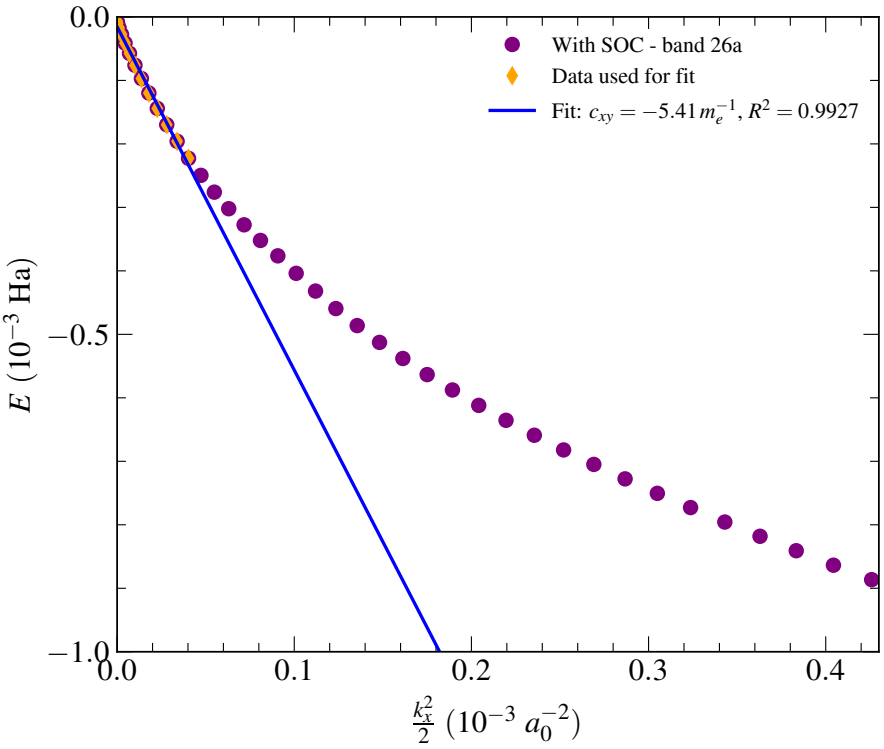

Figure B.23: *Kohn-Sham* eigenvalue E of band $n = 26a$ with SOC as a function of $k_x^2/2$ along the xy direction.

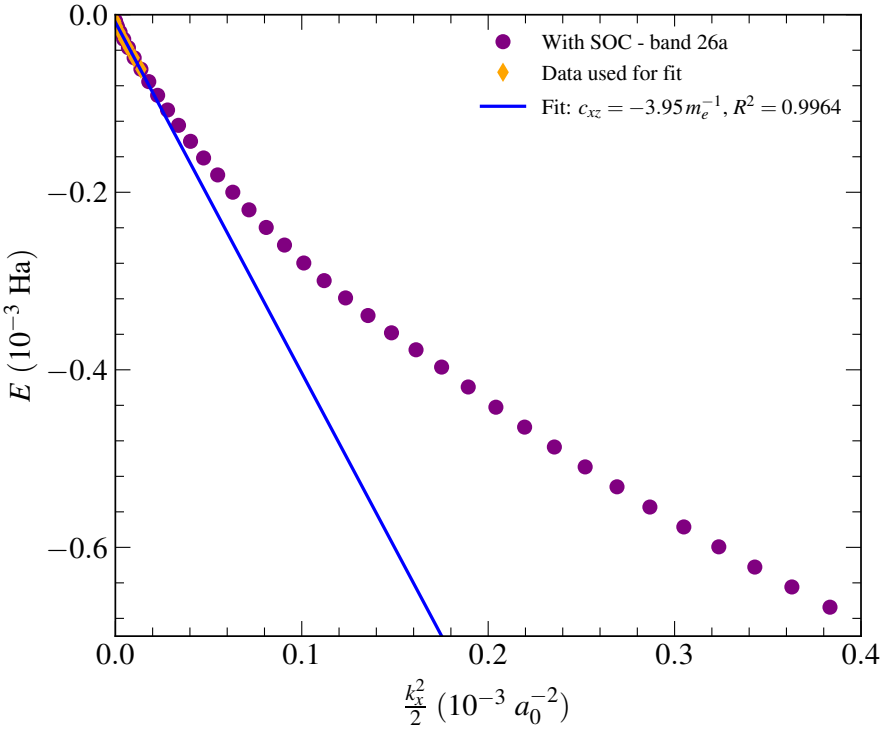

Figure B.24: *Kohn-Sham* eigenvalue E of band $n = 26a$ with SOC as a function of $k_x^2/2$ along the xz direction.

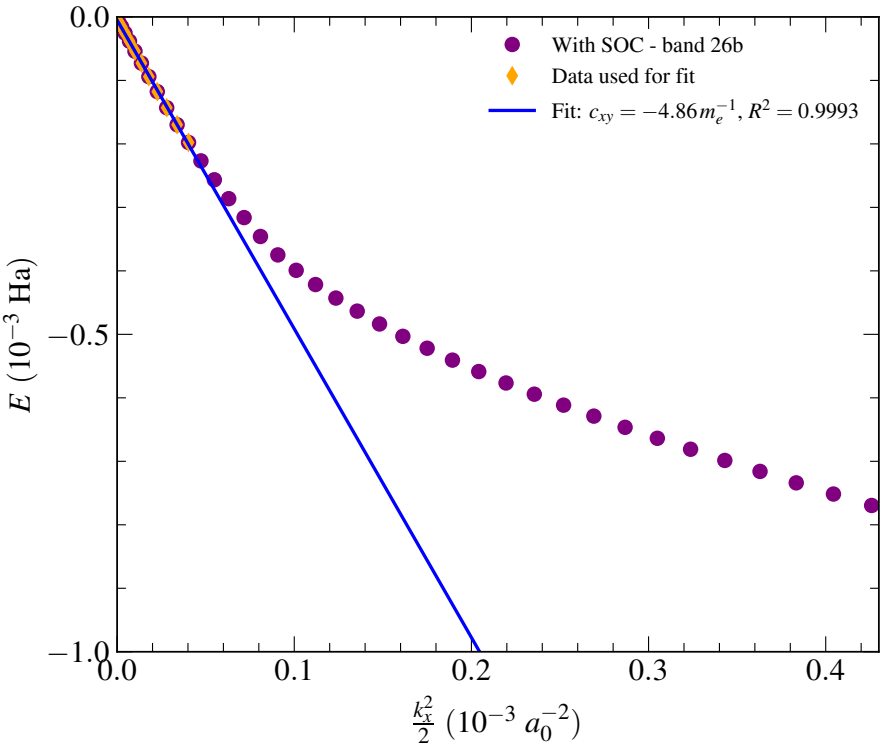

Figure B.25: *Kohn-Sham* eigenvalue E of band $n = 26b$ with SOC as a function of $k_x^2/2$ along the xy direction.

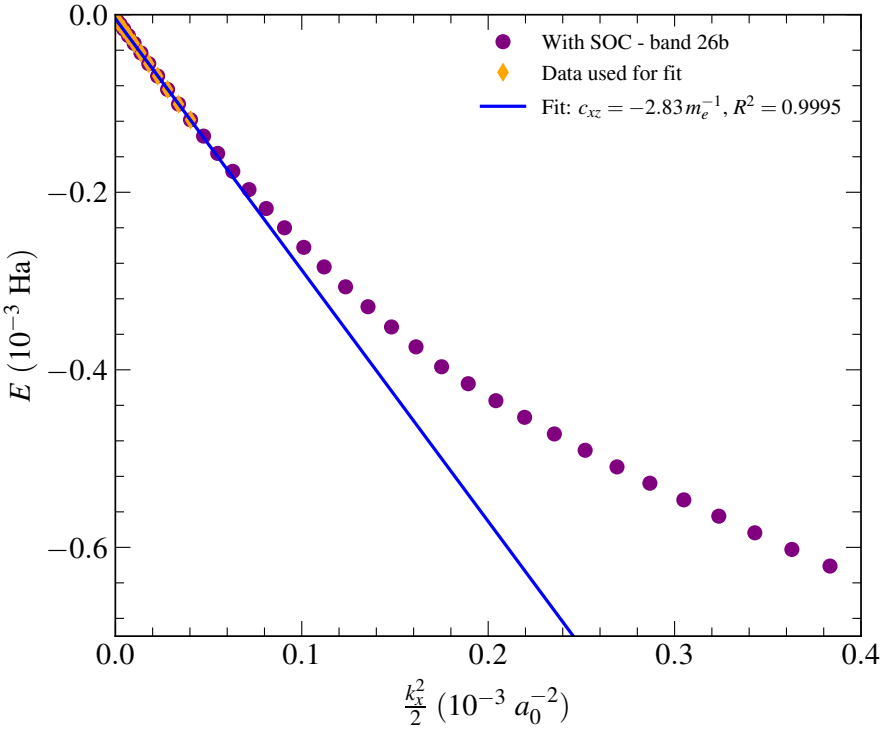

Figure B.26: *Kohn-Sham* eigenvalue E of band $n = 26b$ with SOC as a function of $k_x^2/2$ along the xz direction.

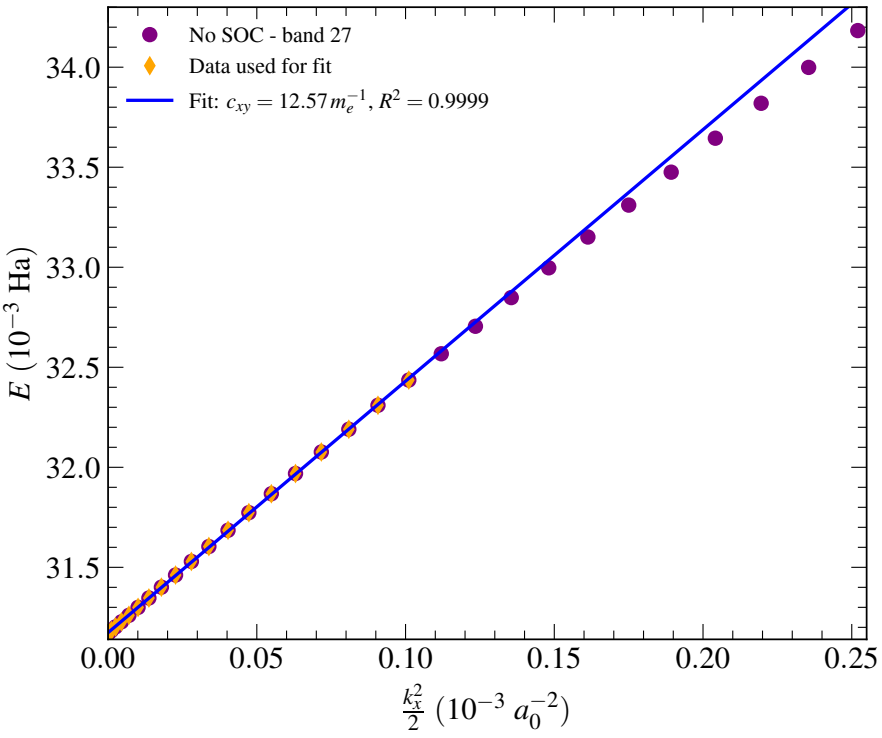

Figure B.27: *Kohn-Sham* eigenvalue E of band $n = 27$ without SOC as a function of $k_x^2/2$ along the xy direction.

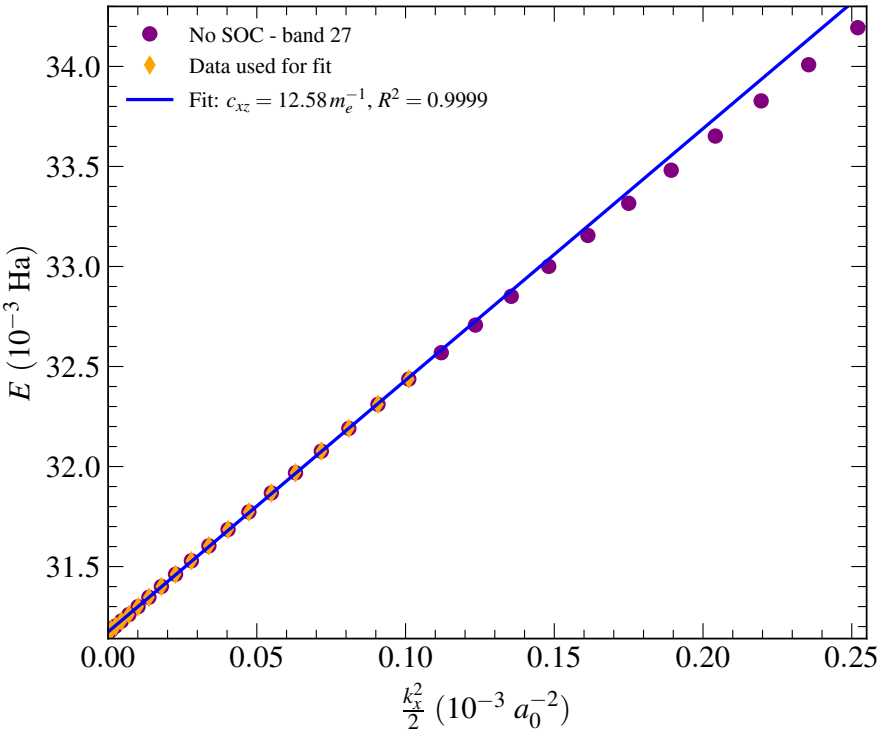

Figure B.28: *Kohn-Sham* eigenvalue E of band $n = 27$ without SOC as a function of $k_x^2/2$ along the xz direction.

C Mobility Calculations

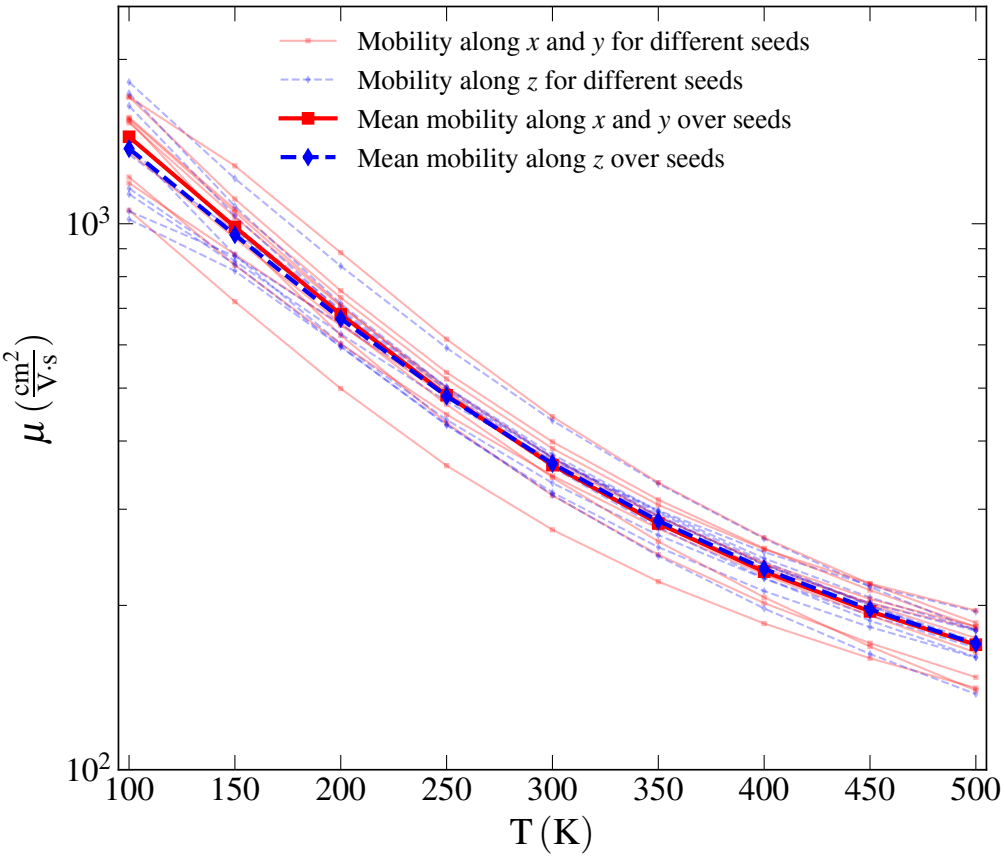

Figure C.1: Calculated temperature dependence of the electron mobility for the lowest conduction-band pair along the coordinate axes, for ten calculations (each with $N_k = 100$ and $N_\Omega = 100$) using different random-number seeds, together with their mean.

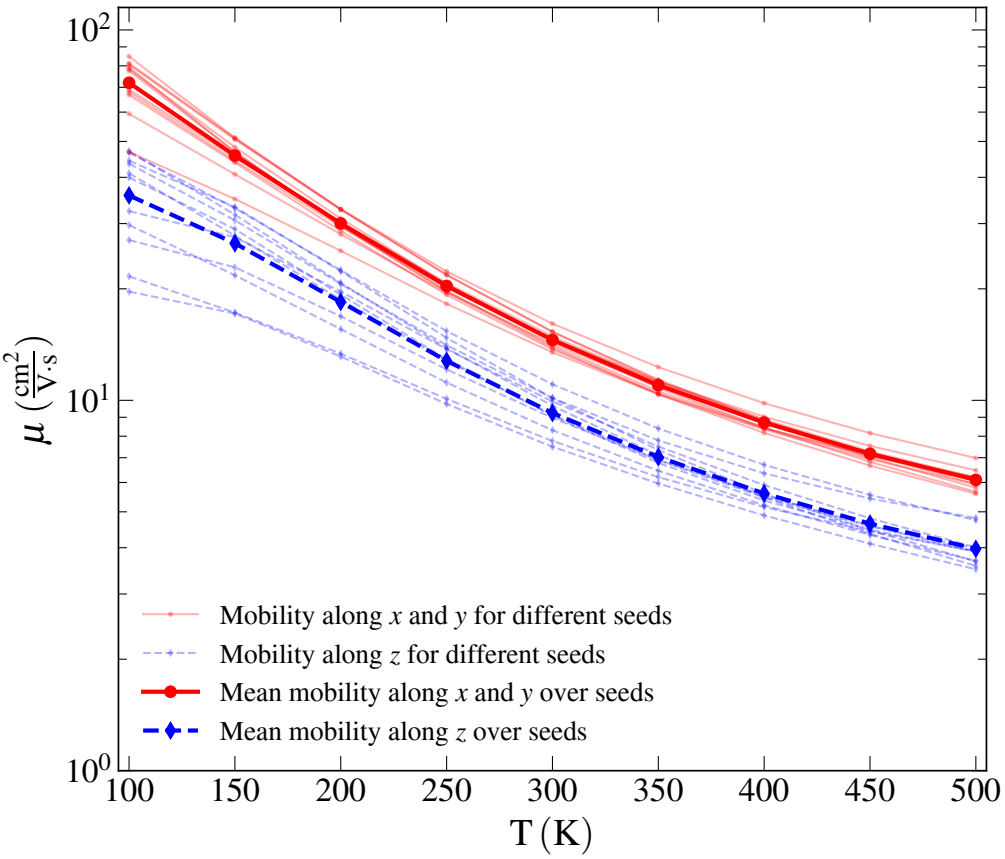

Figure C.2: Calculated temperature dependence of the hole mobility for the three uppermost valence-band pairs along the coordinate axes, for ten calculations (each with $N_k = 100$ and $N_\Omega = 100$) using different random-number seeds, together with their mean.

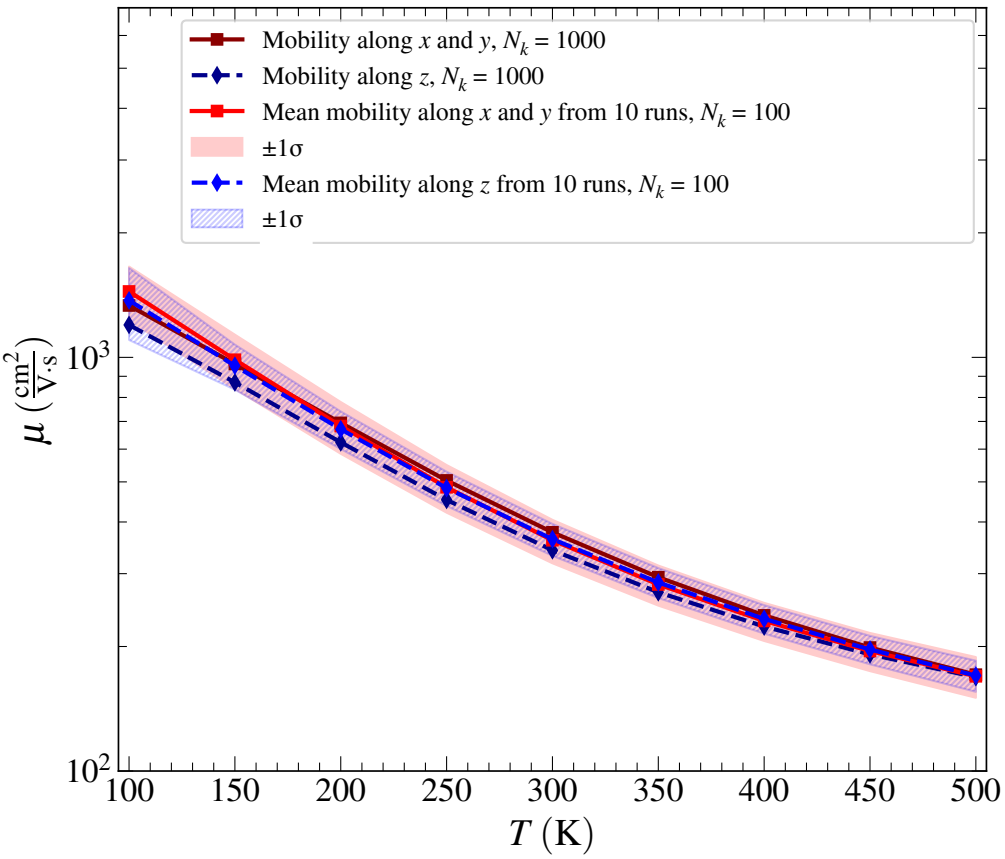

Figure C.3: Calculated temperature dependence of the electron mobility for the lowest conduction-band pair along the coordinate axes, averaged over ten calculations (each with $N_k = 100$ and $N_\Omega = 100$), together with the results of an independent calculation with $N_k = 1000$ and $N_\Omega = 100$.

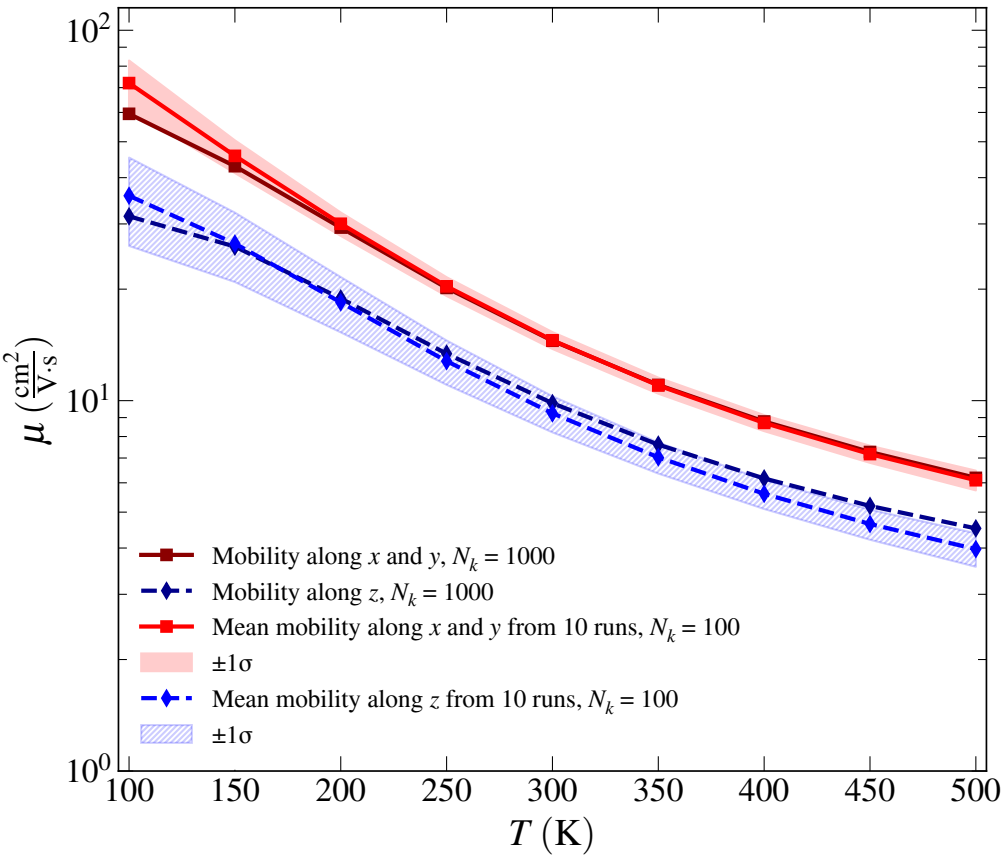

Figure C.4: Calculated temperature dependence of the hole mobility for the three uppermost valence-band pairs along the coordinate axes, averaged over ten calculations (each with $N_k = 100$ and $N_\Omega = 100$), together with the results of an independent calculation with $N_k = 1000$ and $N_\Omega = 100$.

D Additional Data

Table D.1: Diagonal elements of the high-frequency dielectric tensor $\hat{\varepsilon}_\infty$ and the Born effective-charge tensors $\hat{Z}^*$ for Zn and O, calculated using DFPT on the basis of DFT calculations with a $6 \times 6 \times 4$ *Monkhorst–Pack* k-point grid, both without and with SOC. The off-diagonal elements of these tensors are zero. Components in the plane normal to the **c** direction are denoted by $\perp$, and components parallel to it by $\parallel$.

Type	$\varepsilon_\infty^\perp$	$\varepsilon_\infty^\parallel$	$Z_\perp^*$(Zn)	$Z_\parallel^*$(Zn)	$Z_\perp^*$(O)	$Z_\parallel^*$(O)
Without SOC	6.6896	6.2432	2.1770	2.1985	-2.2142	-2.2189
With SOC	6.7108	6.2564	2.1778	2.1990	-2.2150	-2.2194

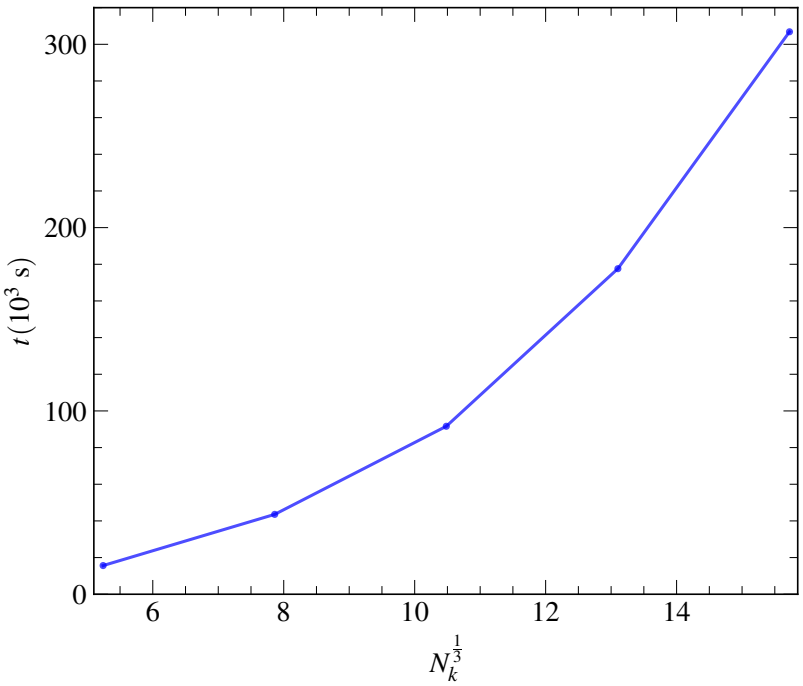

Figure D.1: Total execution time of the DFT and DFPT calculations of the high-frequency relative dielectric tensor (ε_∞) and Born effective charges (Z^*), as a function of the linear k-point density in the *Monkhorst–Pack* grid used for the DFT calculation at $E_{cut} = 45$ Ha. The grids were $6 \times 6 \times 4$, $9 \times 9 \times 6$, $12 \times 12 \times 8$, $15 \times 15 \times 10$, and $18 \times 18 \times 12$. Each calculation was run in parallel on 16 CPU cores of an Intel® Core™ i7-14700 processor.